Imperial College London

Transient optical studies of carrier dynamics in perovskite solar cells.

Jinhyun Kim

Department of Chemistry

Imperial College London

Submitted for the Degree of Doctor of Philosophy

November 2018

Except where otherwise cited or referenced is made, the work presented in this thesis is the result of my own work. This dissertation has not been submitted in whole or in part to satisfy another degree of qualification at this or any other university.

Jinhyun Kim,

November 2018

Abstract.

In this thesis, the charge carrier dynamics of trapping and transfer of electrons and holes are investigated for perovskite photovoltaics based on methylammonium lead iodide (MAPI$_3$) model materials. To understand the recombination processes in perovskite photovoltaics, the photophysical properties of perovskite thin-films and perovskite with charge transport layers (CTL) are studied with various optical measurement tools such as photoluminescence (PL) spectroscopy, time-correlated single photon counting (TCSPC) and transient absorption spectroscopy (TAS).

This thesis provides key new quantitative insights for the critical steps in the function of planar perovskite-based solar cells. One of the challenges of using spectroscopic tools to study perovskite is the reliability of the data. Strong intensity dependent behaviour is observed, which is important for interpretation data from different measurement techniques. Several studies have reported that trapping and recombination dynamics in MAPI$_3$ films are highly, and non-linearly light intensity (and carrier density) dependent. However, studies on the impact of this non-linear, light intensity behaviour on interfacial charge transfer efficiency and the efficiency of photocurrent generation in devices under operation, have been very limited to date.

Initially, perovskite structure and crystallization process, as well as the principles of photophysics and spectroscopy measurement techniques are introduced. A procedure for measuring charge carrier dynamics as a function of excitation power and the sample preparation is demonstrated.

The first chapter of the results section describes the dependency between excitation conditions and charge carrier dynamics of MAPI$_3$ with PEDOT:PSS and PC$_{61}$BM as a CTL, to unveil the

recombination behaviour in a perovskite device. The results show that different excitation density of the excitation source and repetition rate can cause significant difference on recombination processes. 1 Sun equivalent continuous-wave light emitting diode (LED) source allows collecting reliable PL quenching efficiency to estimate interlayers charge transfer rate. Steady-state and pulsed measurements indicate low transfer efficiencies at low excitation conditions (<5E + 15 cm−3) due to rapid charge trapping and low transfer efficiencies at high excitation conditions (>5E + 17 cm−3) due to fast bimolecular recombination. TCSPC and TAS were used to explore the dynamics.

The second chapter describes the change of the perovskite crystal with oxygen when kept in the dark and explores the impact on photoluminescence behaviour. Spectroscopic tools such as PL, absorptance and TAS are used to analyse the evolution of PL properties which is corelated with X-Ray diffraction (XRD) and device performance.

The third chapter focuses on the integrated perovskite device structure stacked with organic photovoltaics. In this structure, carrier transfer behaviour has been changed not only by the interface between CTL and perovskite-organics bulk heterojunction (BHJ) layer, but also by charge accumulation in whole device components such as electrode and Zinc-oxide (ZnO) hole blocking layer due to the electric field, which is the key to design new device structure.

The last chapter provides conclusions from these studies and suggests further work.

Table of contents

Contents

List of publications

- "Evidence for surface defect passivation as the origin of the remarkable photostability of unencapsulated perovskite solar solar cells employing aminovaleric acid as a processing additive", Chieh-Ting Lin, Francesca De Rossi, **Jinhyun Kim**, Jenny Baker, Jonathan Ngiam, Bob Xu, Sebastian Pont, Nicholas Aristidou, Saif A.Haque, Trystan Watson, Martyn A McLachlan, and James R Durrant, *Journal of Materials Chemistry A*, **2019**, 7, 3006-3001. DOI: 10.1039/C8TA11985F

- "Probing and controlling intragrain crystallinity for improved low temperature-processed perovskite solar cells", Tian Du, Claire H. Burgess, Chieh-Ting Lin, Flurin Eisner, **Jinhyun Kim**, Shengda Xu, Hongkyu Kang, James R. Durrant and Martyn A. McLachlan, *Advanced Functional Materials*, **2018**, 1803943. DOI: 10.1002/adfm.201803943

- "Excitation density dependent photoluminescence quenching and charge transfer efficiencies in hybrid perovskite/organic semiconductor bilayers.", **Jinhyun Kim**, Robert Godin, Stoichko D. Dimitrov, Daniel T. J. Bryant and James R. Durrant, *Advanced Energy Materials*, **2018**, 1802474. DOI: 10.1002/aenm.201802474

- "An effective approach of vapour assisted morphological tailoring for reducing metal defect sites in lead-free, $(CH_3NH_3)_3Bi_2I_9$ bismuth-based perovskite solar cells for improved performance and long-term stability", Sagar M. Jain, Dibya Phuyal, Matthew L. Davies, Meng Li, Bertrand Philippe, Catherine De Castro, Zhen Qiu, **Jinhyun Kim**, Trystan Watson, Wing Chung Tsoi, Olof Karis, Håkan Rensmo, Gerrit Boschloo, Tomas Edvinsson, James R. Durrant, *Nano Energy*, **2018**, 05, 003.

- "Elucidating the origins of sub-gap tail states and open-circuit voltage in methylammonium lead triiodide perovskite solar cells", Tian Du, **Jinhyun Kim**, Jonathan Ngiam, James R. Durrant, and Martyn A. McLachlan, *Advanced Functional Materials,* **2018**, 28,1801808.

- "Passivation of oxygen and light induced degradation by the PCBM electron transport layer in planar perovskite solar cells", Lin Chieh-Ting, Pont Sebastian, **Kim Jinhyun**, Du Tian, Xu Shengda, Li Xiaoe, Bryant Daniel, McLachlan Martyn, and Durrant James, *Sustainable Energy & Fuels*, **2018**, 2, 1686-1692.

- "Molecular engineering using an anthanthrone dye for low-cost hole transport materials: A strategy for dopant-free, high-efficiency, and stable perovskite solar cells", Hong Duc Pham, Thu Trang Do, **Jinhyun Kim**, Cecile Charbonneau, Sergei Manzhos, Krishna Feron, Wing Chung Tsoi, James R. Durrant, Sagar M. Jain, and Prashant Sonar, *Advanced Energy Materials*, **2018**, 8, 1703007.

- "One step facile synthesis of a novel anthanthrone dye-based, dopant-free hole transporting material for efficient and stable perovskite solar cells", Hong Duc Pham, Kazuma Hayasake, **Jinhyun Kim**, Thu Trang Do, Hiroyuki Matsui, Sergei Manzhos, Krishna Feron, Shizuo Tokito, Trystan Watson, Wing Chung Tsoi, Nunzio Motta, James R. Durrant, Sagar Motilal Jain and Prashant Sonar, *J. Mater. Chem. C*, **2017**, 6, 3699.

Abbreviations

ΔOD	Optical density difference
t	Tolerance factor
A_{asb}	Absorbance
A_{ast}	Absorptance
AFM	Atomic force microscopy
Al	Aluminium
BHJ	Bulk-heterojunction
CB	Conduction band
CCD	Charge coupled device
CGD	Centre for Global Development
CLT	Charge transport layers
DI water	Deionization water
DMSO	Dimethyl sulfoxide
DSSC	Dye-sensitised solar cells
E_A	Activation energies
Eg	Band gap
EQE	External quantum efficiency
ESA	Excited state absorption signals
ETM	Electron-transporting material
E_{trap}	Deep-level trap
FF	Fill factor
fs	Femtosecond
fs-TAS	Femtosecond transient absorption spectroscopy
FWHM	Full width at half maximum

GA	Gas-assisted
GB	Glove box
GSB	Ground state bleaching signals
HOMO	Highest occupied molecular orbital
HTM	Hole-transporting material
IEA	International Energy Agency
I_{emi}	Photoluminescence emission intensity
I_{ex}	Excitation intensity
I_{exc}	Photoluminescence excitation intensity
Int	l light intensity
IRF	Instrument response function
ISCAS	Chinese Academy of Sciences
J_{max}	Current density maximum
J_{SC}	Short circuit current density
J–V	Current density-voltage
LiF	Lithium floride
LOMO	Lowest unoccupied molecular orbital
LPF	Long pass filter
MA^+	Methylammonium ions
MAI	Methyl-ammonium iodide
$MAPI_3$	Methylammonium lead iodide ($CH_3NH_3PbI_3$)
Mtoe	Million tonnes of oil equivalent
N2200	Poly{[N,N'-bis(2-octyldodecyl)naphthalene-1,4,5,8-bis(dicarboximide)-2,6-diyl]alt-5,5'-(2,2'-bithiophene)}
Nd:YAG	Neodymium-doped yttrium aluminium garnet

n-i-p	Normal structure device
nm	Nanometre
NREL	National Renewable Energy Laboratory
ns	Nanosecond
N_t	Trap density
OECD	Economic Co-operation and Development countries
OPA	Optical parametric amplification
OPV	Organic photovoltaic
PB	Photo bleaching signals
$PC_{61}BM$	[6,6]-phenyl-C61-butyricacidmethyleater
PCE	Power conversion efficiency
PEDOT:PSS	Poly(3,4-ethylenedioxythiophene) polystyrene sulfonate
PFN	Poly [(9,9-bis(3'-(N,N-dimethylamino)propyl)-2,7-fluorene)-alt-2,7-(9,9–dioctylfluorene)]
P_I	Incident light intensity
PIA	Photoinduced transient absorption
p-i-n	Inverted structure device
PL	Photoluminescence
PL_0	PL intensity
PLQ	PL quenching
PLQE	Photoluminescence quenching efficiency
ps	Picosecond
PSC	Perovskite solar cell
PTAA	Poly(triaryl amine)
PV	Photovoltaics

R_{diff}	Diffuse reflectance
Ref_{sub}	Absorptance of the substrate
R_{spec}	Specular reflectance
SC	Short circuit
SC	Spin coated
SE	Stimulated emission signals
SPF	Short pass filters
Spiro-MeOTAD	2,20,7,70-tetrakis-(N,N-di-p-methoxyphenylamine)9,90-spirobifluorene
SRH	Shockley-Read-Hall
ssDSSCs	Solid-state dye-sensitised solar cells
ss-PL	Steady-state photoluminescence
T	Transmittance
TA	Transient absorption
TAS	Transient absorption spectroscopy
TCSPC	Time-correlated single photon counting
tr-PL	PL transient spectroscopy (Transient photoluminescence)
TT	DT-PDPP2T-TT
VB	Valence band
V_I^+	Iodine vacancies
V_{max}	Voltage maximum
V_{OC}	Open circuit voltage
XRD	X-Ray diffraction
ZnO	Zinc-oxide

Acknowledgement

First of all, I would like to sincerely thank my supervisor, James Durrant, for his support and help during my PhD course. It is my honour to join his wonderful group and work with a group of professional and dedicated people. All the experience and knowledge gained here will benefit me for the rest of my life. make my PhD course was really essential, without you I couldn't make it achievable.

I gratefully acknowledge Stoichko and Robert for their help on my research. Their knowledge and patience in answering my questions have benefited me a lot. I am thankful to Li and Pabitra for their perpetual support. I also thank Tian, Saga, Lin. It has been a great time working with them. The good discussions and chats between us have been quite helpful for my research.

Apart from experiments, I learned the fun of gardening from Li. Thanks to her meticulous care, the plants are still thriving even in our basement office without sunlight. This reminds me of those of us who are working in the basement: because a group of fantastic people are accompanied by each other, the experimental work can be a great fun. With you guys, I could be a baking Padawan of the Cake Club and enjoy the crossword time even though I could barely solve it. I really enjoyed the time with you guys Scot, Chaz, Jia Ying, Seb, Maddy, Dan, Hyo Jung, Laia, Michael, Camilo, James, Tom, Ludmilla, Sacha, Shababa, Yu Han, Yi Fan, Weidong, Carlota, Jamie, Ding Dong, Elisa, Ernest, Steph, Andreas, Flo, Yimeng, Xiuli, Jia Qi, Derya, Davide, Jason, and Andy...

I greatly thanks to my family for all the support and encouragement. Very special thanks to my great love, Jiaxi!

Chapter 1. Introduction

Contents

1.1. Motivation and context

'The sun, the moon and the stars would have disappeared long ago...

had they happened to be within the reach of predatory human hands'.

-Havelock Ellis-

Advances in human civilisation have been fuelled by increased energy consumption, with expanding energy demands encouraging further developments in technology. According to the International Energy Agency (IEA), the world's total primary energy supply was 13761 Mtoe (million tonnes of oil equivalent) in 2016, almost double that of the 6101 Mtoe estimated in 1973 (in Figure 1.1).[1] Interestingly, electricity accounted for 9.4% of the total consumption rate in 1973; in 2016, this increased to 18.8%. This trend was also observed in the Organisation for Economic Co-operation and Development countries (OECD), where the electricity usage rate was even higher at 22.3% in 2016.[1] A report from the Centre for Global Development (CGD) showed that higher electricity consumption was correlated with the human development index score, which indicates the level of development and human welfare. This means the increasing trend of energy consumption will only grow more sharply as less-developed countries become better developed.[2] Despite increasing electricity usage in the modern world, most of the electricity (around 65.3% in 2016) is still generated by burning fossil fuels (coal, natural gas and oil), and this burning of fossil fuels is largely believed to be the source of ecological issues, such as the greenhouse effect and global climate change. Thus, generating electricity from eco-friendly sources becomes very attractive. Solar energy is one such alternative source that can be harnessed using solar cells and solar thermal technologies.[3]

World total final consumption by fuel

1973 4661 Mtoe

- Oil — Oil 48.3%
- Natural gas — Natural gas 14.0%
- Biofuels and waste — Biofuels and waste 13.1%
- Coal — Coal 13.5%
- Other
- Electricity — Electricity 9.4%

2016 9555 Mtoe

- Biofuels and waste 11.0%
- Natural gas 15.3%
- Coal 10.8%
- Other 3.4%
- Oil 40.9%
- Electricity 18.8%

Other*includes heat, solar thermal, and geothermal
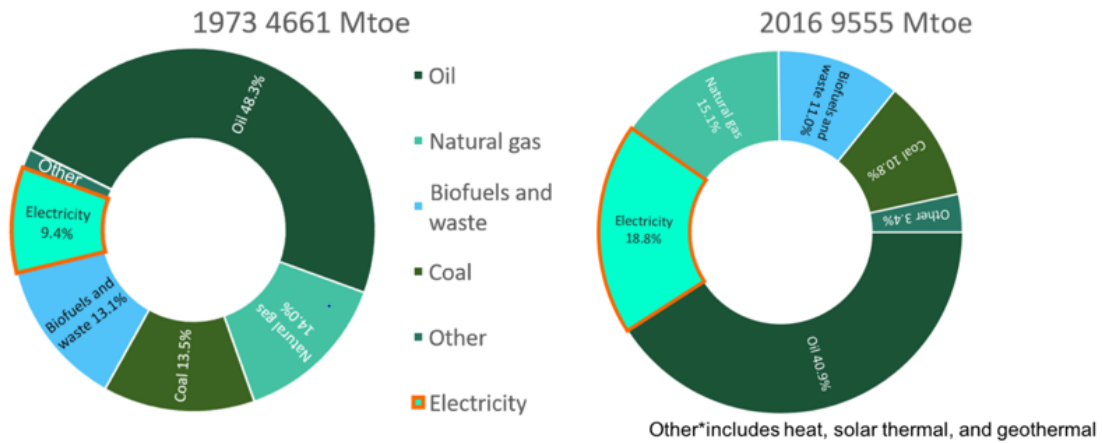
World Electricity generation by source

1973 6131 TWh
(Solar PV 4 TWh ~0.07%)

	Oil 24.8%	Natural gas 12.1%
		Nuclear 3.3%
Coal 38.3%	Hydro 20.9%	

2016 24973 TWh
(Solar PV 328 TWh ~1.3%)

		Nuclear 10.4%
Natural gas 23.2%		Non-hydro renewables and waste 8.0%
Hydro16.3%	Coal 38.4%	Oil 3.7%

Non-hydro renewables and waste* includes geothermal, solar, wind tide/wave/ocean, biofuel, waste, heat and other
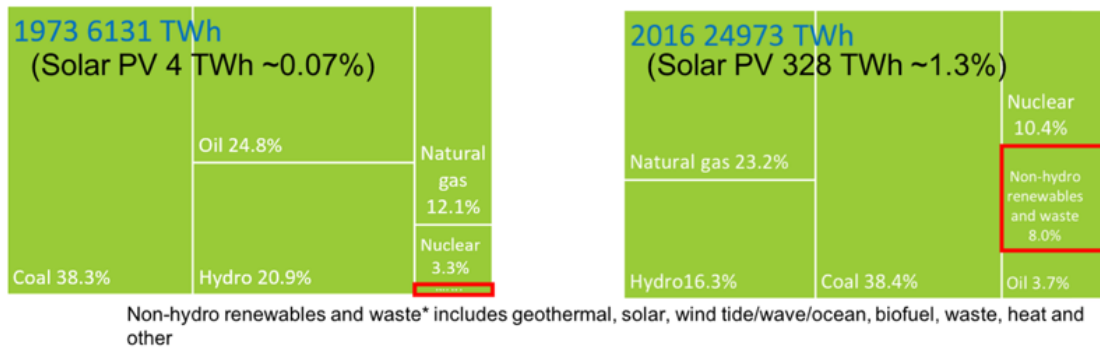
Figure 1.1 IEA charts of global net energy consumption by fuel type and global electricity production by fuel or energy source. [1]

According to the National Renewable Energy Laboratory (NREL), the earth annually receives an average direct normal irradiance of approximately 5 kWh/m^2 of energy daily from the sun.[4] This abundant amount of solar energy is a renewable and scalable energy source that can be harnessed using various technologies, such as photovoltaic and solar thermal collectors. However, electricity generation from photovoltaics (PV) in 2016 was approximately 1.3% (328 TWh) of the total electricity generation.[1]

Currently, the solar cell industry is dominated by crystalline silicon solar cells (80% market share).[5] Crystalline silicon solar cells have been developed to achieve cost-efficient energy conversion; unfortunately, the fragility of silicon imposes limits on silicon solar cell

applications.[6] Low-temperature and solution-processable solar cells, such as organic solar cells, have been extensively studied to complement crystalline silicon solar cell technology.[7] Because they have recently surpassed 20% solar energy conversion efficiencies using low-cost solution-based processing methods, photovoltaic cells based on hybrid perovskite materials have also quickly gained attention as they are exceptionally encouraging for commercial applications.[8] In 2009, Kojima et al.[9] reported an organometallic lead halide perovskite (methylammonium lead(II) halides, $CH_3NH_3PbX_3$ (X=halogen)) layer could substitute the dyes traditionally used to sensitise a mesoporous titanium dioxide layer in dye-sensitised solar cells (DSSC).[10] Following this discovery, the perovskite-based solar cell technology developed quickly with dramatic enhancements reported for solar efficiency. In Kojima's work, the perovskite-based DSSC had a power conversion efficiency of 3.8% and unstable properties since the perovskite was dissolved by the corrosive liquid redox electrolyte. However, solid-state dye-sensitised solar cells (ssDSSCs) based on 2,20,7,70-tetrakis-(N,N-di-p-methoxyphenylamine)9,90-spirobifluorene (Spiro-MeOTAD) were produced as a solution to the efficiency and stability limitations of liquid electrolyte DSSCs.[11] Spiro-MeOTAD, a solid-state hole-transporting material (HTM), has molecular orbital energy levels and pore-filling qualities that are required for efficient ssDSSCs. In 2012, the photo conversion efficiency of such ssDSSCs was improved to about 10% by Kim et al.,[12] leading to great interest from both industry and academics alike. The introduction of $CH_3NH_3PbI_3$, methylammonium lead iodide (MAPI$_3$) as a light absorber in such solar cells resulted in rapidly increasing energy conversion efficiencies.[13] Further experiments with Al_2O_3, instead of mesoporous TiO_2, scaffolds resulted in an increase in open circuit voltage and showed that electron extraction did not require a scaffold; thus, the perovskite itself can also act as the free charge transport material.[14] A thin-film perovskite solar cell without a mesoporous scaffold was constructed that demonstrated solar efficiency greater than 10%.[14b, 15] Burschka et al. showed that the deposition technique

efficiency of a sensitised architecture exceeded 15% using a two-step solution processing method.[16] Meanwhile, Olga Malinkiewicz et al. and Liu et al. demonstrated that planar solar cells could be fabricated by thermal co-evaporation in a p-i-n and an n-i-p architecture, achieving efficiencies greater than 12% and 15%, respectively.[13c, 17] As a result of intensive research efforts, in 2018, a perovskite solar cell was reported by the Chinese Academy of Sciences (ISCAS) to have achieved an efficiency of 23.3%. This finding was certified by the NREL, as displayed in Figure 1.2.[8d]
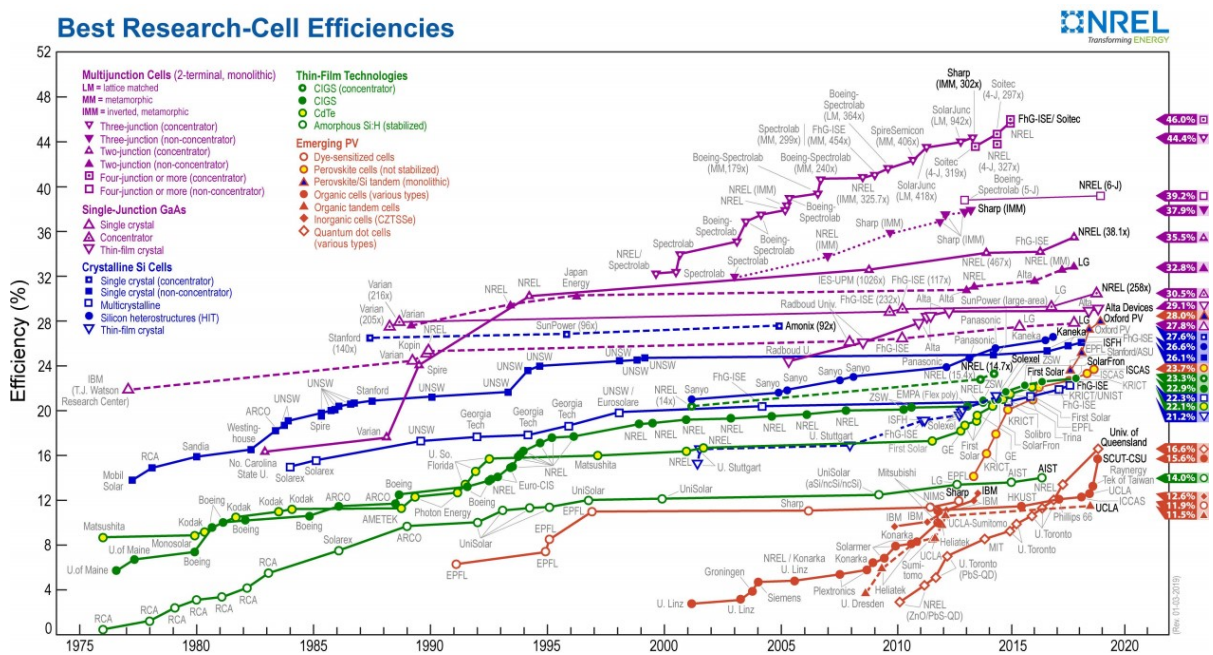
Figure 1.2 NREL efficiency chart of certified research for solar cell efficiencies over time. (Figure source: https://www.nrel.gov/pv/assets/pdfs/pv-efficiency-chart.20181221.pdf)

1.2. General overview and important concepts

1.2.1. Perovskite structure

AMX$_3$-type organometallic halide perovskites, whose structure is explained in Figure 1.3 and 2.1,[18] are now leading materials for solar energy conversion device development because of their high device performance, good optoelectronic properties and their potential for low-temperature device manufacturing.[19]
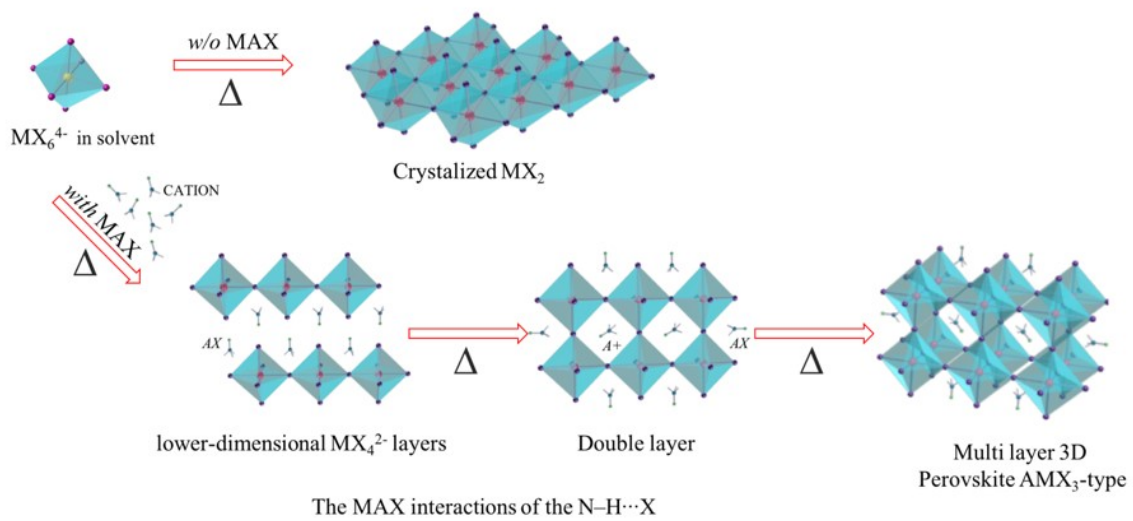
Figure 1.3 Schematic crystal structure of the AMX$_3$-type organometallic halide perovskite structure. Transition from 1D to 3D perovskite structure used for photovoltaics. This structure is stable only with the aid of MAX due to its size. (A=CH$_3$NH$_3$ or any other cation on the corner and M=M^{2+} ion at the centre of the lattice)

AMX$_3$-type organohalide perovskite films are generally fabricated from a precursor solution containing stoichiometric amounts of metal halide (MX$_6^{4-}$) (M=M^{2+} metal ion, X=Cl, Br, I) and organic cations (CH$_3$NH$_3^+$(X$^-$)) for site A. Figure 1.3 shows schematic drawing of the formation of 3D perovskite structure. The small organic cation occupying the vacancies of the polytetrahedron initiates the formation of a low-dimensional perovskite. As a result, lower-dimensional MX$_4^{2-}$ layers form, with further interactions resulting in an eight corner-sharing octahedral 3-D perovskite crystal. However, without the organic cation, MX$_6^{4-}$ can only form a metal halide (MX$_2$) crystal structure. This perovskite structure has been studied for over 80

years and has been shown to display excellent optoelectronic behaviour.[18a, 20] In the 3-D perovskite structure, it has been widely studied that the optical bandgap could be affected by halogen atoms such as iodine, bromine or chlorine for methylammonium lead trihalide. The optical bandgap shifts from about 1.5 to 2.3 eV depending on the halide content. The role of the organic cation is known to indirectly influence the band structure.[21] In the $MAPI_3$ crystal, weak hydrogen bonding forms between the ammonium head(s) of the organic cation and the eight halides.[21e] In this AMX_3, the perovskite structure and the size of the ions can press the lattice, which results in M–X bond length deformations. The tolerance factor (t) is a geometric parameter ($t = (R_A + R_X)/[\sqrt{2}(R_M + R_X)]$), where R_A, R_M and R_X are the radii of the corresponding ions, which is often used to classify the lattice structure. When the value of t is close to 1, the perovskite tends to follow an ideal cubic structure, whereas when this value is smaller than 1, the structure is distorted into a low-symmetry structure, such as a tetragonal or orthorhombic.[22] Additionally, phase transitions are also known to occur by varying the sample temperature.[23] As a result, $MAPI_3$ perovskites have a tetragonal structure at room temperature that affects the band gap energy.[18d, 24] The $MAPI_3$ perovskite used in this study (PbI_2 as the lead halide with MAI as the centre cation) shows a narrow band gap of 1.55 eV and a high extinction coefficient.[25] Thus, it was one of the most successfully applied perovskite materials as a light absorber in a solar cell system.[14a, 26] For simplicity, hereafter in this thesis, the term 'perovskite' will refer to $MAPI_3$ specifically.

1.3. Photophysics background relevant to perovskite materials

1.3.1. Excitons, charge separation and the invention of the perovskite cell

In photovoltaic devices, photons' energy is absorbed by a light-absorbing material. The electrons in the ground-state that absorb these photons jump into their excited-state and electron-hole pairs are thereby generated. If the dielectric constant is small, for example in an organic semiconducting material, the electron–hole binding energy is relatively high, causing these electron–hole pairs to be bound as excitons by electrostatic attraction.[27] Therefore, to obtain free charge carriers in such materials, excitons need an energy offset to overcome this binding energy. Thus, they typically diffuse to an interface between the donor and acceptor materials and dissociate. In the case of perovskite materials, their large dielectric constant leads to a low exciton binding energy (for MAPI$_3$, below 50 meV at room temperature).[28] Perovskite excitons are therefore easily dissociated by thermal energy at room temperature and form free electron and hole carriers. Finally, the charge carriers, electrons and holes, are collected by an external circuit. Organic-inorganic halide perovskites have been previously shown to act as not only the light-absorbing material, but also the ambipolar charge transporter. Moreover, free charge carriers and weakly bound excitons seem to coexist with the exited state population, interchanging and decaying over a similar timescale.[29] To ensure selective charge extraction/transfer, heterojunctions for the electron and hole transport layers are generally interposed between the electrode and the perovskite layer (as will be explained further below).

1.3.2. Vibrational and electronic transitions and photoluminescence spectra

1.3.2.1. Charge-carrier recombination mechanisms in semiconductors (photophysical processes in a pristine film)

The absorption of photons causes electrons to move from the valence band (VB) to the conduction band (CB), forming electron–hole pairs. In perovskite materials, these electron–

hole pairs typically spontaneously dissociate into free carriers.[30] Recombination of these electrons and holes occurs where these two carriers annihilate each other. Depending on whether the energy released by this recombination is emitted in the form of a photon or heat, the recombination processes can be classified as either a radiative recombination or a non-radiative recombination.[31]
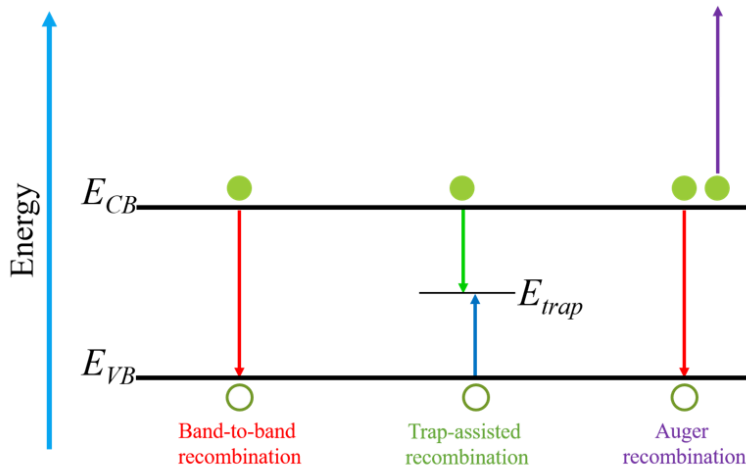
Figure 1.4 Carrier recombination mechanisms in semiconductors

Different recombination pathways are illustrated in Figure 1.4 Free carrier band-to-band recombination is often referred to as radiative bimolecular recombination. Trap-assisted recombination (one particle involved, non-radiative monomolecular recombination) can be based on the Shockley-Read-Hall (SRH) model via a mid-band energy level E_{trap} (deep-level trap). This can be thought of as a two-step transition of an electron from the CB to the VB. In case of Auger recombination, which is a non-radiative recombination involving the interaction of three particles (two electrons (or holes) and a hole (or electron)), electrons and holes directly recombine as in band-to-band recombination, while energy is delivered to another free carrier. [31-32] In perovskite, the recombination dynamics of bulk films are generally known to be related to SRH-like monomolecular recombination, free electron hole bimolecular recombination and Auger recombination.[33] The charge recombination rate is simply expressed by the following

rate equation (1)

$$R_{T} = k_1 + nk_2 + n^2 k_3,$$ (1)

where R_T is the total recombination rate, n is the charge-carrier density, k_1 is the monomolecular recombination rate constant, k_2 is the bimolecular recombination rate constant and k_3 is the Auger recombination rate constant.[33b] However, in perovskite films, bimolecular recombination via trapping and reversible trapping (de-trapping) process via a shallow trap state (or defect) is known to be favourable.[33d, 34] The shallow defect doped in the material could not be an non-radiative recombination centre in the perovskite film.[35] Auger recombination activates at very high charge densities ($\geq$2-5E^{18} cm^{-3}),[31, 36] thus it could be ignored in this thesis on solar cell devices. The details of the nonlinear recombination behaviour of perovskite films will be described in chapter 3.

1.3.2.2. Direct and indirect properties of semiconductors for PV
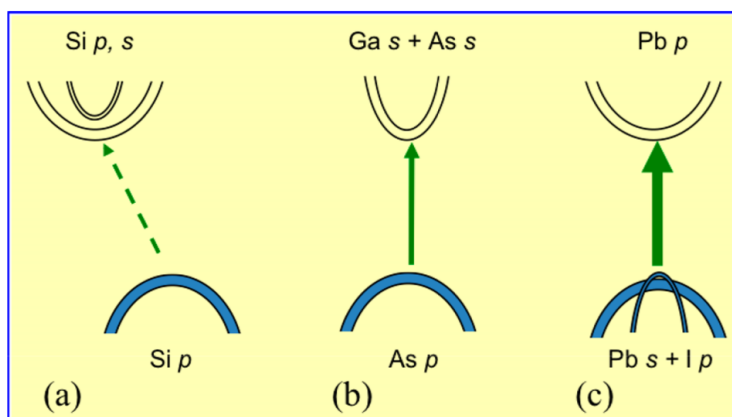
*Figure 1.5 Schematic of optical absorption transitions of a) Si; b)GaAs and c)MAPI₃. (Figure source: The Journal of Physical Chemistry C. **2015**, 119, 5253)* [37]

Figures 1.5a and 1.5b show schematics of the optical absorption transitions of Si and GaAs, the two-representative inorganic photovoltaic absorber materials. From the viewpoint of the joint density of states, CB and VB, Si is preferable over GaAs because the s orbital is more dispersed than the p orbital.[37-38] However, there is an indirect gap in Si, in which case, the optical transition between the VB and CB edges is a phonon-assisted transition, resulting in relatively low optical absorption near the edges of the band. By combining the properties of Si and GaAs, namely, p–p transitions and direct band gaps, respectively, the optical absorption can be ideal and more efficient. The p–p transition can only be applied to compound semiconductors that contain cationic elements exhibiting lone pairs of electrons, such as Ge(2), Sn(2), Pb(2), Sb(3) and Bi(3). For example, a p–p transition may occur in compound semiconductors such as SnS, PbS, Sb_2Se_3 and Bi_2S_3. However, most of these compounds typically have low symmetry and therefore have indirect-band-gaps.[37-38]

In case of $MAPI_3$ perovskite, it not only has a p–p transition but also has a direct-band-gap due to the organic/inorganic hybrid chemical structure, resulting in efficient optical absorption, as shown in Figure 1.5c. Therefore, due to the Pb lone pair s orbitals and the perovskite symmetry, the optical absorption coefficient of lead halide perovskite is expected be high.
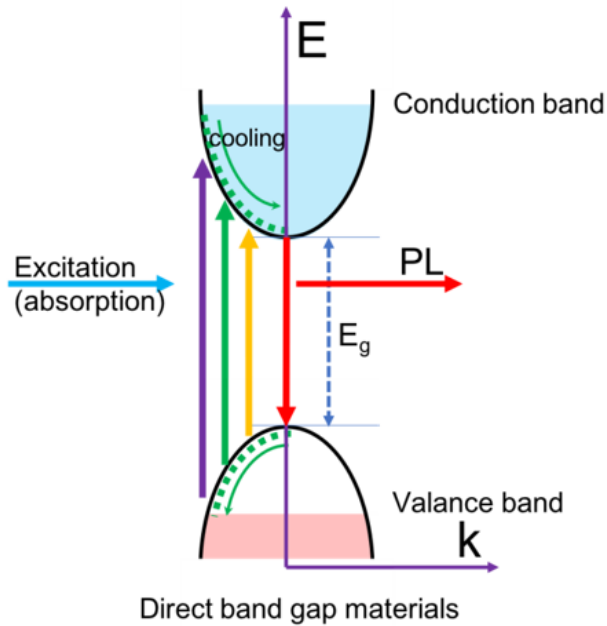
Figure 1.6 Schematic of E–k band diagram of the photoluminescence process in direct-band-gap semiconductor materials.

The photoluminescence (PL) mechanism in a direct-band-gap semiconductor is schematically illustrated in Figure 1.6, which plots an E–k plot of a direct bandgap material, where E and k are the orbital energy and wave vectors respectively. In the case of direct gap material, both the CB minimum and the VB maximum appear at the center of the region, where k = 0. When the absorbed UV- or visible-light energy exceeds the band gap (E_g) of the material (the energy gap between the VB and the CB), an electron–hole pair is generated and the electron (hole) is excited to a higher conduction (valence) band. These unstable excited electrons and holes undergo energy and momentum relaxation (cooling) towards the CB minimum and VB maximum, respectively. The electrons on CB recombine with the holes on VB, and then the decay can result in photon emission (fluorescence). The fluorescence or photoluminescence energy can be lower than the excitation energy, and the fluorescence wavelength is greater than the excitation wavelength.

PL spectroscopy is a commonly used technique to study excited state properties in semiconductor films and its devices. However, studying the PL of perovskite films remains challenging as the reproducibility or repeatability of the PL intensity can be poor, because the PL intensity of the film can be affected by several factors including crystallinity, morphology and trap state densities.[39] Furthermore, the PL is dependent on the humidity/temperature and atmosphere both in manufacture and in measurement.[39] For example, during the doctoral studies reported herein, it was often observed that the PL intensity of $MAPI_3$ was very variable between different measurements, attributed in part to issues of reproducibility of film processing but also to temporal evolution of PL intensity following film formation. This unstable optical property of perovskite will be discussed in more depth in chapter 4.

In perovskite systems, both absorption and emission transient spectroscopy have been widely used to study the ground- and excited-state dynamics, such as determining diffusion lengths and charge extraction yields.[29, 40]
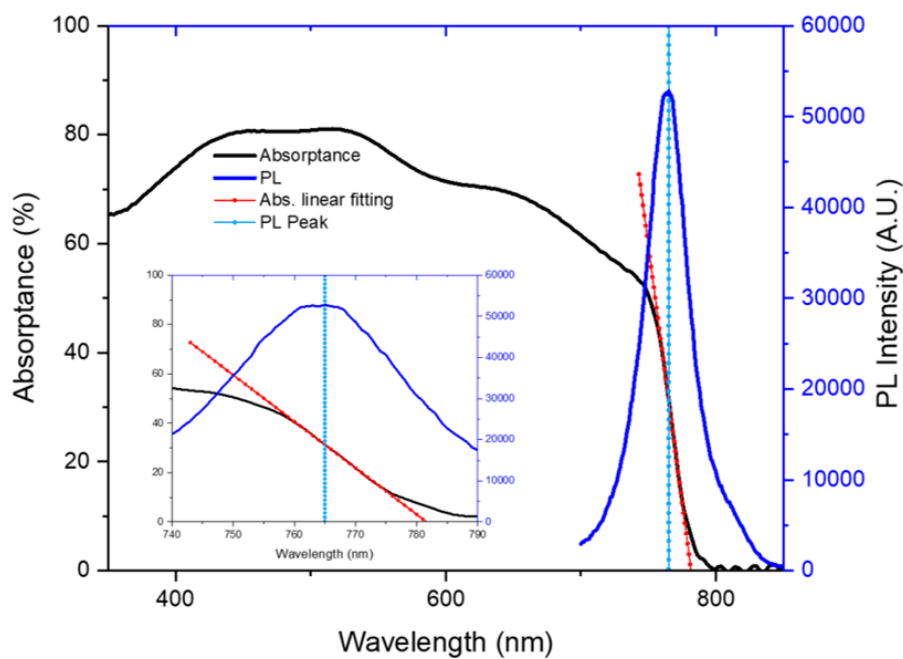
Figure 1.7 Absorptance spectrum (black line), emission spectrum (blue line peaks at 764 nm) of ~300-nm-thick toluene-treated MAPI$_3$ films on glass. Inset shows a fitting line of the onset of the absorptance and PL peak position.

Figure 1.7 shows the strong visible-range absorptance of the MAPI$_3$ perovskite film. The absorptance onset is at 781 nm with a band edge emission peak near 765 nm, which indicates

E_g. The ground-state absorptance spectrum of MAPI$_3$ (black line) shows a continuous absorption band because the light energy that exceeds E_g is also absorbed as described above.
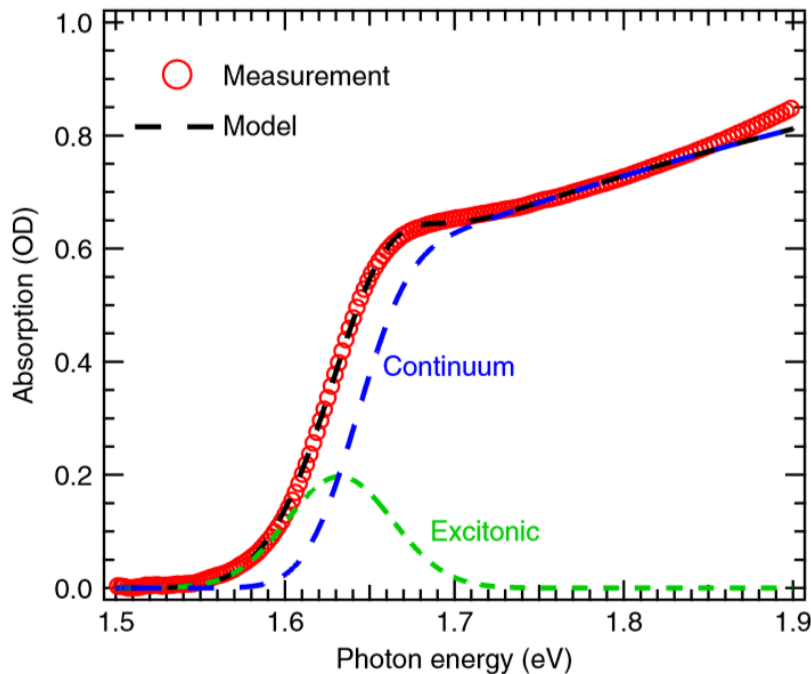
Figure 1.8 Absorption spectrum of MAPI$_3$ film (red circles), and Elliott's model (black dashed line), the excitonic contribution (green dashed line) and the continuum absorption band (blue dashed line). (Figure source; Nature Communications volume 7, Article number: 12613 (2016))[40]

In perovskite, the absorbed photons form free charge carriers and the weakly bonded excitons that seem to coexist as described above.[29] In Figure 1.8, the MAPI$_3$ absorption spectrum (red circles) data obtained by Yang et al. is fitted by Elliott's model (black dashed line),[42c] in which the electrons and holes are treated by Coulombic interactions.[33c, 41-42] In this model, sharp excitonic and continuum absorption spectra can be decoupled. The excitonic signal peaks at 1.63 eV (760 nm) and the continuum transitions, collected from spectral onset, is 1.64 eV (755 nm). Perovskite is generally considered to be a direct bandgap material because its absorption coefficient in the visible spectrum is greater than 10^4 cm^{-1}. This requires a direct optical transition oscillator strength. Typically, the PL peak is centred close to the absorption onset

because of its direct-band-gap structure.[43] In our MAPI$_3$ film, a slight mismatch between the PL peak and the absorption onset of around 33 meV is observed. There are reports about the existence of a sub-conduction or valance band states or an indirect band structure resulting from the rotation of the methylammonium in the MAPI$_3$ film, which may influence the band structure.[21a, 44] In this thesis, phosphorescence will not be considered since PL in perovskite is generally only observed in lower-dimensional perovskites, which are generally used for emission devices[45] (not PV devices) involving organic ammonium molecules with a functional group such as a π-conjugated chromophore as an organic layer.[46]

1.3.2.3. Photoluminescence excitation intensity dependency measurements.

Photoluminescence excitation intensity (I_{exc})-dependent emission intensity (I_{emi}) measurements can be used to probe the relevant recombination pathways of the photogenerated carriers in perovskite materials since the emission intensity experimentally increases in a power law manner (i.e., $I_{emi} \propto I_{exc}{}^b$, where the power law coefficient b may reflect the underlying carrier recombination processes).[47] The competition between carrier trapping and bimolecular electron/hole recombination can change the order of emission growth. Figure 1.9 shows the results of typical I_{exc}-dependent I_{emi} measurements performed on ~10-nm-thick MAPI$_3$ films and a single MAPI$_3$ crystal from the literature.[47]
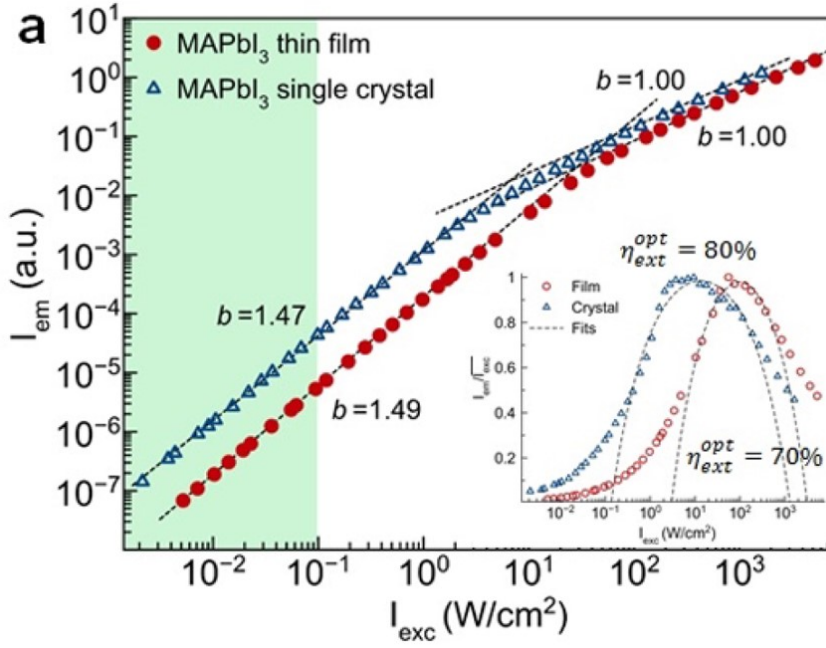
Figure 1.9 I_{exc}-dependent I_{emi} measurements performed on MAPI$_3$ single crystals (blue triangles) and films (red circles). The dot line shows linear fitting on log–log plot at high and low excitation density. (inset) Emission Quantum yields of the corresponding samples (Figure source; J. Phys. Chem. Lett. 2016, 7, 715−721)[47]

Examining the curve further, a power law b smaller than 1 may indicate direct electron−hole recombination (bimolecular recombination). The ideal bimolecular recombination should give power law decays with a gradient of 1, with deviations from this bimolecular behaviour being indicative of other processes. Trapping of both photogenerated electrons and holes has been suggested to lead to superlinear (quadratic) growth of I_{emi} (i.e., $I_{emi} \propto I_{exc}^2$, $b = 2.0$) because the defect trapping has a higher rate than bimolecular recombination.[47-48] With an increase in excitation density, the impact of such defective states has been observed to decrease due to trap filling; thus, the value of b also decreases. Experimentally, if continuous wave (CW) excitation is used, at low excitation densities, a gradient b of 1.5 is normally observed. In pulsed measurements, a higher number of ~1.8 is often observed experimentally.[49] Draguta et al. and Wen et al. suggested that the power law coefficients observed in I_{emi}–I_{exc} diagrams can be used to infer carrier recombination mechanisms in MAPI$_3$ films, the participation of sub gap states, and occasionally, the nature of the excited species (free carriers or excitons).[48-49]
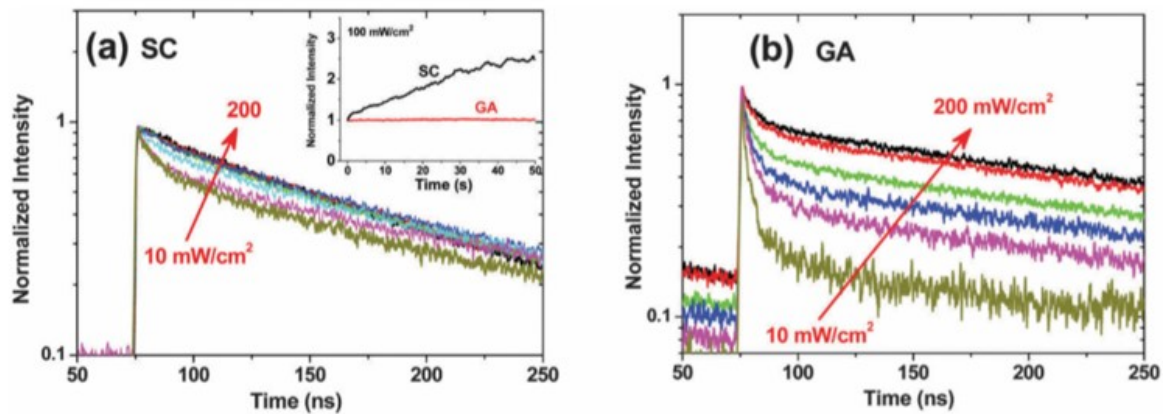
Figure 1.10 PL transient dynamics of a) spin coated (SC) and b) gas-assisted (GA) MAPI₃ perovskite film measured with various excitation densities from 10 to 200 mW cm⁻². a) inset, steady-state PL-intensity monitoring of SC and GA samples under low excitation density as 100 mW cm⁻². (Figure source; J. Mater. Chem. C. 2016, 4, 793)[48]

To study charge-carrier dynamics related to the trap state dynamics of perovskite, transient PL (tr-PL) spectroscopy is commonly employed. Time-correlated singe-photon counting (TCSPC) measurements have been used since they can provide very sensitive PL transient measurements at a very low excitation density. Figure 1.10a and 1.10b show examples of tr-PL decays for neat MAPI₃ films that have different trap densities with various excitation densities.[48] The TCSPC decays are commonly fitted to a biexponential ($y=A_1 \exp(-\tau / \tau_1)+A_2 \exp(-\tau / \tau_2)$) expression to quantify the amplitude of the fast and slow components. The fast (τ_1) and slow (τ_2) components are assigned to monomolecular and bimolecular recombination of the free charge-carrier, respectively. The fast component has been assigned to carrier trapping into defect sites.[44a, 50] In lower charge-carrier excitation density, the charge-carrier trapping dominates the PL decay, while the lifetime and weight of the second component (assigned as bimolecular recombination) increases and the weight of the fast component decreases as the excitation density is increased. This result shows the importance of excitation density for understanding perovskite solar cell device mechanisms that operate in higher charge-carrier densities, such as 1 sun. Moreover, the relationship between the recombination processes and

excitation density could be affected by the trap states density of the film.[48, 51] As an example, two different trap density samples measured using TCSPC with various excitation densities are displayed in Figure 1.10 a and b. The gas-assisted (GA) sample in 10b (which has a larger trap density $N_t = 1.04 \times 10^{17}$) has a larger fast component and shorter lifetimes compared with the spin coated (SC) sample ($N_t = 7.44 \times 10^{16}$) in 10a. The higher trap density sample shows more effective defect trapping at low excitation densities, but this trapping process is suppressed with increasing excitation density (see Figure 10c). However, it is unclear why the SC samples show PL intensity increases over time, but the GA samples do not (see Figure 1.10a inset). The unstable or light curing/healing properties of MAPI$_3$ PL is a significant issue for many studies and may relate to trap densities evolving with time.[45b] The importance of these different recombination pathways in limiting the performance of perovskite solar cells is discussed in detail in chapter 3.

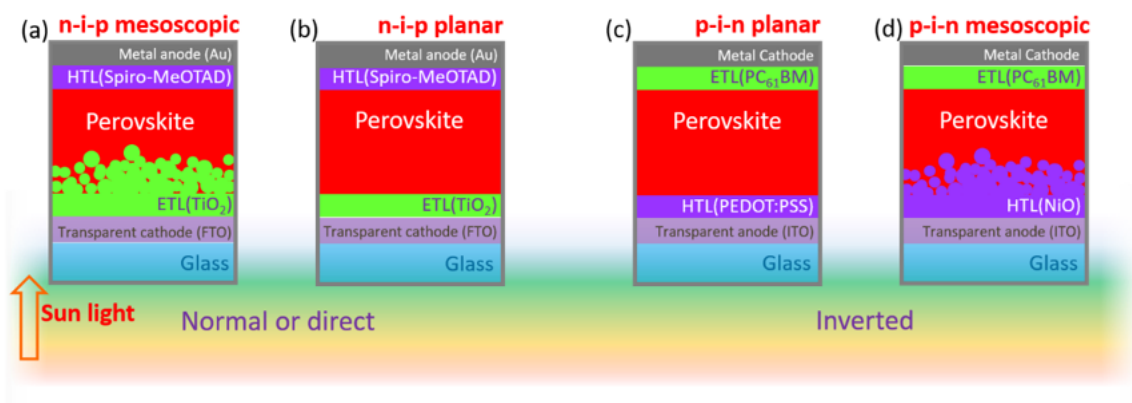### 1.3.3. Electron and hole collection strategies for perovskite solar cells

Figure 1.11 Schematics of perovskite solar cells in: (a) n-i-p mesoscopic; (b) n-i-p planar; (c) p-i-n planar; and (d) p-i-n mesoscopic structures. (a, b) Normal device structure; and (c, d) inverted device structure.

Figure 1.11 shows the four major device structures used for perovskite solar cells. Each perovskite solar cell device consists of six basic components: a perovskite layer where light absorption occurs; two transport interfaces (electron-transporting material, ETM, and hole-transporting material, HTM) where charge is collected; two electrodes (a transparent electrode and a metallic electrode where charge is transferred to the external circuit); and a glass (or plastic) substrate. The ETM and HTM layers are necessary for improving the selectivity of charge collection for the respective electrodes.[52] The first two perovskite device structures are referred to as 'normal or direct' device structures, with direct parallels to DSSCs employing nanocrystalline TiO_2.[12, 14a, 33c] In the n-i-p mesoscopic structure, the light-harvesting dye is replaced by the halide perovskite semiconductor. Instead of a liquid electrolyte, a solid-state hole conductor is used.[53] The mesoscopic structure is the standard structure of a perovskite solar cell from which other structures have evolved. In a planar device structure, the perovskite light absorber is found sandwiched between the ETM and HTM. If the HTM is on top of the perovskite absorber and the ETM is below, it forms an n-i-p structure (a normal device); if the opposite configuration is employed, it becomes a p-i-n structure (an inverted device).[54] Detailed studies of the electron and hole transfer dynamics will be discussed in chapter 3. p-i-n-structured perovskite solar cells typically show slightly lower efficiencies than devices with mesoporous ETM layer but are promising since they show less hysteresis during device operation and are favourable for further applications, such as tandem and integrated structure solar cells, as will be discussed in chapter 5. Additionally, lesser hysteresis of p-i-n perovskite solar cell allows the simplification of optical analyses because the hysteresis of the device, which could be changed by ionic accumulation, photo voltage and internal fields, changes the charge transport properties, which in turn relate to charge life time, transfer yield and mobility.[55]
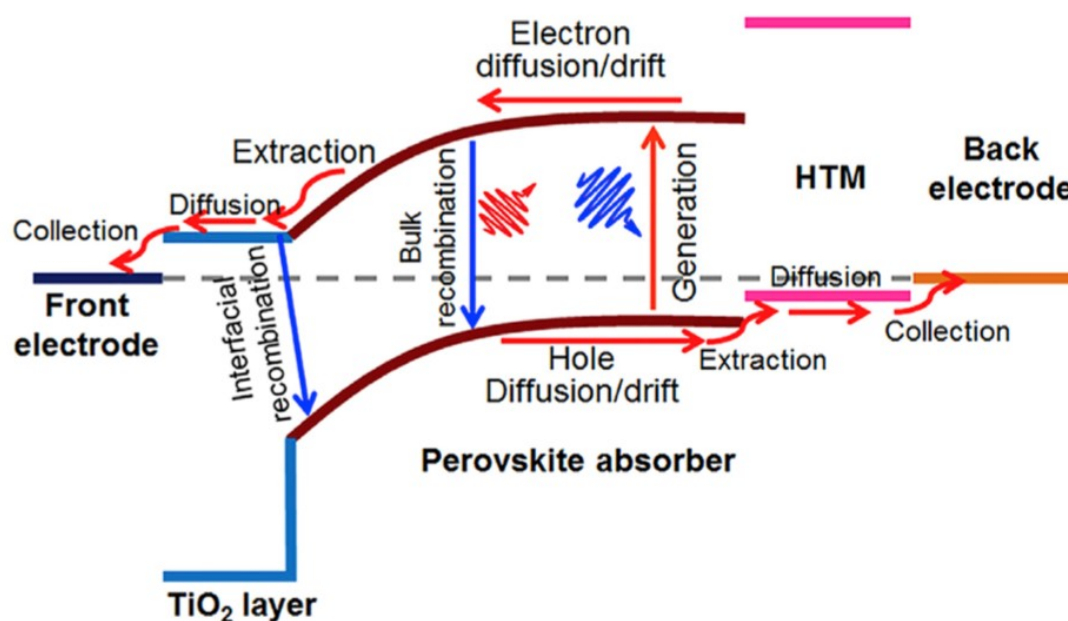
*Figure 1.12 Possible charge processes of the perovskite solar cells. (Figure source; Joule. **2018**, 2, 879.)[56]*

Figure 1.12 shows the schematic of the charge transfer processes in a conventional perovskite device and the corresponding timescale. As described above, the absorbed photons generate the exciton and subsequently, free charge carriers, in a timescale ranging from femtosecond to picosecond.[56-57] Generally, the electron and hole are transported to ETL and HTL within several nanoseconds through the bulk by diffusion or drift and then extracted (transferred) by the transfer materials usually within several microseconds.[29, 56, 58] Since the exciton and free charge generation is relatively efficient in perovskite devices, this timeline of the transfer dynamics has been widely studied using transient absorption and PL spectroscopy.[47, 49b, 59] During these processes, bulk and interfacial recombination occurs and could limit the performance. However, long charge-carrier lifetimes extending up to several microseconds and good charge-carrier mobility are known to minimize the bulk recombination, whose details will be described in chapter 3.

1.4. Objectives of the thesis and areas of research addressed

The main objective in this thesis is the characterisation and understanding of the charge transfer between $MAPI_3$ and ETM or HTM. The neat $MAPI_3$ films and the junction structure (with electron and hole transport layers) were studied with techniques including photoluminescence (PL), tr-PL, transient absorption (TA), and UV-vis spectroscopies. These techniques were used to understand the photophysical properties of the material, to explain the charge-carrier dynamics in perovskite and how these factors impact device performance.

Previous literature on many of these parameters, particularly including carrier and transfer lifetimes as well as PL intensity, has reported a wide range of values.[31, 59a, 60] These variations may reflect different material processing and device structures, the reproducibility of samples and/or repeatability of the measurements. Thus, this thesis will explore the correlations between the electronic properties of the $MAPI_3$ perovskite material, optical measurements and the sample preparation conditions and techniques.

In chapter 3, the first chapter that presents results, the charge-carrier density-dependent bimolecular recombination kinetics of $MAPI_3$ perovskite, compete with charge transfer at light fluxes approaching 1 sun, are discussed. The excitation density dependence of the PL properties of $MAPI_3$ films and the photoluminescence quenching efficiency (PLQE) of the perovskite in junctions with Poly(3,4-ethylenedioxythiophene) polystyrene sulfonate (PEDOT:PSS) and $PC_{61}BM$ (hole and electron acceptors, respectively) will be investigated using ground-state optical spectroscopy in combination with femtosecond transient absorption spectroscopy (fs-TAS) and tr-PL. This allows the excited-state dynamics in these perovskite films and their interfaces with charge extracting layers to be unravelled. In chapter 4, the $MAPI_3$ PL instability

issues will be discussed. The origin of the PL change of MAPI$_3$ perovskite films stored within nitrogen in the dark will be investigated. UV-Vis spectroscopy, transient absorption spectroscopy (TAS), TCSPC, X-Ray diffraction (XRD) and atomic force microscopy (AFM) will be used to unveil the aging effect of neat MAPI$_3$ film. The study allows to study perovskite recrystallization processes while stored in dark without oxygen at room temperature and to determine the cause of optical property changes. Finally, the charge-carrier dynamics of the more complicated perovskite/organic integrated device will be discussed in chapter 5. In this perovskite and organic photovoltaic (OPV)-junction structured device, the charge-carrier transfer behaviours are known to be more complicated to study by using fs-TAS. The detailed charge-carrier transfer process will be studied with not only bilayer film, but also multi-layer and even full device samples based on the previous knowledge explained in chapter 3.

1.5. Reference

[1]   IEA,   Key   World   Energy   Statistics   2018, https://webstore.iea.org/download/direct/2291?fileName=Key_World_2018.pdf, accessed: 1024, 2018.

[2]   CGD,   Electricity   Consumption   and   Development   Indicators, https://www.cgdev.org/media/electricity-consumption-and-development-indicators, accessed: 0808, 2018.

[3]   P. A. Owusu, S. Asumadu-Sarkodie, S. Dubey, *Cogent Engineering.* **2016**, 3.

[4]   B. R. Anthony Lopez, Donna Heimiller, Nate Blair, and Gian Porr, NREL 2012.

[5]   a) A. Bhuwalka, J. F. Mike, M. He, J. J. Intemann, T. Nelson, M. D. Ewan, R. A. Roggers, Z. Lin, M. Jeffries-El, *Macromolecules.* **2011**, 44, 9611; b) G. Li, V. Shrotriya, J. Huang, Y. Yao, T. Moriarty, K. Emery, Y. Yang, *Nature Materials.* **2005**, 4, 864; c) A. Shah, P. Torres, R. Tscharner, N. Wyrsch, H. Keppner, *Science.* **1999**, 285, 692.

[6]   a) M. He, D. Zheng, M. Wang, C. Lin, Z. Lin, *J Mater Chem A.* **2014**, 2, 5994; b) M. A. Green, K. Emery, Y. Hishikawa, W. Warta, E. D. Dunlop, *Progress in Photovoltaics: Research and Applications.* **2015**, 23, 1; c) A. Yella, H. W. Lee, H. N. Tsao, C. Yi, A. K. Chandiran, M. K. Nazeeruddin, E. W. Diau, C. Y. Yeh, S. M. Zakeeruddin, M. Gratzel, *Science.* **2011**, 334, 629; d) S. Strehlke, D. Sarti, A. Krotkus, K. Grigoras, C. Lévy-Clément, *Thin Solid Films.* **1997**, 297, 291.

[7]   a) S.-I. Na, S.-S. Kim, J. Jo, D.-Y. Kim, *Advanced Materials.* **2008**, 20, 4061; b) S. Gunes, H. Neugebauer, N. S. Sariciftci, *Chemical Reviews.* **2007**, 107, 1324; c) Y. Kim, S. Cook, S. M. Tuladhar, S. A. Choulis, J. Nelson, J. R. Durrant, D. D. C. Bradley, M. Giles, I. McCulloch, C.-S. Ha, M. Ree, *Nature Materials.* **2006**, 5, 197.

[8]   a) Y. Rong, Z. Tang, Y. Zhao, X. Zhong, S. Venkatesan, H. Graham, M. Patton, Y. Jing, A. M. Guloy, Y. Yao, *Nanoscale.* **2015**, 7, 10595; b) H. Zhang, J. Mao, H. He, D. Zhang, H. L. Zhu, F. Xie, K. S. Wong, M. Grätzel, W. C. H. Choy, *Advanced Energy Materials.* **2015**, 5, 1501354; c) X. Li, D. Bi, C. Yi, J. D. Decoppet, J. Luo, S. M. Zakeeruddin, A. Hagfeldt, M. Gratzel, *Science.* **2016**, 353, 58; d) NREL, Best Research-Cell efficiencies, https://www.nrel.gov/pv/assets/pdfs/pv-efficiency-chart.20181221.pdf, accessed: 01, 2019; e) S. S. Shin, E. J. Yeom, W. S. Yang, S. Hur, M. G. Kim, J. Im, J. Seo, J. H. Noh, S. I. Seok, *Science.* **2017**, 356, 167; f) M. Saliba, T. Matsui, J. Y. Seo, K. Domanski, J. P. Correa-Baena, M. K. Nazeeruddin, S. M. Zakeeruddin, W. Tress, A. Abate, A. Hagfeldt, M. Gratzel, *Energy & Environmental Science.* **2016**, 9, 1989.

[9]   A. Kojima, K. Teshima, Y. Shirai, T. Miyasaka, *Journal of the American Chemical Society.* **2009**, 131, 6050.

[10]   B. O'Regan, M. Grätzel, *Nature.* **1991**, 353, 737.

[11]   a) Y. S. Kwon, J. Lim, I. Song, I. Y. Song, W. S. Shin, S.-J. Moon, T. Park, *J Mater Chem.* **2012**, 22, 8641; b) U. Bach, D. Lupo, P. Comte, J. E. Moser, F. Weissortel, J. Salbeck, H. Spreitzer, M. Gratzel, *Nature.* **1998**, 395, 583; c) N. Cai, S. J. Moon, L. Cevey-Ha, T. Moehl, R. Humphry-Baker, P. Wang, S. M. Zakeeruddin, M. Gratzel, *Nano Letters.* **2011**, 11, 1452.

[12]   H. S. Kim, C. R. Lee, J. H. Im, K. B. Lee, T. Moehl, A. Marchioro, S. J. Moon, R. Humphry-Baker, J. H. Yum, J. E. Moser, M. Gratzel, N. G. Park, *Sci Rep.* **2012**, 2, 591.

[13]   a) D. Liu, T. L. Kelly, *Nature Photonics.* **2013**, 8, 133; b) C. C. Stoumpos, C. D. Malliakas, M. G. Kanatzidis, *Inorganic Chemistry.* **2013**, 52, 9019; c) M. Liu, M. B. Johnston, H. J. Snaith, *Nature.* **2013**, 501, 395.

[14]   a) M. M. Lee, J. Teuscher, T. Miyasaka, T. N. Murakami, H. J. Snaith, *Science.* **2012**, 338, 643; b) J. M. Ball, M. M. Lee, A. Hey, H. J. Snaith, *Energy & Environmental Science.* **2013**, 6.

[15]   P. Docampo, J. M. Ball, M. Darwich, G. E. Eperon, H. J. Snaith, *Nature Communications.* **2013**, 4, 2761.

[16]   J. Burschka, N. Pellet, S. J. Moon, R. Humphry-Baker, P. Gao, M. K. Nazeeruddin, M. Gratzel, *Nature.* **2013**, 499, 316.

[17]   O. Malinkiewicz, A. Yella, Y. H. Lee, G. M. Espallargas, M. Graetzel, M. K. Nazeeruddin, H. J. Bolink, *Nature Photonics.* **2013**, 8, 128.

[18]   a) H. D. Megaw, *Nature.* **1945**, 155, 484; b) W. F. Forrester, R. M. Hinde, *Nature.* **1945**, 156, 177; c) F. Hao, C. C. Stoumpos, Z. Liu, R. P. Chang, M. G. Kanatzidis, *J Am Chem Soc.* **2014**, 136, 16411; d) R. E. Schaak, T. E. Mallouk, *Chem Mater.* **2002**, 14, 1455; e) P. Gao, M. Grätzel, M. K. Nazeeruddin, *Energy & Environmental Science.* **2014**, 7, 2448; f) N. G. Park, *Journal of Physical Chemistry Letters.* **2013**, 4, 2423.

[19]   M. A. Green, A. Ho-Baillie, H. J. Snaith, *Nature Photonics.* **2014**, 8, 506.

[20]   a) V. M. Goldschmidt, *Die Naturwissenschaften.* **1926**, 14, 477; b) I. V. Veksler, M. P. Teptelev, *Lithos.* **1990**, 26, 177; c) G. V. Liberts, V. Y. Fritsberg, *Physica Status Solidi (a).* **1981**, 67, K81.

[21]   a) C. Motta, F. El-Mellouhi, S. Kais, N. Tabet, F. Alharbi, S. Sanvito, *Nature Communications.* **2015**, 6, 7026; b) F. Sani, S. Shafie, H. N. Lim, A. O. Musa, *Materials (Basel).* **2018**, 11; c) A. M. Ganose, C. N. Savory, D. O. Scanlon, *Chemical Communications.* **2016**, 53, 20; d) G. Giorgi, J.-I. Fujisawa, H. Segawa, K. Yamashita, *The Journal of Physical Chemistry C.* **2014**, 118, 12176; e) David B. Mitzi, *Journal of the Chemical Society, Dalton Transactions.* **2001**, 0, 1-12.

[22]   a) Z. Fan, K. Sun, J. Wang, *J Mater Chem A.* **2015**, 3, 18809; b) S. Catalano, M. Gibert, J. Fowlie, J. Iniguez, J. M. Triscone, J. Kreisel, *Reports on Progress in Physics.* **2018**, 81, 046501.

[23]   R. L. Milot, G. E. Eperon, H. J. Snaith, M. B. Johnston, L. M. Herz, *Advanced Functional Materials.* **2015**, 25, 6218.

[24]   G. E. Eperon, S. D. Stranks, C. Menelaou, M. B. Johnston, L. M. Herz, H. J. Snaith, *Energy & Environmental Science.* **2014**, 7, 982.

[25]   T. Supasai, N. Rujisamphan, K. Ullrich, A. Chemseddine, T. Dittrich, *Appl Phys Lett.* **2013**, 103, 183906.

[26]   a) N. J. Jeon, J. H. Noh, Y. C. Kim, W. S. Yang, S. Ryu, S. I. Seok, *Nature Materials.* **2014**, 13, 897; b) J. H. Im, I. H. Jang, N. Pellet, M. Gratzel, N. G. Park, *Nature Nanotechnology.* **2014**, 9, 927; c) Z. Xiao, C. Bi, Y. Shao, Q. Dong, Q. Wang, Y. Yuan, C. Wang, Y. Gao, J. Huang, *Energy & Environmental Science.* **2014**, 7, 2619.

[27]   J. Nelson, *The Physics of solar cells*, Imperial College Press, **2003**.

[28]   a) A. Jha, H.-G. Duan, V. Tiwari, P. K. Nayak, H. J. Snaith, M. Thorwart, R. J. D. Miller, *ACS Photonics.* **2017**, 5, 852; b) F. D. Fuller, J. Pan, A. Gelzinis, V. Butkus, S. S. Senlik, D. E. Wilcox, C. F. Yocum, L. Valkunas, D. Abramavicius, J. P. Ogilvie, *Nature Chemistry.* **2014**, 6, 706; c) S. A. March, C. Clegg, D. B. Riley, D. Webber, I. G. Hill, K. C. Hall, *Scientific Reports.* **2016**, 6, 39139; d) K. Tanaka, T. Takahashi, T. Ban, T. Kondo, K. Uchida, N. Miura, *Solid State Communications.* **2003**, 127, 619.

[29]   S. D. Stranks, G. E. Eperon, G. Grancini, C. Menelaou, M. J. Alcocer, T. Leijtens, L. M. Herz, A. Petrozza, H. J. Snaith, *Science.* **2013**, 342, 341.

[30]   G. H. Wannier, *Physical Review.* **1937**, 52, 191.

[31]   T. C. Sum, N. Mathews, *Energy & Environmental Science.* **2014**, 7, 2518.

[32]   G. Xing, N. Mathews, S. S. Lim, N. Yantara, X. Liu, D. Sabba, M. Gratzel, S. Mhaisalkar, T. C. Sum, *Nature Materials.* **2014**, 13, 476.

[33]   a) C. Wehrenfennig, G. E. Eperon, M. B. Johnston, H. J. Snaith, L. M. Herz, *Advanced Materials.* **2014**, 26, 1584; b) M. B. Johnston, L. M. Herz, *Accounts of Chemical Research.* **2016**, 49, 146; c) M. Saba, M. Cadelano, D. Marongiu, F. Chen, V. Sarritzu, N. Sestu, C. Figus, M. Aresti, R. Piras, A. G. Lehmann, C. Cannas, A. Musinu, F. Quochi, A. Mura, G. Bongiovanni, *Nature Communications.* **2014**, 5, 5049; d) Y. Yamada, T. Nakamura, M. Endo, A. Wakamiya, Y. Kanemitsu, *Journal of the American Chemical Society.* **2014**, 136, 11610.

[34]   a) Y. Wang, H. Y. Wang, M. Yu, L. M. Fu, Y. Qin, J. P. Zhang, X. C. Ai, *Physical Chemistry Chemical Physics.* **2015**, 17, 29501; b) D. Meggiolaro, S. G. Motti, E. Mosconi, A. J. Barker, J. Ball, C. Andrea Riccardo Perini, F. Deschler, A. Petrozza, F. De Angelis, *Energy & Environmental Science.* **2018**, 11, 702.

[35]   A. R. Srimath Kandada, S. Neutzner, V. D'Innocenzo, F. Tassone, M. Gandini, Q. A. Akkerman, M. Prato, L. Manna, A. Petrozza, G. Lanzani, *Journal of the American Chemical Society.* **2016**, 138, 41.

[36]   a) M. Cadelano, M. Saba, N. Sestu, V. Sarritzu, D. Marongiu, F. Chen, R. Piras, F. Quochi, A. Mura, G. Bongiovanni, *Photoexcitations and Emission Processes in Organometal Trihalide Perovskites*, IntechOpen, **2016**; b) M. Cadelano, V. Sarritzu, N. Sestu, D. Marongiu, F. Chen, R. Piras, R. Corpino, C. M. Carbonaro, F. Quochi, M. Saba, A. Mura, G. Bongiovanni, *Advanced Optical Materials.* **2015**, 3, 1557.

[37]   W.-J. Yin, T. Shi, Y. Yan, *The Journal of Physical Chemistry C.* **2015**, 119, 5253.

[38]   Z. Xiao, Y. Yan, *Advanced Energy Materials.* **2017**, 7.

[39]   a) D. W. de Quilettes, S. M. Vorpahl, S. D. Stranks, H. Nagaoka, G. E. Eperon, M. E. Ziffer, H. J. Snaith, D. S. Ginger, *Science.* **2015**, 348, 683; b) L. C. Chen, J. C. Chen, C. C. Chen, C. G. Wu, *Nanoscale Research Letters.* **2015**, 10, 1020; c) L.-C. Chen, Z.-L. Tseng, C.-C. Chen, S. H. Chang, C.-H. Ho, *Applied Physics Express.* **2016**, 9; d) L. Wagner, L. E. Mundt, G. Mathiazhagan, M. Mundus, M. C. Schubert, S. Mastroianni, U. Wurfel, A. Hinsch, S. W. Glunz, *Scientific Reports.* **2017**, 7, 14899; e) S. Shao, J. Liu, G. Portale, H.-H. Fang, G. R. Blake, G. H. ten Brink, L. J. A. Koster, M. A. Loi, *Advanced Energy Materials.* **2018**, 8; f) M. Abdi-Jalebi, Z. Andaji-Garmaroudi, S. Cacovich, C. Stavrakas, B. Philippe, J. M. Richter, M. Alsari, E. P. Booker, E. M. Hutter, A. J. Pearson, S. Lilliu, T. J. Savenije, H. Rensmo, G. Divitini, C. Ducati, R. H. Friend, S. D. Stranks, *Nature.* **2018**, 555, 497; g) S. V. Makarov, V. Milichko, E. V. Ushakova, M. Omelyanovich, A. Cerdan Pasaran, R. Haroldson, B. Balachandran, H. Wang, W. Hu, Y. S. Kivshar, A. A. Zakhidov, *ACS Photonics.* **2017**, 4, 728; e) Nurul Ain Manshor, Qamar Wali, Ka Kan Wong, Saifful Kamaluddin Muzakir, Azhar Fakharuddin, Lukas Schmidt-Mende, Rajan Jose, *Phys. Chem. Chem. Phys.*, **2016**,**18**, 21629-21639; f) Kewei Wu, Ashok Bera, Chun Ma, Yuanmin Du, Yang Yang, Liang Li, Tom Wu, Phys. Chem. Chem. Phys. **2014**,**16**, 22476-22481.

[40]   a) G. J. Hedley, A. J. Ward, A. Alekseev, C. T. Howells, E. R. Martins, L. A. Serrano, G. Cooke, A. Ruseckas, I. D. Samuel, *Nature Communications.* **2013**, 4, 2867; b) A. J. Ward, A. Ruseckas, M. M. Kareem, B. Ebenhoch, L. A. Serrano, M. Al-Eid, B. Fitzpatrick, V. M. Rotello, G. Cooke, I. D. Samuel, *Advanced Materials.* **2015**, 27, 2496; c) K. H. Lee, P. E. Schwenn, A. R. Smith, H. Cavaye, P. E. Shaw, M. James, K. B. Krueger, I. R. Gentle, P. Meredith, P. L. Burn, *Advanced Materials.* **2011**, 23, 766; d) J. Kim, I. Heo, D. Park, S. J. Ahn, S.-Y. Jang, S. Yim, *J Mater Chem A.* **2014**, 2, 10250.

[41]   Y. Yang, M. Yang, K. Zhu, J. C. Johnson, J. J. Berry, J. van de Lagemaat, M. C. Beard, *Nature Communications.* **2016**, 7, 12613.

[42]   a) Y. Yang, D. P. Ostrowski, R. M. France, K. Zhu, J. van de Lagemaat, J. M. Luther, M. C. Beard, *Nature Photonics.* **2015**, 10, 53; b) N. Sestu, M. Cadelano, V. Sarritzu, F. Chen, D. Marongiu, R. Piras, M. Mainas, F. Quochi, M. Saba, A. Mura, G. Bongiovanni, *Journal of Physical Chemistry Letters.* **2015**, 6, 4566; c) R. J. Elliott, *Physical review.* **1957**, 108, 1384.

[43]   a) C. Wehrenfennig, M. Liu, H. J. Snaith, M. B. Johnston, L. M. Herz, *Journal of Physical Chemistry Letters.* **2014**, 5, 1300; b) J. L. Knutson, J. D. Martin, D. B. Mitzi, *Inorganic Chemistry.* **2005**, 44, 4699.

[44]   a) J. S. Manser, P. V. Kamat, *Nature Photonics.* **2014**, 8, 737; b) K. G. Stamplecoskie, J. S. Manser, P. V. Kamat, *Energy & Environmental Science.* **2015**, 8, 208.

[45]   a) Y. H. Kim, H. Cho, T. W. Lee, *Proceedings of the National Academy of Sciences of the United States of America.* **2016**, 113, 11694; b) Y. Tian, C. Zhou, M. Worku, X. Wang, Y. Ling, H. Gao, Y. Zhou, Y. Miao, J. Guan, B. Ma, *Advanced Materials.* **2018**, 30, e1707093; c) H. Lin, C. Zhou, Y. Tian, T. Siegrist, B. Ma, *ACS Energy Letters.* **2017**, 3, 54.

[46]   H. Hu, F. Meier, D. Zhao, Y. Abe, Y. Gao, B. Chen, T. Salim, E. E. M. Chia, X. Qiao, C. Deibel, Y. M. Lam, *Advanced Materials.* **2018**, 30, 2.

[47]   S. Draguta, S. Thakur, Y. V. Morozov, Y. Wang, J. S. Manser, P. V. Kamat, M. Kuno, *Journal of Physical Chemistry Letters.* **2016**, 7, 715.

[48]   X. Wen, Y. Feng, S. Huang, F. Huang, Y.-B. Cheng, M. Green, A. Ho-Baillie, *Journal of Materials Chemistry C.* **2016**, 4, 793.

[49]   a) R. Sheng, X. Wen, S. Huang, X. Hao, S. Chen, Y. Jiang, X. Deng, M. A. Green, A. W. Ho-Baillie, *Nanoscale.* **2016**, 8, 1926; b) F. Vietmeyer, P. A. Frantsuzov, B. Janko, M. Kuno, *Physical Review B.* **2011**, 83.

[50]   M. B. Price, J. Butkus, T. C. Jellicoe, A. Sadhanala, A. Briane, J. E. Halpert, K. Broch, J. M. Hodgkiss, R. H. Friend, F. Deschler, *Nat Commun.* **2015**, 6, 8420.

[51]   a) J. M. Richter, M. Abdi-Jalebi, A. Sadhanala, M. Tabachnyk, J. P. Rivett, L. M. Pazos-Outon, K. C. Godel, M. Price, F. Deschler, R. H. Friend, *Nature Communications.* **2016**, 7, 13941; b) T. Leijtens, G. E. Eperon, A. J. Barker, G. Grancini, W. Zhang, J. M. Ball, A. R. S. Kandada, H. J. Snaith, A. Petrozza, *Energy & Environmental Science.* **2016**, 9, 3472.

[52]   Z. Song, S. C. Watthage, A. B. Phillips, M. J. Heben, *J Photon Energy.* **2016**, 6, 022001.

[53]   W. Chen, Y. Wu, J. Liu, C. Qin, X. Yang, A. Islam, Y.-B. Cheng, L. Han, *Energy & Environmental Science.* **2015**, 8, 629.

[54]   K. C. Wang, J. Y. Jeng, P. S. Shen, Y. C. Chang, E. W. Diau, C. H. Tsai, T. Y. Chao, H. C. Hsu, P. Y. Lin, P. Chen, T. F. Guo, T. C. Wen, *Scientific Reports.* **2014**, 4, 4756.

[55]   a) S.-H. Turren-Cruz, M. Saliba, M. T. Mayer, H. Juárez-Santiesteban, X. Mathew, L. Nienhaus, W. Tress, M. P. Erodici, M.-J. Sher, M. G. Bawendi, M. Grätzel, A. Abate, A. Hagfeldt, J.-P. Correa-Baena, *Energy & Environmental Science.* **2018**, 11, 78; b) D. A. Jacobs, Y. Wu, H. Shen, C. Barugkin, F. J. Beck, T. P. White, K. Weber, K. R. Catchpole, *Physical Chemistry Chemical Physics.* **2017**, 19, 3094; c) N. Tessler, Y. Vaynzof, *ACS Applied Energy Materials.* **2018**, 1, 676.

[56]   J. Shi, Y. Li, Y. Li, D. Li, Y. Luo, H. Wu, Q. Meng, *Joule.* **2018**, 2, 879.

[57]   C. S. Ponseca, Jr., T. J. Savenije, M. Abdellah, K. Zheng, A. Yartsev, T. Pascher, T. Harlang, P. Chabera, T. Pullerits, A. Stepanov, J. P. Wolf, V. Sundstrom, *Journal of the American Chemical Society.* **2014**, 136, 5189.

[58]   a) G. Xing, N. Mathews, S. Sun, S. S. Lim, Y. M. Lam, M. Gratzel, S. Mhaisalkar, T. C. Sum, *Science.* **2013**, 342, 344; b) J. Shi, D. Li, Y. Luo, H. Wu, Q. Meng, *Review of Scientific Instruments.* **2016**, 87, 123107; c) Z. Xiao, Q. Dong, C. Bi, Y. Shao, Y. Yuan, J. Huang, *Advanced Materials.* **2014**, 26, 6503.

[59]   a) T. C. Sum, N. Mathews, G. Xing, S. S. Lim, W. K. Chong, D. Giovanni, H. A. Dewi, *Accounts of Chemical Research.* **2016**, 49, 294; b) J. C. Brauer, Y. H. Lee, M. K. Nazeeruddin, N. Banerji, *J Phys Chem Lett.* **2015**, 6, 3675; c) Q. Shen, Y. Ogomi, J. Chang, S. Tsukamoto, K. Kukihara, T. Oshima, N. Osada, K. Yoshino, K. Katayama, T. Toyoda, S. Hayase, *Physical Chemistry Chemical Physics.* **2014**, 16, 19984; d) M. Saba, M. Cadelano, D. Marongiu, F. Chen, V. Sarritzu, N. Sestu, C. Figus, M. Aresti, R. Piras, A. G. Lehmann, C. Cannas, A. Musinu, F. Quochi, A. Mura, G. Bongiovanni, *Nat Commun.* **2014**, 5, 5049.

[60]   a) T. Jiang, W. Fu, *Rsc Adv.* **2018**, 8, 5897; b) E. Bi, H. Chen, F. Xie, Y. Wu, W. Chen, Y. Su, A. Islam, M. Gratzel, X. Yang, L. Han, *Nature Communications.* **2017**, 8, 15330; c) J. C. Yu, J. A. Hong, E. D. Jung, D. B. Kim, S. M. Baek, S. Lee, S. Cho, S. S. Park, K. J. Choi, M. H. Song, *Scientific Reports.* **2018**, 8, 1070; d) C. Li, F. Wang, J. Xu, J. Yao, B. Zhang, C. Zhang, M. Xiao, S. Dai, Y. Li, Z. Tan, *Nanoscale.* **2015**, 7, 9771; e) W. Zhang, Y. Ding, Y. Jiang, M. Zheng, S. Wu, X. Lu, M. Zeng, X. Gao, Q. Wang, G. Zhou, J.-m. Liu, K. Kempa, J. Gao, *Rsc Adv.* **2017**, 7, 39523; f) F. H. Isikgor, B. Li, H. Zhu, Q. Xu, J. Ouyang, *J Mater Chem A.* **2016**, 4, 12543; g) C. Li, Y. Zhong, C. A. Luna, T. Unger, K. Deichsel, A. Graser, J. Kohler, A. Kohler, R. Hildner, S. Huettner, *Molecules.* **2016**, 21; h) Y. Li, L. Meng, Y. M. Yang, G. Xu, Z. Hong, Q. Chen, J. You, G. Li, Y. Yang, Y. Li, *Nature Communications.* **2016**, 7, 10214; i) J. Cui, H. Yuan, J. Li, X. Xu, Y. Shen, H. Lin, M. Wang, *Science and Technology of Advanced Materials.* **2015**, 16, 036004; j) T. C. Sum, S. Chen, G. Xing, X. Liu, B. Wu, *Nanotechnology.* **2015**, 26, 342001.

Chapter 2. Experimental techniques

Contents

2.1. Abstract

In this chapter, the materials used and the preparation of samples are described. Also, the main spectroscopy equipment and techniques used in this thesis are indicated.
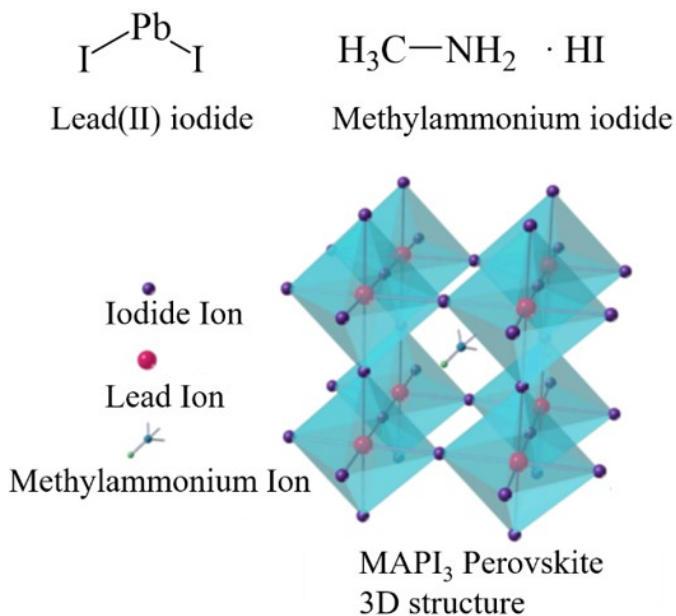
2.2. Materials used in this thesis

Figure 2.1 MAPI₃ perovskite structure and chemical structure of materials used for perovskite precursor solution.

All the studies in this thesis were carried out with MAPI$_3$ perovskite as the light absorbing material. MAPI$_3$ perovskite is suitable as a model material for basic perovskite studies and has been widely used for perovskite solar cell applications. It has a relatively simple perovskite structure.[1] Methyl-ammonium iodide (MAI) (Dyesol, PN101000) and PbI$_2$ (Sigma Aldrich, 99%) were used for MAPI$_3$ precursor solution preparation (see Figure 2.1). All the other semiconductor materials used are shown in Figure 2.2. PEDOT:PSS and PTAA were acquired from Heraeus (Clevios P VP Al4083) and Ossila respectively and were used as hole transfer materials, while PC$_{61}$BM from Nano C and Poly{[N,N'-bis(2-octyldodecyl)naphthalene-1,4,5,8-bis(dicarboximide)-2,6-diyl]alt-5,5'-(2,2'-bithiophene)} (N2200) from One Material were utilized as the electron transport layers for chapter 4 and 5. In chapter 5, PDPP2T-based polymers DT-PDPP2T-TT acquired from One Material was used as an organic donor material.
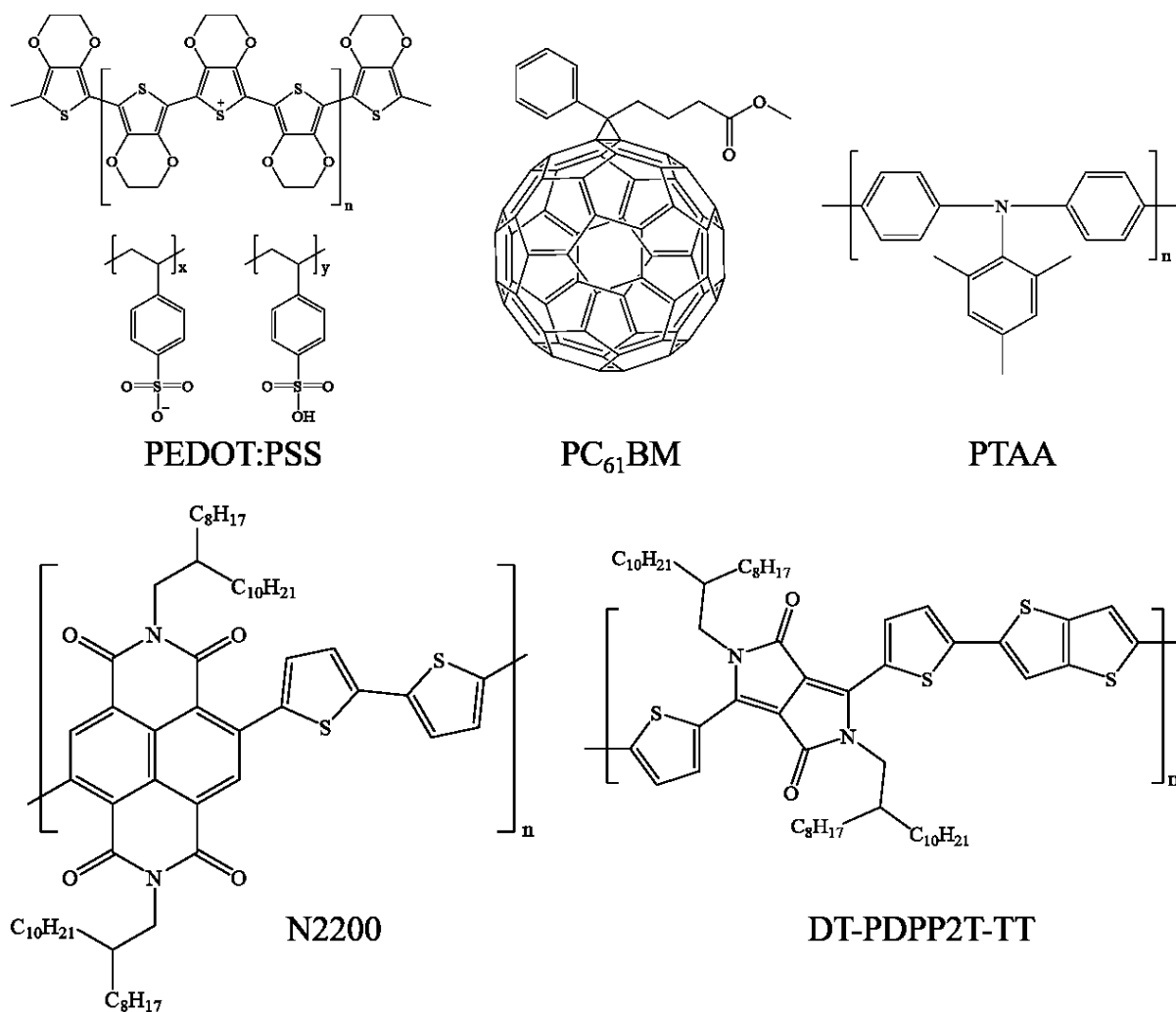
Figure 2.2 Chemical structures of PEDOT:PSS, PC₆₁BM, PTAA, N2200, and DT-PDPP2T-TT

2.3. Sample preparation.

2.3.1. Film preparation.

The specific film and device fabrication conditions will be introduced in each individual chapter. Thin films were required for the characterization of the materials, thus the solutions were prepared and deposited on glass (VWR chemicals) or ITO glass (Psiotech and Amgtech for chapter 3 and 4, and chapter 5, respectively) substrates. The substrates were well cleaned using a sonication bath with DI water with 5% of detergent (Decon90), followed by rinsing

with DI water, ethanol, acetone, and isopropanol for 10 mins each, then dried with nitrogen and in a 120 °C drying oven. After this the substrates were further treated with an oxygen plasma for 10 mins prior to depositing the solutions. A spin coater (Laurell Technologies Corporation, WS-650-23) was usually used to prepare films. All the samples except PEDOT:PSS film were spincoated in an N_2 filled glove box (Mbraun, O_2 and H_2O level below 0.5 ppm respectively). All the solutions were filtered with a 0.2 μm PTFE membrane and dehydrated with magnesium sulphate (VWR chemicals) before use. To maximise the stability of the fabricated perovskite films and prevent the degradation of samples by air and eliminate the oxygen effect on charge carrier mobility behaviour, films were encapsulated by using a glass coverslip and Surlyn (Solaronix, Swiss) in a nitrogen filled glove box at 80 °C and then we further sealed the edges with epoxy to minimise potential oxygen diffusion while measuring and storing samples before spectroscopic measurements in chapters 3 and 4. The seal was made by heating the gasket around the cell with the tip of a soldering iron. Additionally, for chapter 3, the $MAPI_3$ samples were stored for 12 days in a nitrogen-filled glove box at room temperature and kept in the dark after encapsulation to collect more reliable spectroscopic data. The samples storage effect will be described in chapter 4.

2.3.2. Device preparation.

For chapter 3, ITO/PEDOT:PSS/$MAPI_3$/$PC_{61}BM$/LiF/Ag devices were fabricated. The top cathode deposition of lithium floride (LiF) and aluminium (Al) to complete the device was undertaken to enable JV characterization, including the light intensity dependence of current density by Du Tian (imperial College London). A 10 nm LiF and 100 nm Al layer was deposited through a patterned shadow mask by thermal evaporation at ~10^{-7} mbar high vacuum with a deposition rate of 0.2 nm s^{-1}. For chapter 4 and 5 ITO/PTAA/$MAPI_3$/$PC_{61}BM$/LiF/Ag

devices were characterised. The devices were fabricated and their JV characterization undertaken by Du Tian (Imperial College London) and Chieh-Ting Lin (Imperial College London) for chapter 3, 4 and chapter 5, respectively.

2.4. Experimental techniques

2.4.1. Steady-state UV-vis absorption spectroscopy

UV-visible absorption spectroscopy was undertaken in the wavelength range 300 - 1400 nm, which is the useful irradiance range of the sun for solar cell applications. Since the polymer and small molecules films are generally not very reflective, the reflectance of these films was neglected in the organic film measurements. Therefore, absorbance (A_{asb}) can be related to the logarithm of transmittance (T), as the equation (2.1) shown below:

$$A_{asb} = -\log T$$

(2.1)

In this thesis, the steady state absorption spectrum of the perovskite films was measured by using a UV-2600 Shimadzu UV-vis spectrophotometer with wavelength resolution of 0.1 nm and scan rate of 1 nm/s. An integrating sphere is attached to enable determination of the reflectance and absorbance since perovskite material has a highly reflective glassy surface.
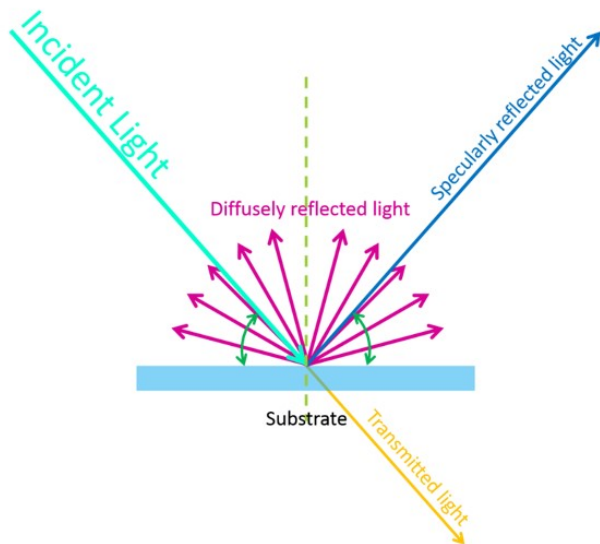
Figure 2.3 schematic drawing of diffuse and specular reflectance for thin film.

According to the law of reflection, the relative angle of incidence and reflection can be determined by plotting the surface normal rays at the point of incidence. (see Figure 2.3) Specular reflection means that when the reflective surface of the object is smooth, the light will be reflected symmetrically. When light reaches a rough surface, because the direction of the normal line of each point is different, the reflected light is randomly oriented to different directions. This type of reflection is called diffuse reflection. One of the difficulties of measuring perovskite films which have a smooth surface but are deposited on a mesoporous substrate such as a TiO_2 or NiO is that the fine particles in the medium may scatter the reflected light and affect the efficiency of light reaching the detector, which reduces the clarity of the spectrum. Therefore, the integrating sphere would be necessary for this type of measurement. The structure of the integrating sphere is shown in the figure below. The barium sulfate-coated sphere can draw the scattered light to make sure all light can be detected.
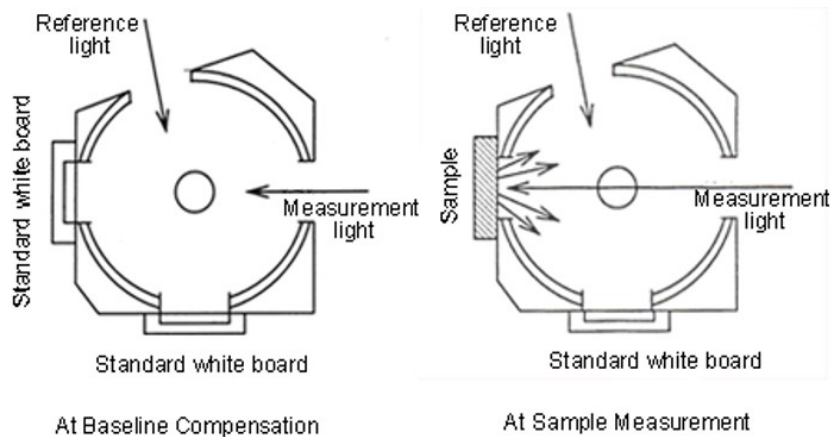
Measuring diffuse reflectance, not including Specular reflection
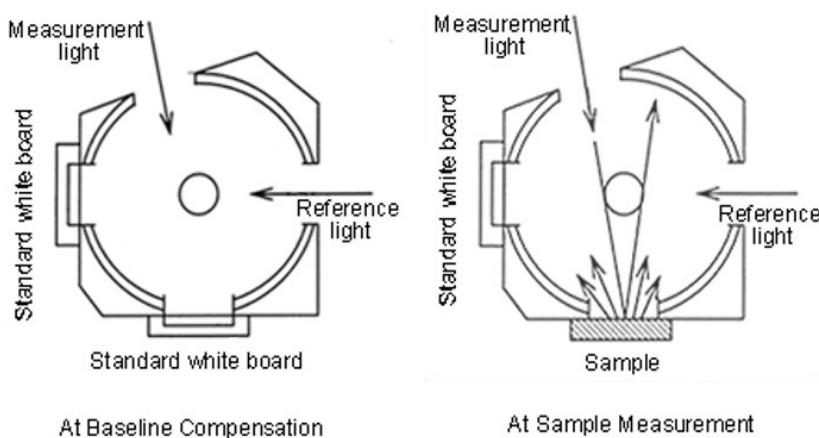
Measuring diffuse reflectance, including Specular reflection

Figure 2.4 Schematic figure of the working principle of integrating sphere measuring diffuse and specular reflectance. (Figure source; https://www.shimadzu.com/an/molecular_spectro/uv/accessory/solidsample/solid.html accessed at 08.08.2018)[2]

In Figure 2.4, the working principle of the integrating sphere is as follows: the sample is placed in front of the incident light window for measurement, and the light reflected from the sample is collected by a barium sulfate-coated sphere and then reach the detector.[2] The reflectance (relative reflectance) value was obtained using the reflectance of a standard whiteboard (which is regarded as 100%) as a reference. When light is directed at the sample at an incident angle of 0°, only diffuse reflection is detected. To measure both specular and diffuse reflection,

different incident angle needs to be used. From the measurement, absorptance (A_{ast}) of material on the substrate can be calibrated as the equation (2.2) shown below:

$$A_{ast} = 100 - T - R_{diff} - R_{spec} - Ref_{sub}$$

(2.2)

Where A_{ast} is absorptance, T is transmittance, R_{diff} is diffuse reflectance, R_{spec} is specular reflectance and Ref_{sub} is absorptance of the substrate.

2.4.2. Photoluminescence spectroscopy

2.4.2.1. Steady-state photoluminescence (ss-PL) spectroscopy

Photoluminescence spectroscopy is used to measure the intensity of fluorescence. The higher the fluorescence intensity, the stronger the emission ability of the sample. If there is an interaction between the fluorescent molecule and a quencher, the fluorescence intensity would be reduced, which is called fluorescence quenching. Photoluminescence spectroscopy can thus be used to understand the efficiency of quenching of emissive charge carriers when comparing the maximum PL of a neat material film to the PL of a bilayer or blend film. As described before, for the perovskite carrier dynamics studied herein, charge carrier transfer to the transport layer is the most important quenching process. PLQE, shown in the equation (2.3) below can assess the charge transfer yield from the surface of perovskite to the charge transport material:

$$\text{PLQE}(\%) = \frac{I_{neat} - I_{quencher}}{I_{neat}} \times 100$$

(2.3)

where I_{neat} and $I_{quencher}$ respectively refer to the photoluminescence intensities of the neat and bilayer or blend films. PLQE measurements have been widely used to characterize the exciton separation properties of organic photovoltaic devices between donor and accepter materials because this measurement is inexpensive and simple to estimate charge transfer and can also be successfully applied to other types of PV devices including emerging hybrid perovskite PV devices.[3] Steady state PL measurements were undertaken using a Fluorolog 1039 spectrometer (Horiba Scientific) at room temperature. Depending on the emission wavelength, different detectors are required. For a PL emission below to 800 nm, a visible detector was used. Once the PL emission is higher than 800 nm, it requires a liquid nitrogen-cooled infrared detector which is more sensitive. For conventional measurements, monochromatic excitation light generated from the spectrometer's internal xenon light source was used.

2.4.2.2. Steady-state 1 Sun photoluminescence
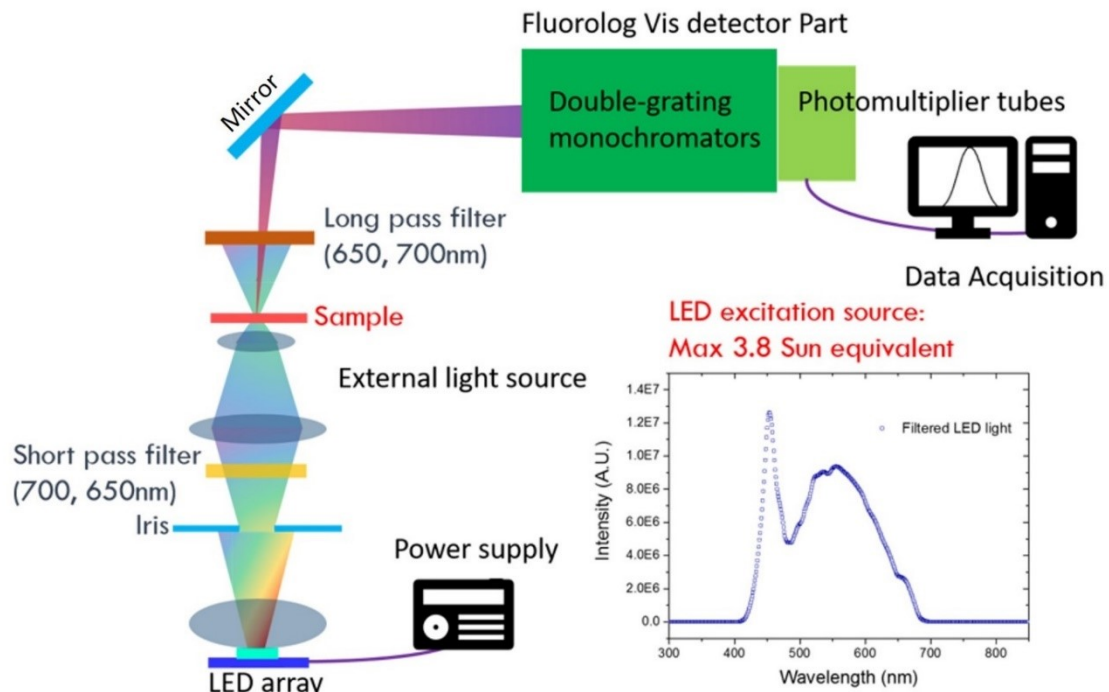
Figure 2.5 Schematic drawing of home-made steady-state 1 Sun LED PL spectrometer system and the spectrum of the filtered LED external light source. The sample was excited through the glass side.

For variable excitation density measurements, an external white light emitting diode (LED) light source (Bridgelux RS Array BXRA-40E7500-j-03) was used with 650 and 700 nm short pass filters (SPF). A DC power supply was used to manipulate the excitation fluenece of the LED from ~0.08 to 370% of 1 Sun. the fluence estimated by normalising against current densities obtained with AM 1.5 irradiation. The PL of the sample was acquired by the Fluorolog 1039 spectrometer passing through a 650 and 700 nm long pass filter (LPF) to cut off the excitation light source. In figure 2.5, the PL spectrometer, external light setup and the filtered LED irradiation spectrum is displayed.

2.4.2.3. Pulsed laser photoluminescence

Figure 2.6 Scheme of lab-made static state LASER PL spectrometer system

Pulsed photoluminescence was characterised by using an Nd:Yag Laser (Opolette, OPOTEK) with a laser pulse resolution of 20 ns (See figure 2. 6). The reputation rate of the excitation la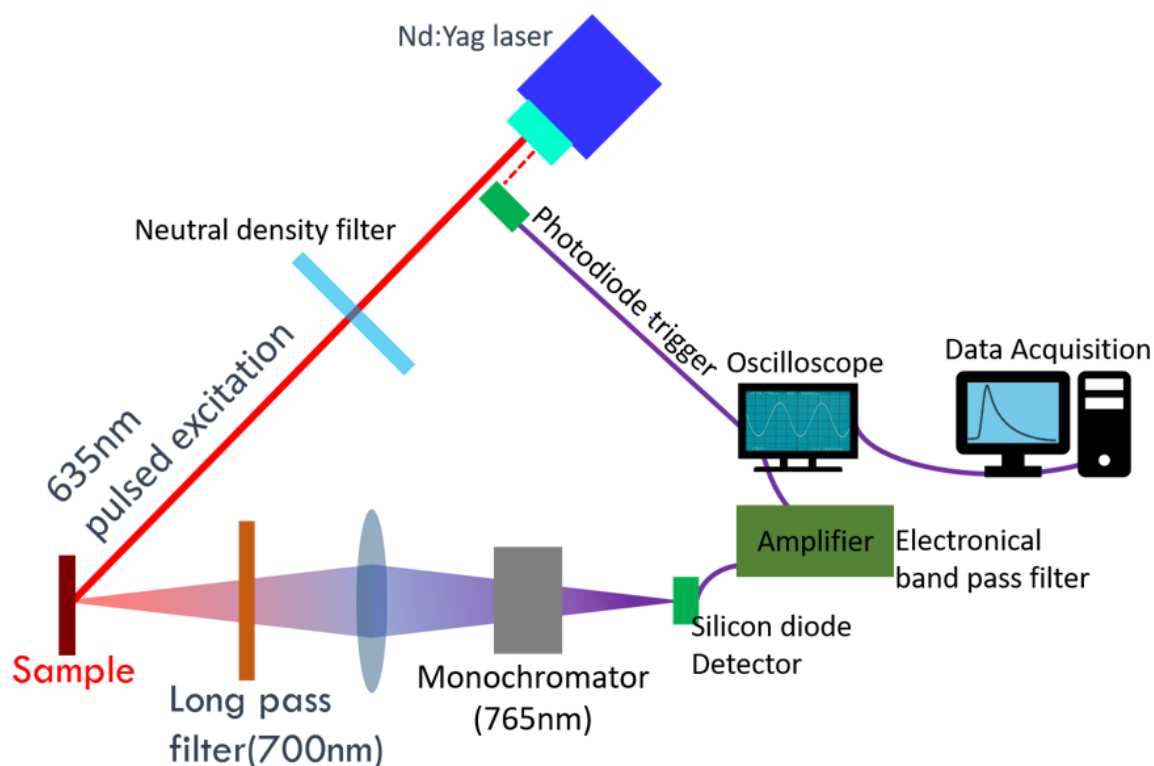ser was 20 Hz, which is relatively low to allow the analysis of more simplified PL information. For example, low reputation rate can reduce the accumulation of perovskite charge carriers which have ns - μs lifetimes. Additionally, the sensitive Si-photodiode detector (Hamamatsu Photonics, S1722-01) and high power of the laser permits samples to be excited by a wide range of excitation densities (0.1 to 380 μJ cm^{-2} pulse energies) using neutral density filters. The photodiode signal is then pre-amplified and sent to the main amplifier which is made up of an electronic band pass filter (Costronics Electronics). A digital oscilloscope (Tektronics, TDS220) collects the signals that are synchronized with the trigger signal of the pump laser pulse of the photodiode (Thorlabs Inc., DET210). The instrument response time to measure the PL transients is 100 ns.

2.4.2.4. Time-correlated singe-photon counting (TCSPC)

Since the probability of detecting a single photon at a specific time after a low intensity excitation pulse is proportional to the fluorescence intensity at that time, TCSPC is often used as to monitor the fluorescence lifetime from picoseconds to microseconds. A histogram of fluorescence photon arrival times can be established based on successive excitation-collection cycles which is a direct quantitative indicator of the decay dynamics. Compared with other time domain techniques, TCSPC has the advantages of great sensitivity, large dynamic range and high time resolution. It is does not need a strong excitation source (reducing the risk of photobleaching the sample) and also is not affected by fluctuations in the intensity of the excitation source during the measurement. TCSPC's workflow is briefly shown in the figure 2. 7 below.
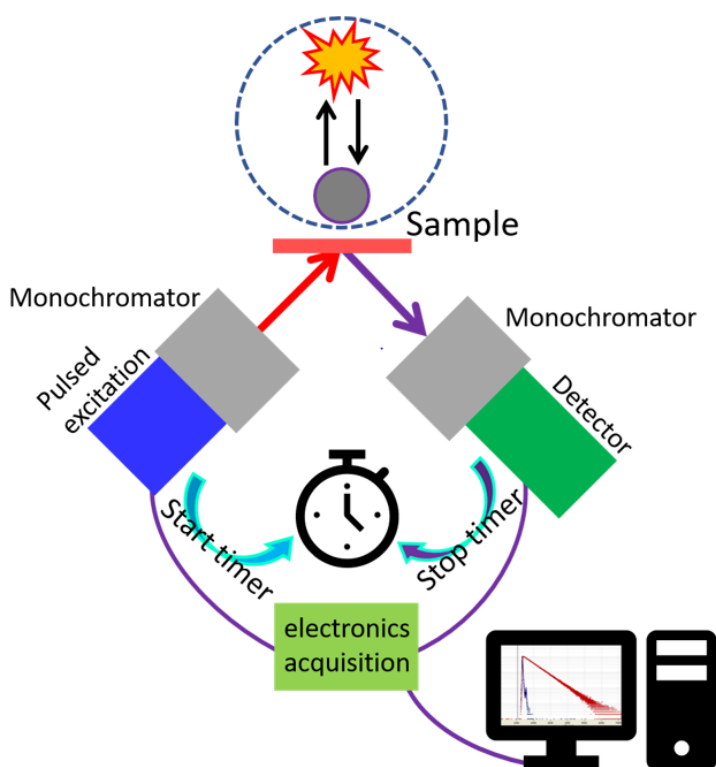
Figure 2.7 Explanation of the pulsed technique for TCSPC and the work flow schematically.

The instrumentation is mainly composed of the following four parts: light source, detector, electronics and optical components. (Figure 2.7) The excitation light source and detector have the biggest impact on the performance of the equipment, and the measurement response only depends on these two components.

In this study, aDelta Flex system (Horiba Scientific) was used for TCSPC measurements of tr-PL. The PL transient signal was collected using a single-photon counting detector (PPD-900, Horiba scientific). The excitation source was a 635 nm diode laser (NanoLED N-02B, Horiba scientific) with a < 200 ps pulse duration and a 1 MHz repetition rate. In order to modulate the excitation pulse energy, neutral density filters were used.

Figure 2.8 PL quenching (PLQ) spectra of a) stoichiometric MAPI$_3$, b) MAI excess MAPI$_3$ films with PC$_{61}$BM c) ss-PL emission spectra and d) tr-PL decay spectra probed at 765 nm of stoichiometric MAPI$_3$ (red line) and MAI excess MAPI$_3$ (blue line) films.

Figure 2.8a, 2.8b and 2.8c show the example of steady-state photoluminescence (ss-PL) analysis of neat stoichiometric MAPI$_3$ film (1:1 ratio of MAI and PbI$_2$) and 5% MAI excess ratio MAPI$_3$ perovskite film with and without PC$_{61}$BM as an electron transport layer.[4] From these PL spectrums, PL peak intensity could be collected and PLQE can be easily calculated. The PLQEs of stoichiometric and MAI excess MAPI$_3$ film are simply calibrated using the equation 2.3 as 73% and 98% of PLQE respectively, and the electron transfer properties could be compared. Figure 2.8c shows the comparison between these films. As mentioned, the higher intensity of PL indicates the relatively smaller amount of the nonradiative recombination

processes together with the lower density of trap states. Thus, it could be concluded that MAI excess MAPI$_3$ film has less non-radiative trap state than stoichiometric MAPI$_3$ film. Figure 2.8d shows tr-PL dynamics of MAPI$_3$ films probed from the peak wavelength of PL spectra as 765nm. Typically, perovskite shows biphasic decay behavior; fast few nanosecond lifetime components and following slow decay components over 100 ns are assigned as charge carrier trapping and bimolecular recombination process of the remain carriers in the bulk respectively. These two components could be fitted practically using biexponential equation ($y = A_1 \times \exp(-x/\tau_1) + A_2 \times \exp(-x/\tau_2) + y_0$) which allows to study charge carrier trapping process from the tr-PL and gives more correct free charge carrier life time of the film. From the fitting, biexponential decay times of $\tau_1=1.4$ and $\tau_2=370$ ns for stoichiometric MAPI$_3$ and $\tau_1=2.7$ and $\tau_2=735$ ns for MAI excess MAPI$_3$ could be analysed. More details of these data and analysis can be found in reference.[4]

2.4.3. Femtosecond transient absorption spectroscopy (fs-TAS)

TAS is a pump-probe time-resolved absorption spectroscopy technique which allows the determination of photo induced processes in films including interfacial charge transfer processes in single and multi-layered materials, which are key to the photovoltaic operation.[1d, 5] As an optical two pulse transient technique, fs-TAS has a high pulse temporal resolution, which enables the study of early excited states dynamics (from ~200 fs to 6 ns) and permits the monitoring of early stages of charge generation. The IRF (instrument response function) of this system is approximately 200 fs, which is based on FWHM (the full width at half maximum) of the scattering signals. An imaging spectrometer with white light probe pulse is used to collect

transient spectra as a function of time delay. The components of the fs-TAS used in this thesis are illustrated in Figure 2.9.
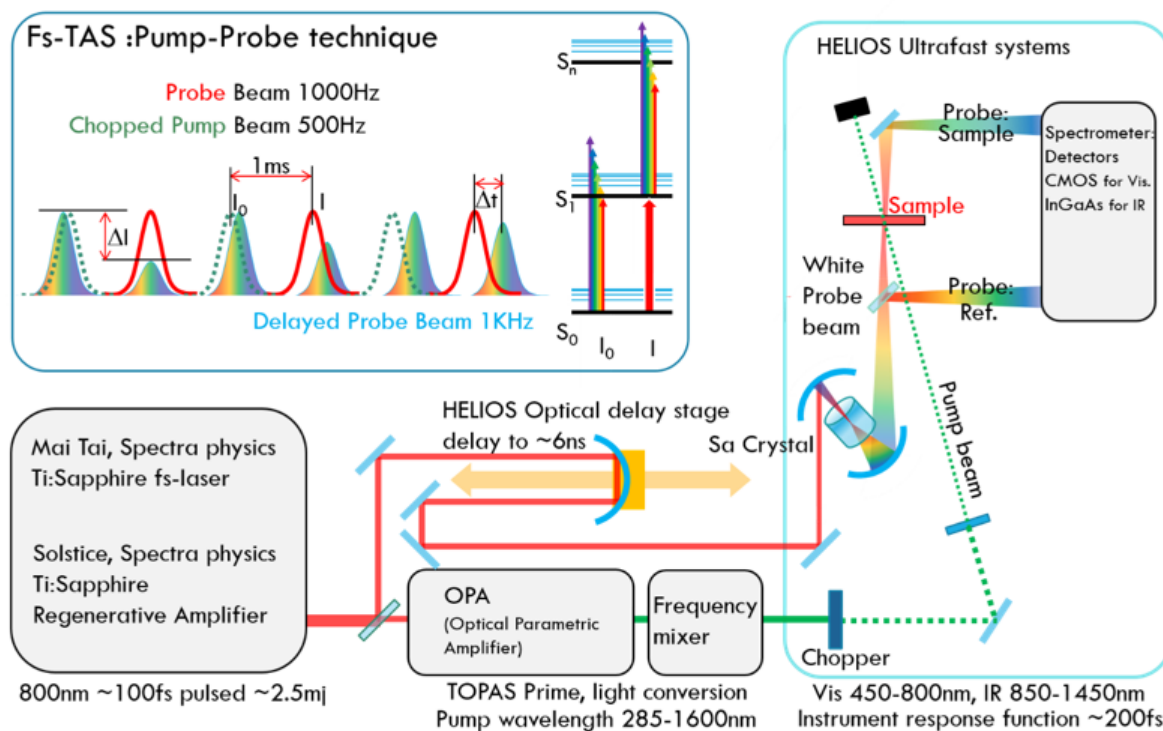
Figure 2.9 Schematic figure of the ultra-fast TAS setup used for this study and the working mechanism left top inset.

The output pulse energy of the Ti:Sapphire femtosecond optical cavity (Mai Tai, Spectra Physics) is increased by a Ti:Sapphire regenerative amplifier (Solstice, Spectra Physics) from 17.5 nJ to >2.5 mJ, while the narrow pulse duration is maintained to ~ 100 fs. A Solstice box is required to amplify the ultrashort pulses, because they may damage the Ti:Sapphire crystal in the regenerative amplifier if they are amplified directly. A Solstice box comprises three parts: a stretcher, a regenerative amplifier, and a compressor. The pulses are time-stretched before amplified, and finally re-compressed, after which the output would be an 800 nm, ~100 fs pulsed beam with a pulse energy of ~2.5 mJ. Following this amplification process, the

generation of white light can be achieved in the transient spectrometer. The output of Solstice is divided into two separate directions, the optical parametric amplification (OPA) (TOPAS prime, Light conversion) and the delay line (HELIOS) respectively. The OPA is an amplifier based on the non-linear optical parametric amplification principle to emit light with variable frequencies and polarization, after which a frequency mixer is used to extend the excitation wavelength range to UV and IR. One of the benefits of OPA is the flexibility to tune excitation pulses to a variety of possible wavelengths from 285 to 1600 nm. This thesis will mainly cover excitation wavelengths between 550 and 840 nm.

For the rest of fundamental pulses directed to the delay line, these are reflected by a spherical mirror attached to a cart with micrometre-precision movement. The movable distance on cart determines the time delay of the pulse relative to the excitation pulse. The delay line allows time delays to be extended to 6 ns. After passing the delay stage, the pulse enters the spectrometer (HELIOS, Ultrafast Systems) where the white probe beam is generated, the aligned excitation and probe pulses are aligned on the sample, and the intensity change of the probe pulse are detected and measured. In the spectrometer area, by using different crystals, white light probe beams can be generated either in the visible range (from 450 to 750 nm) with a CMOS detector or in the NIR (from 850 to 1450 nm) with an InGsAs detector. Thus, either ground state bleaching/stimulated emission signals (GSB/SE) or excited state absorption signals (ESA) can be probed since there is a wide range of wavelengths.

The detectors used here are imaging spectrometers. Compared to conventional monochromators, they can simultaneously acquire a spectrally resolved image, which can be faster at processing large amounts of data and can obtain transient spectra instead of transients as a function of time. As shown in Figure 2.9 left top inset, the intensity difference is measured

by chopping the pump pulse. When detecting the probe, the repetition rate of the pump is reduced from 1 kHz to 500 Hz by a chopper. Therefore, the detection pulse frequency-aligned with the pump pulse will be partially absorbed by the excited state while the pulse with no pump will only be absorbed from the ground state.

2.4.3.1. Example of fs-TAS data and analysis
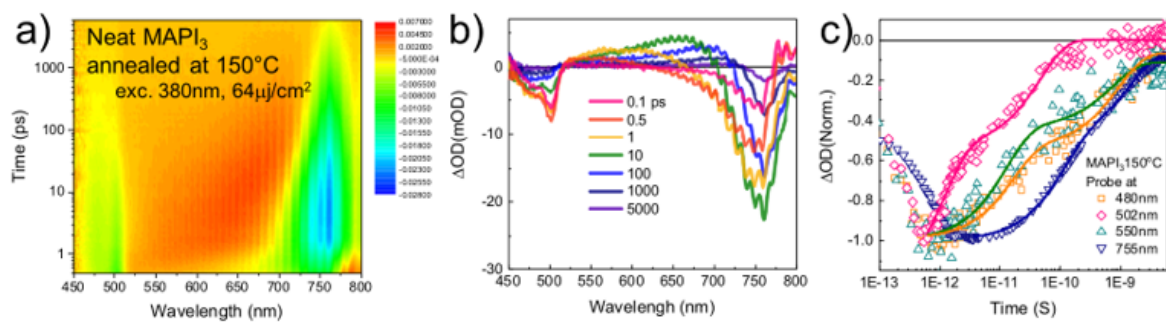
Figure 2.10 a) 2D fs-TAS and b) TA spectra of MAPI$_3$ post annealed at 150 °C with excitation at 380 nm (flux 64 μj/cm^2) c) TA dynamics of the 150ºC annealed MAPI$_3$ films probed at 480 nm (PB1), 502 nm, 550 nm (PIA),and 755 nm (PB2).

Figure 2.10a shows an example of a 2D fs-TAS visible spectrum of MAPI$_3$ perovskite film which PbI$_2$ species introduced by 150 °C post thermal annealing process.[6] Since a charge coupled device (CCD) detector is used to collect the signal in the TAS system, TA signal from an wide range of wavelengths from 450 to 800 nm could be collected each delay time. Thus, typical time, wavelength, and ΔOD data could be collected together and displayed into the 2D spectra. Also, TA spectra in figure 2.10b, and dynamics in Figure 2.10c could be plotted from the data.

From the TA spectra shown in figure 2.10b of MAPI$_3$ perovskite, two typical negative photo bleaching (PB) signals could be observed at around 480 nm (PB1) and 755 nm (PB2). These

typical double bleaching signals of MAPI$_3$ perovskite could be observed when the film thickness is less than around 100nm. For thicker perovskite films (thicknesses over around 300 nm, as used for optimized solar cell devices) have a strong ground state absorbance (over 1) below 550 nm, reducing the signal to noise of this feature. The positive signal in the range of approximately 550 to 650 nm is photoinduced transient absorption (PIA). For film and device characterization, PB2 which comprises of ground state bleaching (GSB) and stimulated emission (SE) near the material bandgap is widely used to study the free charge carrier dynamics of MAPI$_3$ perovskite, and is the most studied spectral feature in this thesis.

The TA dynamics in figure 2.10c collected in a time scale from ±1 ps to 6 ns from the data in figure 2.10a can be analysed to indicate the free charge carrier dynamics for each species. The PB2 at 755 nm shows the information of the excited charge carrier cooling or trapping process, free charge bimolecular recombination, and charge carrier transfer to ETL and HTL.

Analyses of such data can identify the formation of species. For example, in the data shown in Figure 2.10, collected for films deposited with excess Pb^{2+}, charge carrier transfer to PbI$_2$ can be observed at 502 nm wavelength, overlapped with PB1 signal, 1 in figure 2.10b. In figure 2.10c, the time constant of this transfer to PbI$_2$, monitored at 502 nm (2.4 eV) was determined to be around 5 ps from exponential fitting using Origin (OriginLab Corporation). More details of these data and analysis can be found in reference.[6]

2.4.4. X-Ray diffraction (XRD)

Thin film structure can be determined by X-ray crystallography. The X-ray beam incident on the crystalline atoms can be diffracted into many specific directions. Crystal structure, chemical

bonds and the crystallographic disorder can be determined from the mean diffraction pattern. X-rays are considered as electromagnetic radiation waves.[7] Thus, the perovskite structure and phase of the plane were conducted via XRD using a PANalytical X'Pert system (Cu Ka, l=1.54 Å) at 40 kV and 40mA. The diffraction patterns were obtained over the 2θ range between 10° to 50° in steps of 0.04° and subsequently analysed using Highscore software.
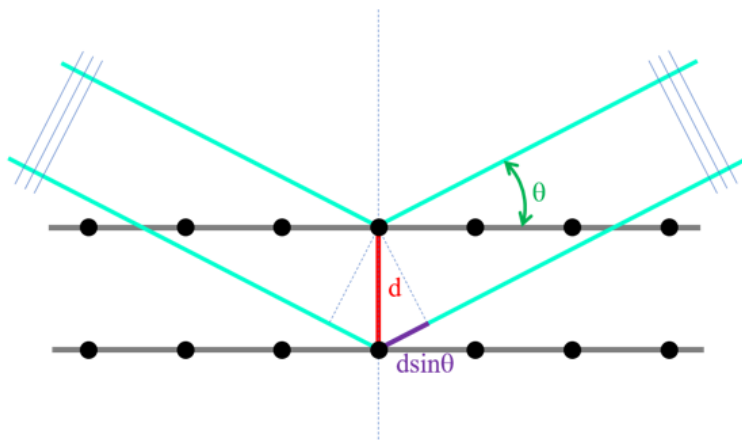
Figure 2.11 Schematic drawing of Bragg's Law in an X-ray diffraction.

The repetitive arrangement of atoms within the crystal from the diffraction pattern is determined by Bragg's law shown below.

$$2d \sin \theta = n\lambda$$

(2.5)

where d is the spacing between diffracting planes, θ is the incident angle, n is any integer, and λ is the wavelength of the beam. (See Figure 2.9) The diffraction pattern is normally collected by X-rays since their wavelength is naturally the same order of magnitude as the spacing d of each plane in the crystal.

2.4.5 Current-Voltage characteristics

Photovoltaic device performance is commonly characterized using current-voltage characteristics called J–V curves in order to determine their efficiency.[8] The power conversion efficiency (PCE) is shown in the equation (2.7)

$$PCE = \frac{J_{SC} \times V_{OC} \times FF}{P_I}$$

(2.7)

where J_{SC} is short circuit current density, V_{OC} is open circuit voltage, FF is fill factor and P_I the incident light intensity. FF represents the ideality of the performance of solar cells affected by various recombination losses and is, therefore, <1 shown in the following below:

$$FF = \frac{V_{Max} \times J_{Max}}{V_{OC} \times J_{SC}}$$

(2.8)

where FF is the ratio of the maximum power output, which is the result of multiplying V_{Max} (voltage maximum) and J_{Max} (current density maximum), to the product of J_{SC} and V_{OC}. (See Figure 2.10)
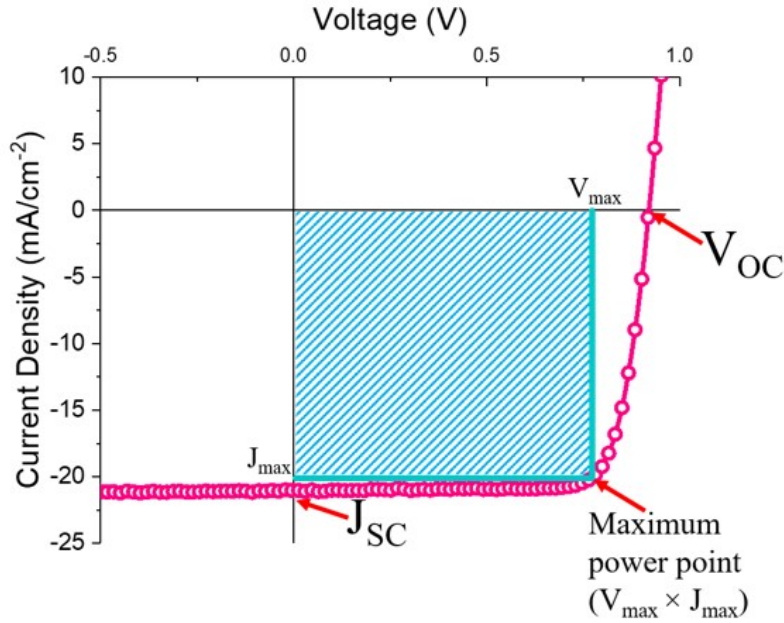
Figure 2.12 Current-Voltage characteristic curves under illumination at 1 Sun conditions.

 J-V curves were measured under A.M 1.5 1 Sun equivalent simulated illumination of 100 mW cm^{-2} provided by a filtered Xenon lamp solar simulator (Oriel Instruments). The light intensity was calibrated with a silicon reference cell. The device was secured in an N_2 gas filled chamber which has a quartz glass window on top allowing solar irradiation passing through to the device. A source meter (Keithley 2400) was used to apply voltage and record the current. The scan rate was set at 125 mV/s. The device active area size was 0.045cm^{-2} (0.3 × 0.15 cm^{-2}). From the J–V curves, device parameters such as open circuit voltage (V_{OC}), short circuit current (Jsc), fill factor (FF) and power conversion efficiency (PCE) were collected.

2.5. References

[1]   a) Y. S. Kwon, J. Lim, I. Song, I. Y. Song, W. S. Shin, S.-J. Moon, T. Park, *J Mater Chem.* **2012**, 22, 8641-8648; b) U. Bach, D. Lupo, P. Comte, J. E. Moser, F. Weissortel, J. Salbeck, H. Spreitzer, M. Gratzel, *Nature.* **1998**, 395, 583-585; c) N. Cai, S. J. Moon, L. Cevey-Ha, T. Moehl, R. Humphry-Baker, P. Wang, S. M. Zakeeruddin, M. Gratzel, *Nano Lett.* **2011**, 11, 1452-1456; d) H. S. Kim, C. R. Lee, J. H. Im, K. B. Lee, T. Moehl, A. Marchioro, S. J. Moon, R. Humphry-Baker, J. H. Yum, J. E. Moser, M. Gratzel, N. G. Park, *Sci Rep.* **2012**, 2, 591; e) D. Liu, T. L. Kelly, *Nature Photonics.* **2013**, 8, 133-138; f) C. C. Stoumpos, C. D. Malliakas, M. G. Kanatzidis, *Inorganic Chemistry.* **2013**, 52, 9019-9038; g) M. Liu, M. B. Johnston, H. J. Snaith, *Nature.* **2013**, 501, 395-398.

[2]   Diffuse   Reflectance   Measurement, https://www.shimadzu.com/an/molecular_spectro/uv/accessory/solidsample/solid.html, accessed: 0808, 2018.

[3]   a) D. W. deQuilettes, W. Zhang, V. M. Burlakov, D. J. Graham, T. Leijtens, A. Osherov, V. Bulovic, H. J. Snaith, D. S. Ginger, S. D. Stranks, *Nature Communications.* **2016**, 7, 11683; b) X. F. Deng, X. M. Wen, J. H. Zheng, T. Young, C. F. J. Lau, J. Kim, M. Green, S. J. Huang, A. Ho-Baillie, *Nano Energy.* **2018**, 46, 356-364; c) X. Feng, H. Su, Y. Wu, H. Wu, J. Xie, X. Liu, J. Fan, J. Dai, Z. He, *J Mater Chem A.* **2017**, 5, 12048-12053; d) D. W. deQuilettes, S. M. Vorpahl, S. D. Stranks, H. Nagaoka, G. E. Eperon, M. E. Ziffer, H. J. Snaith, D. S. Ginger, *Science.* **2015**, 348, 683-686; e) L. Zuo, H. Guo, D. W. deQuilettes, S. Jariwala, N. De Marco, S. Dong, R. DeBlock, D. S. Ginger, B. Dunn, M. Wang, Y. Yang, *Science Advances.* **2017**, 3, e1700106; f) T. Li, Y. Pan, Z. Wang, Y. Xia, Y. Chen, W. Huang, *J Mater Chem A.* **2017**, 5, 12602-12652; g) A. R. Pascoe, S. Meyer, W. Huang, W. Li, I. Benesperi, N. W. Duffy, L. Spiccia, U. Bach, Y.-B. Cheng, *Advanced Functional Materials.* **2016**, 26, 1278-1285; h) D. S. Ginger, N. C. Greenham, *Phys Rev B.* **1999**, 59, 10622-10629; i) K. Cnops, B. P. Rand, D. Cheyns, B. Verreet, M. A. Empl, P. Heremans, *Nat Commun.* **2014**, 5, 3406; j) D. M. Stoltzfus, J. E. Donaghey, A. Armin, P. E. Shaw, P. L. Burn, P. Meredith, *Chemical Reviews.* **2016**, 116, 12920-12955; k) J. R. Zhang, D. L. Bai, Z. W. Jin, H. Bian, K. Wang, J. Sun, Q. Wang, S. Z. Liu, *Advanced Energy Materials.* **2018**, 8, 1703246.

[4]   T. Du, J. Kim, J. Ngiam, S. Xu, P. R. F. Barnes, J. R. Durrant, M. A. McLachlan, *Advanced Functional Materials.* **2018**, 28.

[5]   a) V. sharma, S. Aharon, I. Gdor, C. Yang, L. Etgar, S. Ruhman, *J Mater Chem A.* **2016**, 4, 3546-3553; b) J. M. Marin-Beloqui, J. P. Hernandez, E. Palomares, *Chemical Communications.* **2014**, 50, 14566-14569; c) A. Marchioro, J. Teuscher, D. Friedrich, M. Kunst, R. van de Krol, T. Moehl, M. Grätzel, J.-E. Moser, *Nature Photonics.* **2014**, 8, 250-255.

[6]   T. Du, C. H. Burgess, J. Kim, J. Zhang, J. R. Durrant, M. A. McLachlan, *Sustain Energ Fuels.* **2017**, 1, 119-126.

[7]   D. E. F. WE, *A Textbook of Mineralogy*, New York: John Wiley & Sons., **1932**.

[8]   H. J. van der Bijl, *Proceedings of the IRE.* **1919**, 7, 97-128.

Chapter 3. Excitation density dependent photoluminescence quenching and charge transfer efficiencies in hybrid perovskite / organic semiconductor bilayers

Contents

3.1. Abstract

This study addresses the effect of excitation intensity on the charge transfer efficiency between bilayers of $MAPI_3$ with $PC_{61}BM$ or PEDOT:PSS. Analysis of the kinetic competition between interfacial electron / hole transfer and charge trapping and recombination within $MAPI_3$ is studied by employing a range of optical measurements including steady-state PLQ and tr-PL and absorption over a broad range of excitation densities. Our results indicate that PLQ measurements with a typical PL spectrometer can yield significantly different transfer efficiencies to those measured under 1 Sun irradiation. Steady-state and pulsed measurements indicate low transfer efficiencies at low excitation conditions ($< 5 \times 10^{15}$ cm^{-3}) due to rapid charge trapping and low transfer efficiencies at high excitation conditions ($> 5 \times 10^{17}$ cm^{-3}) due to fast bimolecular recombination. Efficient transfer to $PC_{61}BM$ or PEDOT:PSS is only observed under intermediate excitation conditions (~ 1 Sun irradiation) where electron and hole transfer times are determined to be 36 and 11 ns, respectively. The results are discussed in terms of their relevance to the excitation density dependence of device photocurrent generation, impact of charge trapping on this dependence and appropriate methodologies to determine charge transfer efficiencies relevant to device performance.

3.2. Introduction

As discussed in chapter 1, $MAPI_3$ perovskite materials exhibit a range of favourable optoelectronic properties for photovoltaic device function, including large absorption coefficients for light absorption and high charge carrier mobilities to enable rapid charge transfer from the photoactive layer.[1] A key consideration determining the efficiency of such devices is the kinetic competition between the extraction of photogenerated charges from the photoactive perovskite layer to the external circuit versus charge recombination and trapping processes within this layer and at its interfaces. This kinetic competition, which determines transfer efficiency, is strongly dependent on film processing and device architecture, and also dependent on light irradiation intensity and device operating condition (e.g.: short circuit versus maximum power point). In particular, whilst several studies have reported a strong, and complex, dependence of charge carrier recombination and trapping processes upon light intensity in $MAPI_3$ films,[2] studies of the impact of this light intensity dependence upon the kinetics and efficiency of charge transfer from the $MAPI_3$ layer to electron and hole transport layers have been limited to date.[3] This dependence is not only important to understand the irradiation intensity dependence of device efficiency, but also critical in determining the relevance of steady-state and pulsed assays of these transfer processes to device operation. Such assays are often undertaken under irradiation conditions very different from steady-state solar irradiation, a consideration which has received little attention to date in studies of the impact of these charge transfer processes upon device performance. In the study herein, therefore the light intensity dependence of these charge transfer processes will be investigated employing a range of both steady-state and transient optical measurements, and the relevance of these studies to the efficiency of photocurrent generation under solar irradiation will be discussed.

PL is the most widely used technique to study excited state dynamics in hybrid perovskite films and devices. Such studies include the determination of charge carrier diffusion lengths and transfer yields in the presence of electron / hole charge transport layers, and in complete devices.[1b, 4] In particular the measurement of steady-state PLQE has been used in many of the pioneering works on perovskite photovoltaics to assess the relationship between interfacial charge transfer, charge extraction and device performance.[4j, 5] In such studies the PLQE is calculated from the ratio of the PL emission intensity of the perovskite layer with and without the quencher interlayers, where the loss of PL is interpreted as a marker of charge transfer. Such PLQE measurements have indicated hole transfer efficiencies for many perovskite materials higher than 95% for a broad range of p-type materials used as hole extracting layers in cells, including NiO, Spiro-OMeTAD, PEDOT:PSS and V_2O_5.[6] Similarly, the PLQE measurements with n-type contacts like PFN and $PC_{61}BM$ have also been found to be very high, often > 98 %,[6] indicative of near unity electron transfer efficiencies. However, despite PLQE measurements indicating near unity electron and hole transfer efficiencies, the resulting device photocurrents have often shown wide variations. This may in part result from contact layer selectivity, with for example PEDOT:PSS having the potential to accept both holes and electrons from $MAPI_3$, thereby potentially resulting, in the absence of appropriate electric fields, in enhanced surface recombination losses.[7] In addition, almost all such PLQE studies have been undertaken in standard PL spectrometers, where the irradiation intensity is typically of the order of a few mW cm^{-2}, one to two orders of magnitude lower than solar irradiation. This key consideration has not been taken into account in most such studies. More limited studies have reported a strong excitation intensity dependence of PL intensity and quenching yields in $MAPI_3$ films in the presence of charge transport layers, although the relevance of this to the kinetics and efficiency of interfacial charge transfer and its impact on device performance

remains unclear.[8] Several studies have also reported that the PL intensity of the MAPI$_3$ films alone are strongly dependent not only upon film processing, but also may evolve following deposition depending upon storage conditions (light exposure, temperature, environment, etc.), further complicating the use of PL measurements as an assay of charge transfer efficiency.[9] As such, it is apparent that employing conventional PLQE spectrometer measurements may not be a reliable tool to assay the efficiency of charge transfer processes in MAPI$_3$ devices operating under 1 Sun irradiation.

In addition to PL quenching measurements, tr-PL, absorption and microwave conductivity measurements have been used to study the kinetics and yields of charge transfer from between the MAPI$_3$ layer and electron / hole transport layers.[3d, 10] Such studies have been conducted with widely varying light excitation densities.[11] Typically, tr-PL measurements are conducted using TCSPC spectrometers, which employ very low energy pulsed irradiation (usually ~ 10 pJ cm^{-2} per pulse) but at relatively high repetition rates (MHz), whilst transient absorption measurements are undertaken at much higher pulse energies (usually 1-10 μJ cm^{-2}) and lower repetition rates (kHz). Both of these irradiation conditions are significantly different from steady-state solar irradiation, complicating considerations of the relevance of the data obtained to device operation.

In this study, the impact of excitation density dependence on the steady-state and transient PL and transient absorption properties of MAPI$_3$ thin films and MAPI$_3$/PC$_{61}$BM and PEDOT:PSS/MAPI$_3$ bilayers is investigated. PC$_{61}$BM and PEDOT:PSS correspond to two widely employed electron and hole transport layers.[8b, 12] It should be noted that whilst PC$_{61}$BM's energy level alignment results in it being a selective contact layer for electron transfer from MAPI$_3$, the high doping of PEDOT:PSS results it being potentially able to accept

both electrons and holes from MAPI$_3$, as discussed above. For simplicity, and consistent with its function in perovskite devices, I will assume herein it functions as primarily as a hole transport layer; a point which is discussed below. Four different experimental techniques were applied to investigate the dynamics of charge transfer as a function of excitation intensity, namely fs-TAS, ss-PL spectroscopy and two pulsed PL measurements operating under very different excitation density ranges: TCSPC under high repetition rate, low pulse energy excitation conditions, and nanosecond time resolution PL measurements operating under low repetition rate, high pulse energy excitation conditions more comparable to those employed in fs-TAS measurements. These techniques allow us to probe the efficiency and kinetics of charge transfer over a broad range of excitation conditions, generating carrier densities in the MAPI$_3$ film ranging from 10^{12} to 10^{18} cm^{-3}. The results from these studies allow us to elucidate how charge density-dependant monomolecular and bimolecular recombination in the MAPI$_3$ film competes with charge transfer under different excitation densities, with important implications for the light intensity dependence of device operation and the identification of suitable experimental protocols to assay these transfer processes under conditions relevant to such device operation.

3.3. Experimental detail

3.3.1. Sample preparation

3.3.1.1. Perovskite layer: Deposition of MAPI$_3$ (CH$_3$NH$_3$PbI$_3$) with the toluene dripping method

For this study, MAPI$_3$ perovskite films were prepared by the toluene anti-solvent dripping method with γ-butyrolactone and dimethyl sulfoxide precursor solvents.[13] For precursor

solution for MAPI$_3$ perovskite, 199 mg/mL of MAI and 576 mg/mL of PbI$_2$ were dissolved in γ-butyrolactone (Aldrich, 99%) and dimethyl sulfoxide (Fluka, 99%) mixed solution with 7:3 volume ratio, and then stirred for 3 hours at 65 °C. Then the solution was filtered through a 0.2 µm PTFE filter before deposition in a N2 filled glove box. To deposit perovskite films, the CH$_3$NH$_3$PbI$_3$ solution (70 µL) was first applied onto a well cleaned substrate (substrate area ~2.5 cm × 2.5 cm). The film was then sequentially spun for 5 seconds at 1000 rpm, for 10 seconds at 1000 rpm, for 19 seconds at 4000 rpm and for 5 seconds at 500 rpm, during which toluene (700 µL) was quickly dropped onto the centre of the substrate, and finally spun for 50 seconds at 4000 rpm. The samples were then annealed at 100°C for 10 minutes.

3.3.1.2. Preparation and deposition of the hole transport layer (HTL): PEDOT:PSS

PEDOT:PSS was filtered through a 0.45 µm filter and spin cast on well cleaned substrate at 3500 rpm for 45 seconds. Then, the sample was dried on a hotplate at 150ºC for 15 minutes in air. Before deposition of the perovskite layer, the samples were annealed additionally 5 minutes at 150 ºC in a glove box.

3.3.1.3. Electron transport layer (ETL): PC$_{61}$BM

[6,6]-phenyl-C61-butyricacidmethyleater (PC$_{61}$BM; 20 mg/mL) dissolved in anhydrous chlorobenzene was deposited on MAPI$_3$ at 2000 rpm for 60 seconds and then 4000 rpm for 10 seconds. Then, the film was left to dry for an hour in a glove box.

3.3.1.4. Top Electrode deposition for device

In this chapter, the top cathode of LiF and Al to complete the devices were deposited by Du Tian (imperial College London) together with JV characterization, including the current density dependent as a function of light intensity. A 10 nm LiF and 100 nm Al layer was deposited through a patterned shadow mask by thermal evaporation at ~10^{-7} mbar high vacuum with a deposition rate of 0.2 nm s^{-1}.

3.3.2. Film characterization

3.3.2.1. Spectroscopy

All the samples were stored for 12 days in a nitrogen-filled glove box at room temperature and kept in the dark after encapsulation before spectroscopy measurements. After this storage time, the PL intensity stabilised, indicating the formation of a stable perovskite film, as will be discussed in detail in chapter 4. UV-Vis spectroscopy, fs-TAS, TCSPC, ss-PL Spectroscopy and LED and nanosecond Pulsed PL Measurements are measured as described in chapter 2.

3.4. Results

This is an established fabrication methodology known to produce dense and highly crystalline MAPI$_3$ films reasonably reproducibly.[14]
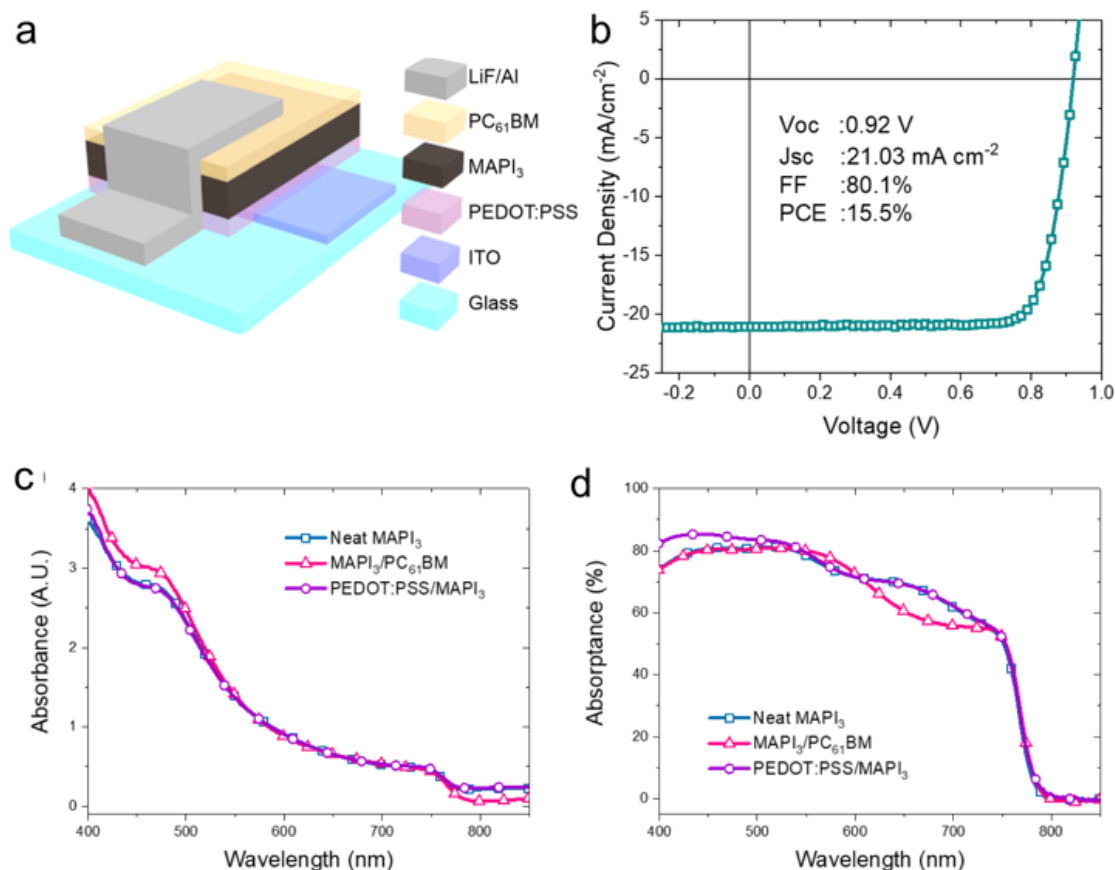
Figure 3.1 a) Device structure of MAPI$_3$ perovskite PV and, b) the power conversion efficiency of the device. c) Absorbance and d) absorptance of neat MAPI$_3$ (blue-green square), MAPI$_3$/PC$_{61}$BM (pink triangles) and PEDOT:PSS/MAPI$_3$ (purple circles).

The 'inverted' device structure of Glass/ITO/PEDOT:PSS/MAPI$_3$/PC$_{61}$BM/LiF/Al was fabricated to test the quality of the films studied and their relevance to published work (following film storage in the glove box as discussed below). Such devices had JV curves typical of those reported for this structure (Figure 3.1a), with power conversion efficiencies of approximately 15.5% for the device structure (Figure 3.1b), and this result is in the range of 13-16 % reported previously.[6, 15] For spectroscopic studies of electron and hole transfer, three

film structures were prepared following the same procedures as for device preparation: MAPI$_3$ ($\approx$ 290 nm thick), MAPI$_3$/PC$_{61}$BM, and PEDOT:PSS/MAPI$_3$.
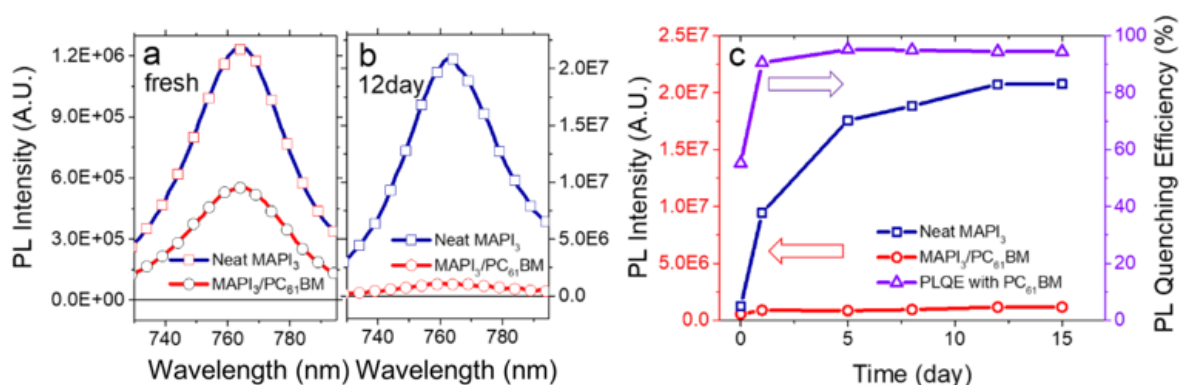

Figure 3.2 PL spectra of MAPI$_3$ and MAPI$_3$/PC$_{61}$BM films measured from a fresh sample (a) and after storage for 12 days (b). The PL peak intensity curve-fitting of neat MAPI$_3$ (blue square) and MAPI$_3$/PC$_{61}$BM (red round), and calculated PLQE were obtained as a function of aging date.

The film absorption and absorptance spectra were typical of well-formed MAPI$_3$ crystals in Figure 3.1c and 3.1d. Consistent with previous reports,[13a] the PL intensity of MAPI$_3$ films was observed to evolve significantly following film fabrication, even for films stored in the dark in a glove box, showing an increase in intensity over a 10 day period before stabilising (Figure 3.2, discussed in more detail in chapter 4). This evolution affects the samples PLQE, as also shown in Figure 3.2. In this study, kinetic measurements of films were performed within 3 days, after 12 days storage in GB after fabrication, thus ignoring the subsequent evolution of thin film PL, so MAPI$_3$ photophysics with storage and/or light exposure time may have a significant impact on the measurement results. The impact of this change of PL intensity affects PL quenching measurements. Note that after this storage treatment, the film PL intensity was relatively insensitive to light soaking, thereby simplifying data analysis (Figure 3.3).
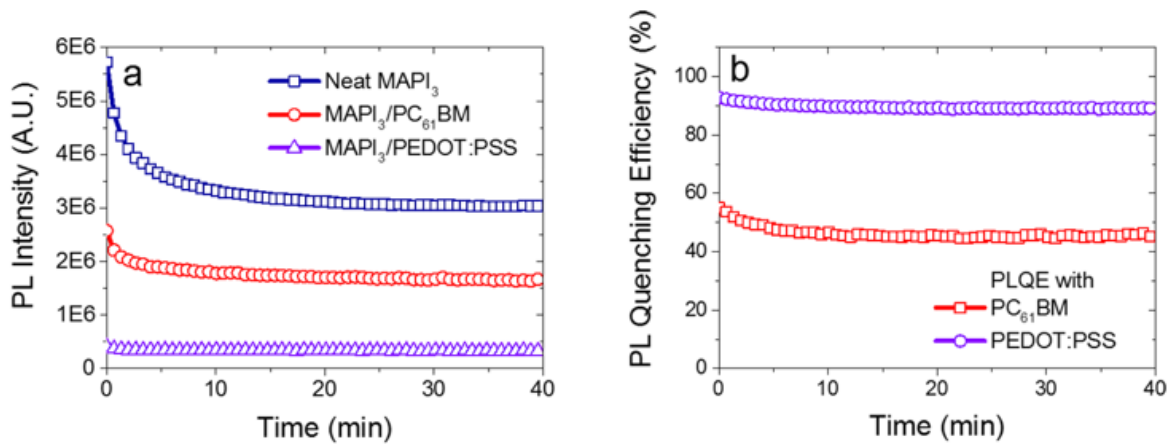
Figure 3.1 PL Light soaking effect of 12 days stabilized films recorded by using 1 Sun LED excitation for 40 min. a) Steady state PL peak intensity of MAPI₃ (blue square), MAPI₃/PC₆₁BM (red circle) and PEDOT:PSS/MAPI₃ (purple triangle) as a function of time. b) PLQE as a function of time.

3.4.1. Steady-state measurement

3.4.1.1. Conventional Steady-state PL and 1 Sun LED PL and quenching efficiency measurement

Figure 3.4 a) Steady-state PL (ss-PL) spectra of neat MAPI₃ (blue-green squares), MAPI₃/PC₆₁BM (pink triangles), and PEDOT:PSS/MAPI₃ (purple circles) films collected in a conventional PL spectrometer with 635 nm excitation at a light fluence of 1.5 mW cm⁻²; b) Equivalent PL spectra of the same films collected using a white light LED excitation source with a power output selected to be equivalent to 1 Sun fluence.

Figure 3.4a shows the conventional ss-PL spectra of MAPI₃, MAPI₃/PC₆₁BM, and

PEDOT:PSS/MAPI₃ films recorded with 635 nm excitation at a light fluence of 1.5 mW cm⁻²,

corresponding to typical fluorimeter excitation conditions. This excitation is much lower than the photon fluence under 1 Sun AM 1.5 conditions (approximately 1.8% of 1 sun). The neat $MAPI_3$ (blue-green squares) film shows typical strong emission with a maximum at ~ 765 nm, as expected for this material.[10a, 16] The PL from $MAPI_3$ in the $MAPI_3/PC_{61}BM$ (pink triangles) and PEDOT:PSS/$MAPI_3$ (purple circles) films is strongly quenched by the presence of the interlayers. The PLQE obtained for $MAPI_3/PC_{61}BM$ is 91% and for PEDOT:PSS/$MAPI_3$ it is 97%. Following the fabrication and storage procedure detailed above, this PLQE measurement was found to be reproducible within ± 2 % and insensitive to light pre-soaking. These PLQE data are consistent with the values reported in the literature.[6, 8a, 10c] However and indicate reasonably efficient transfer of electrons and holes from $MAPI_3$ to $PC_{61}BM$ and PEDOT:PSS respectively under this irradiation condition.

In addition to this standard method for assessment of PLQE, the PL spectra of the films were recorded using a white light LED excitation source with a power output selected to correspond to circa 1 Sun photon fluence. Figure 3.4b presents the PL spectra of the samples, which show differing relative amplitudes from those measured with the standard spectrometer light excitation source (Figure 3.4a). In particular, while the PLQE of the PEDOT:PSS/$MAPI_3$ film is unchanged at 97%, the PLQE of $MAPI_3/PC_{61}BM$ is substantially lower, dropping from 91% down to 46%. This result clearly indicates the importance of light intensity when conducting PLQE measurements, particularly when considering the ability of electron transfer to compete with charge trapping and recombination within the $MAPI_3$ film.

3.4.1.2. Excitation dependence of LED PL
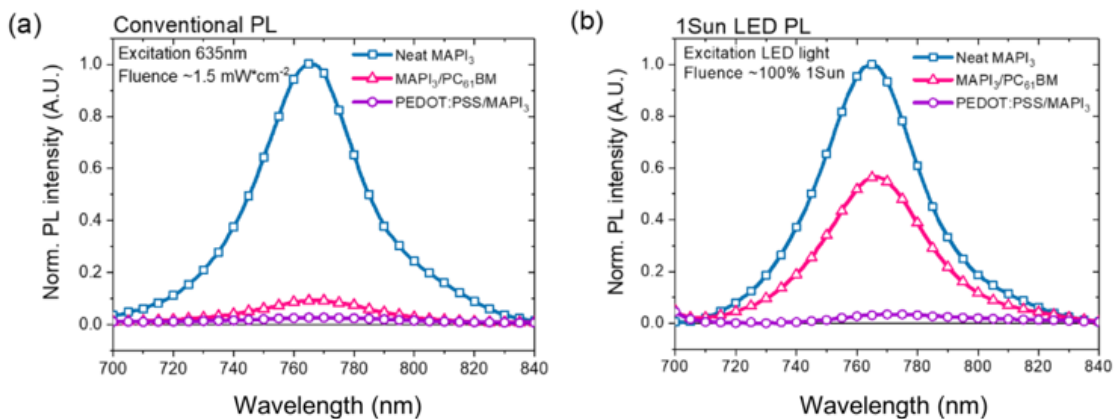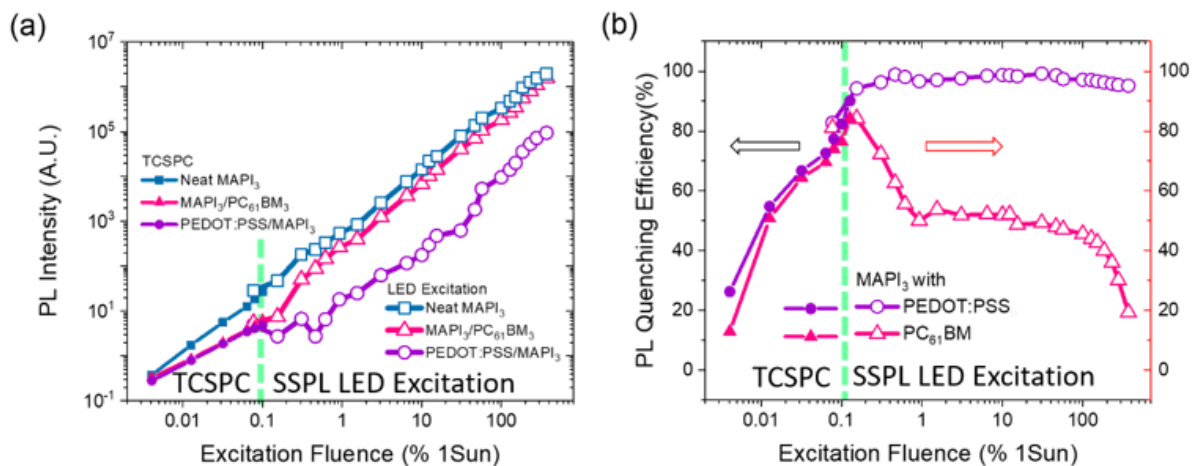
Figure 3.5 a) Integrated PL intensities acquired with steady-state PL spectrometer of neat MAPI₃ (blue-green squares), MAPI₃/PC₆₁BM (pink triangles), and PEDOT:PSS/MAPI₃ (purple circles) films plotted on a double-logarithmic scale for excitation densities ranging from 0.0008 to 3.7-fold 1 Sun equivalent; Open symbols correspond to data obtained using CW LED irradiation, whilst closed symbols correspond to integrated TCSPC decays; b) The corresponding photoluminescence quenching efficiencies are determined from these PL data.

Figure 3.5a (open symbols) shows the integrated PL intensities of neat MAPI₃, MAPI₃/PC₆₁BM and PEDOT:PSS/MAPI₃ films plotted as a function of excitation intensity (I_{ex}) from a white light LED source with irradiation intensities equivalent to 0.0008 to 3.7 Suns.
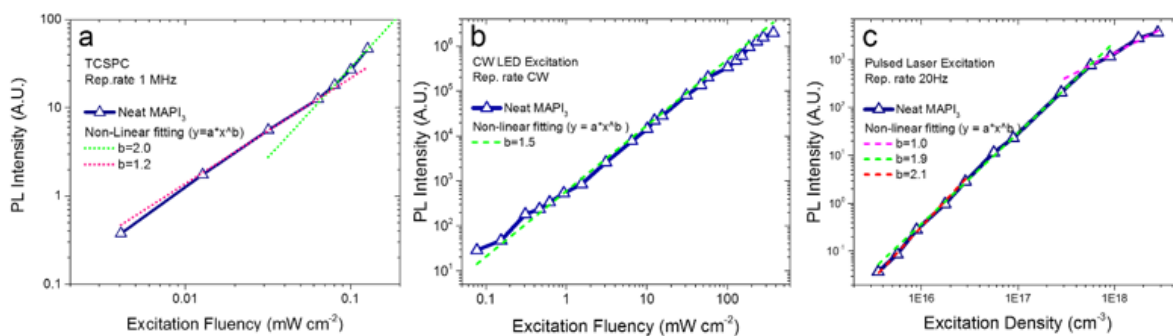
Figure 3.6 PL intensity of neat MAPI₃ film versus excitation density and power law fitting measured using a) TCSPC (integrate area of dynamics) b) filtered-LED excitation and c) Nd:YAG laser excitation.

The results, plotted with double-logarithmic scales, show that for the neat MAPI₃ film, the PL intensity (PL_0) follows approximately $PL_0 \alpha I_{ex}^{\beta}$ where $\beta \sim 2$ at low intensities and ~ 1 at high intensities. (Figure 3.6) Similar super-linear behaviour has been reported previously, [2a, 17] and

assigned to a transition from primarily monomolecular processes at low intensities to bimolecular processes at higher intensities, as discussed further below. Both bilayer films also showed super-linear, but more complex, dependencies of PL intensity upon excitation intensity, as analysed further below. The PL data shown in Figure 3.5a was employed to determine the light intensity dependence of the PLQE for the bilayers $MAPI_3/PC_{61}BM$ and $PEDOT:PSS/MAPI_3$, as plotted in Figure 3.5b (open symbols). The PLQE of $MAPI_3/PC_{61}BM$ peaks near 84% at a low fluence (0.15% of 1 Sun) and decreases to 50% at 93% of 1 Sun before plateauing. The PLQE decreases again for intensities above 1 Sun. The PLQE of $PEDOT:PSS/MAPI_3$ rises from an initial value of 83% and reaches 98% at about 50% of 1 Sun, and retains this high value until dropping slightly (by ~ 1 %) for excitation intensities above 1 Sun.

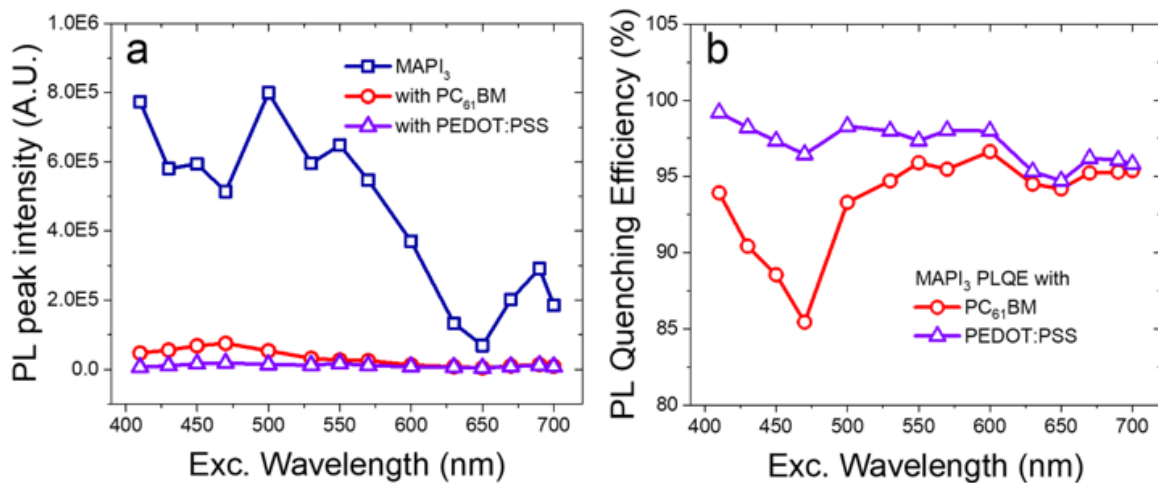*Figure 3.7 a) Conventional steady state PL intensity measurement by a function of excitation wavelength with 1.5 mW cm^{-2} excitation fluenece, and b) PLQE.*

Note that the PLQE was also observed to exhibit a modest dependence upon excitation wavelength (Figure 3.7), which explains the modest difference in PLQE's determined from the monochromatic excitation data in Figure 3.4 and the white light excitation in Figure 3.5.
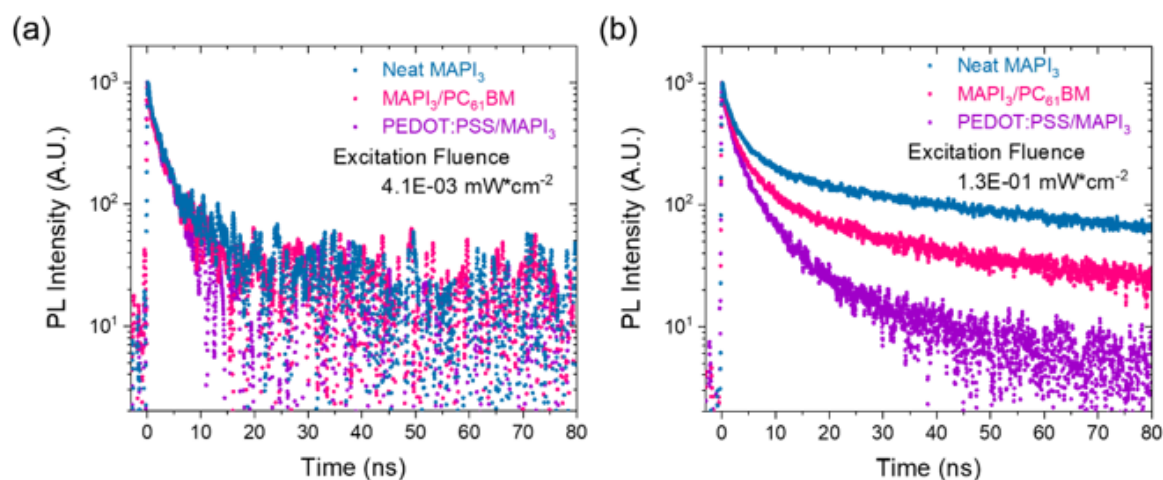
Figure 3.8 TCSPC decay dynamics of the films measured under a) 4.1 × 10^{-3} mW cm^{-2} and b) 1.3 × 10^{-1} mW cm^{-2} excitation densities (circa 0.0041 and 0.13 % of 1 Sun respectively).

I turn now to TCSPC measurements of the PL decay kinetics for the three samples studied. TSCPC is widely employed to study PL decay dynamics in MAPI$_3$ films and is typically, as based on measurements of single photons, undertaken at very low excitation fluences. For the study herein, A pulse repetition rate of 1 MHz and pulse densities in the range of 5.7 to 178 pJ cm^{-2} were employed, corresponding to quasi-CW irradiation intensities ranging from 0.004 to 0.13 mW cm^{-2}. Note that this excitation range, which is typical of TCSPC studies, is lower than the excitation densities employed for the other techniques employed in this study.

TCSPC data collected at the 765 nm peak position of PL for neat MAPI$_3$ films and the two bilayers at the lowest and highest intensities are shown in Figure 3.6a and 3.6b; full data sets over a range of intensities for each film, and the double exponential fitting parameter and the plot as a function of excitation fluence are shown in Figure 3.9, Table 3.1 and Figure 3.10, respectively.

Figure 3.9 TCSPC dynamics data collected at 765 nm for a) neat MAPI₃, b) MAPI₃/PC₆₁BM, and c) PEDOT:PSS /MAPI₃ measured at various excitation fluence.

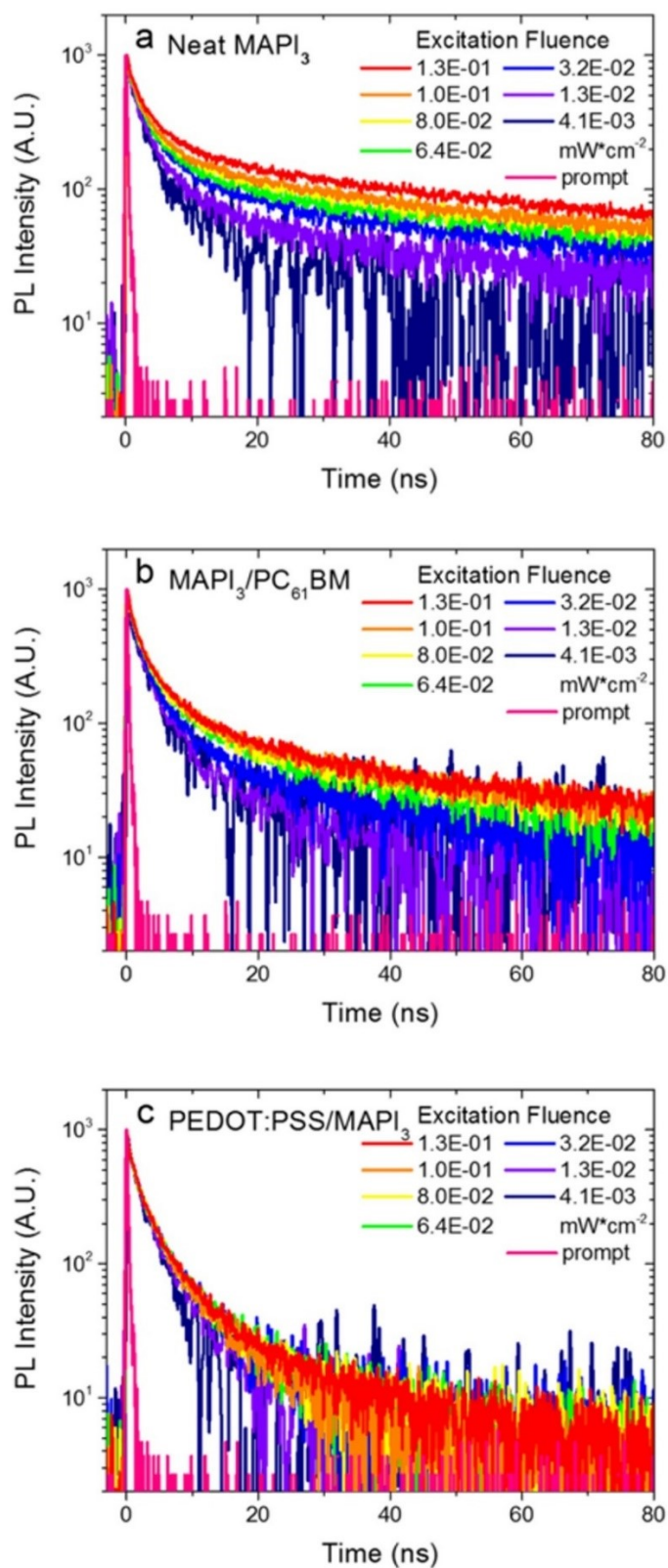| Sample	Excitation Fluence [mW cm^{-2}]	A^1			τ^1 [ns]			A^2			τ^2 [ns]		
neat MAPI$_3$	4.1E-03	863.7	±	5.8	1.7	±	0.02	124.5	±	3.4	17.7	±	0.46
	1.3E-02	856.5	±	3.4	1.8	±	0.01	128.6	±	1.2	31.5	±	0.36
	3.2E-02	853.4	±	2.6	2.3	±	0.01	134.4	±	0.9	48.9	±	0.45
	6.4E-02	782.1	±	2.6	2.3	±	0.01	146.3	±	0.8	56.5	±	0.49
	8.0E-02	766.9	±	2.6	2.3	±	0.01	168.2	±	0.8	56.0	±	0.42
	1.0E-01	765.1	±	2.7	2.3	±	0.01	176.0	±	0.8	56.4	±	0.42
	1.3E-01	764.5	±	2.7	2.3	±	0.01	209.9	±	0.8	59.7	±	0.39
MAPI$_3$/PC$_{61}$BM	4.1E-03	820.0	±	6.9	1.8	±	0.03	127.2	±	5.3	14.5	±	0.54
	1.3E-02	828.1	±	3.2	1.8	±	0.01	128.9	±	2.5	14.3	±	0.25
	3.2E-02	809.3	±	3.1	1.9	±	0.01	126.1	±	1.5	24.7	±	0.33
	6.4E-02	777.8	±	2.6	2.1	±	0.01	126.8	±	1.2	31.7	±	0.33
	8.0E-02	772.9	±	2.6	2.1	±	0.01	126.6	±	1.1	35.4	±	0.37
	1.0E-01	780.1	±	2.9	2.1	±	0.01	132.1	±	1.2	36.9	±	0.40
	1.3E-01	785.2	±	2.8	2.1	±	0.01	135.1	±	1.1	36.7	±	0.38
PEDOT:PSS/MAPI$_3$	4.1E-03	751.0	±	12	1.7	±	0.04	171.2	±	13	7.4	±	0.39
	1.3E-02	717.2	±	5.3	1.7	±	0.02	169.9	±	5.7	8.0	±	0.18
	3.2E-02	745.0	±	3.3	1.8	±	0.01	167.6	±	3.4	10.2	±	0.15
	6.4E-02	719.9	±	3.1	1.8	±	0.01	155.1	±	3.0	11.2	±	0.17
	8.0E-02	736.2	±	3.1	1.9	±	0.01	150.0	±	3.2	10.7	±	0.17
	1.0E-01	728.3	±	3.1	1.9	±	0.01	150.1	±	3.0	11.2	±	0.18
	1.3E-01	729.5	±	3.1	1.9	±	0.01	149.1	±	3.2	10.4	±	0.17

Table 3.1 Double exponential fitting parameter ($y = A_1 \times exp(-x/\tau_1) + A_2 \times exp(-x/\tau_2) + y_0$) of TCSPC dynamics data at 765 nm of neat MAPI$_3$, MAPI$_3$/PC$_{61}$BM, and PEDOT:PSS/MAPI$_3$ measured with various excitation fluenece.
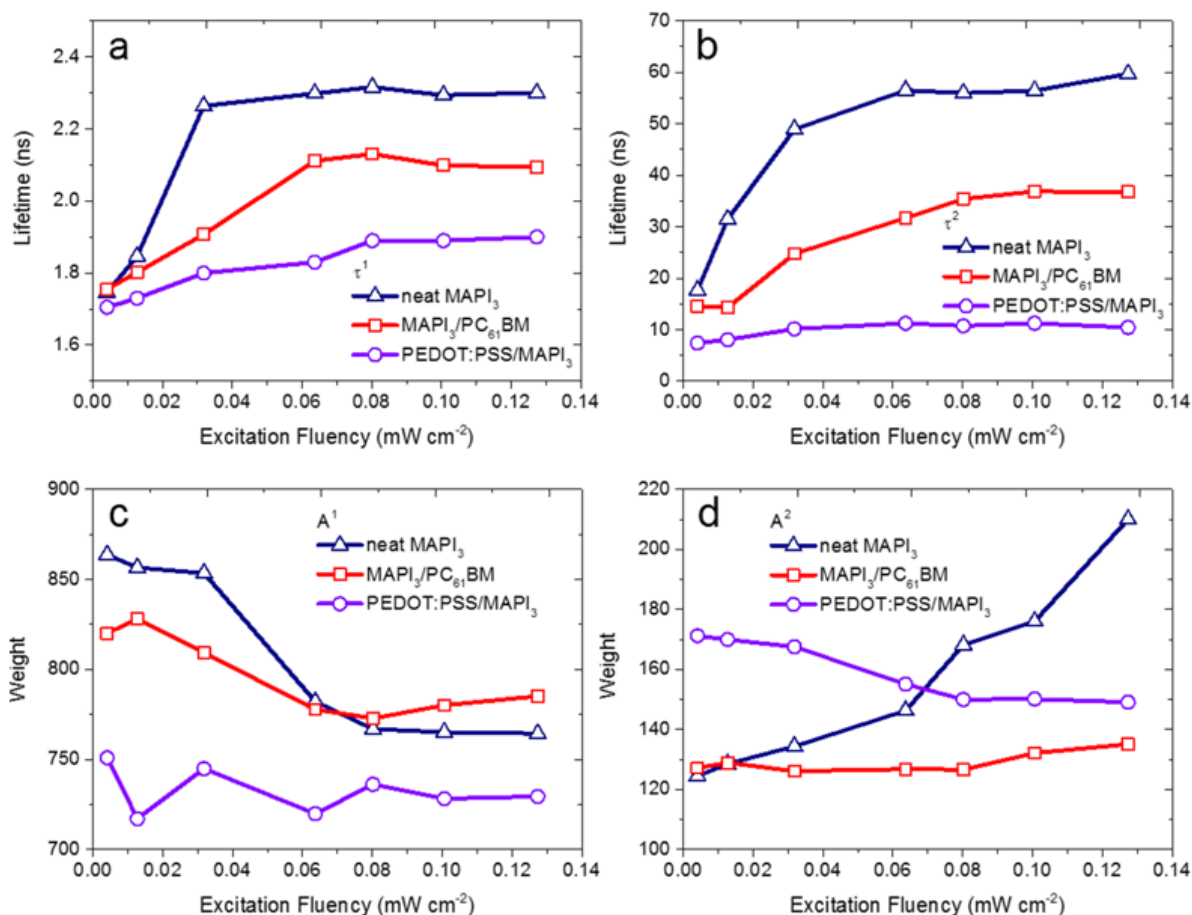
Figure 3.10 Excitation fluence dependent double exponential fitting parameters (y = A$_1$×exp(-x/τ$_1$) + A$_2$×exp(-x/τ$_2$) + y$_0$) of neat MAPI$_3$ (blue square), MAPI$_3$/PC$_{61}$BM (red circle) and PEDOT:PSS/MAPI$_3$ (purple triangle) from TCSPC data. a) τ$_1$, b) τ$_2$, c) A$_1$ and d) A$_2$.

For the lowest excitation density (Figure 3.8a), almost identical PL decays are seen for the MAPI$_3$, MAPI$_3$/PC$_{61}$BM and PEDOT:PSS/MAPI$_3$ films, with all three samples exhibiting a rapid, exponential (τ ~ 1.7 ns) decay. At higher excitation densities, a slower, 10's of nanoseconds, decay phase is increasingly apparent, with this phase being largest and slowest for the MAPI$_3$ film alone (Figures 3.8a, 3.8b, and 3.9). Following literature studies, the fast (1.7ns) decay phase is assigned to monomolecular charge trapping, and the 10's of nanoseconds decay phase to bimolecular recombination, with the increasing dominance of this fast few nanosecond decay phase at higher excitation intensities assigned to trap filling.[18] The observation of similar decay kinetics for all three samples at the lowest excitations conditions

indicates that electron / hole transfer to $PC_{61}BM$ / PEDOT:PSS is unable to compete kinetically with charge trapping at this excitation condition. It further indicates that charge trapping is not changed by the presence of the contact layers, indicating that the PLQ observed at higher excitation conditions does not derive from increased charge trapping due to for example the generation of surface defects, but rather from charge transfer to the contact layers. At the higher excitation conditions, the 10's of nanosecond decay phase is strongly quenched by these layers, indicative of electron / hole transfer competing effectively with bimolecular recombination.[3b, 8a] This behaviour is further illustrated in Figures 3.5a and 3.5b (solid symbols), where plots of the integrated PL intensity and quenching efficiencies determined from these TCSPC data are shown to be in excellent agreement with, and extend to lower light fluxes, the data obtained with continuous irradiation. For both bilayers, the slow decay phase time constant saturates at higher excitation densities (Figure 3.10b) with decay time constants of 36 and 11 ns with $PC_{61}BM$ and PEDOT:PSS respectively. These correspond to conditions of efficient electron / hole transfer, and thus indicate transfer times of circa 36 and 11 ns for electron and hole transfer respectively. The saturation of this decay time for both bilayers indicates that the kinetics of electron / hole transfer are relatively intensity independent, as expected for a monomolecular charge transfer process. As such, the intensity dependence of the PL decays and the PLQE data determined from these TCSPC data are assigned to the intensity dependence of competing charge trapping and bimolecular recombination processes in the $MAPI_3$ film itself.

The non-linear PL and PLQE intensity dependencies shown in Figures 3.4 and 3.5 can be understood as resulting from variations in charge carrier density with excitation density. However, this dependence is difficult to access directly from these (quasi-)steady-state spectroscopic studies, as the accumulated charge carrier density will depend upon the carrier lifetimes, which are themselves excitation density (and transport layer) dependent. As such we

turn now to slower repetition rate pulsed laser measurements, where it is reasonable to assume no charge accumulation between laser pulses. For such measurements, the pulse energy can be directly converted into initial densities of photoinduced charge carriers, assuming that all absorbed photons generate charge carriers. For reference, it should be noted that previous differential charge measurements on analogous devices have indicated charge carrier densities in similar $MAPI_3$ films of $\sim 10^{16}$ cm^{-3} under 1 Sun equivalent irradiation at open circuit, decreasing with lower light intensities.[19]

3.4.2. Pulsed static-state PL and quenching efficiency measurement system

3.4.2.1. Pulsed laser PL and quenching efficiency measurement
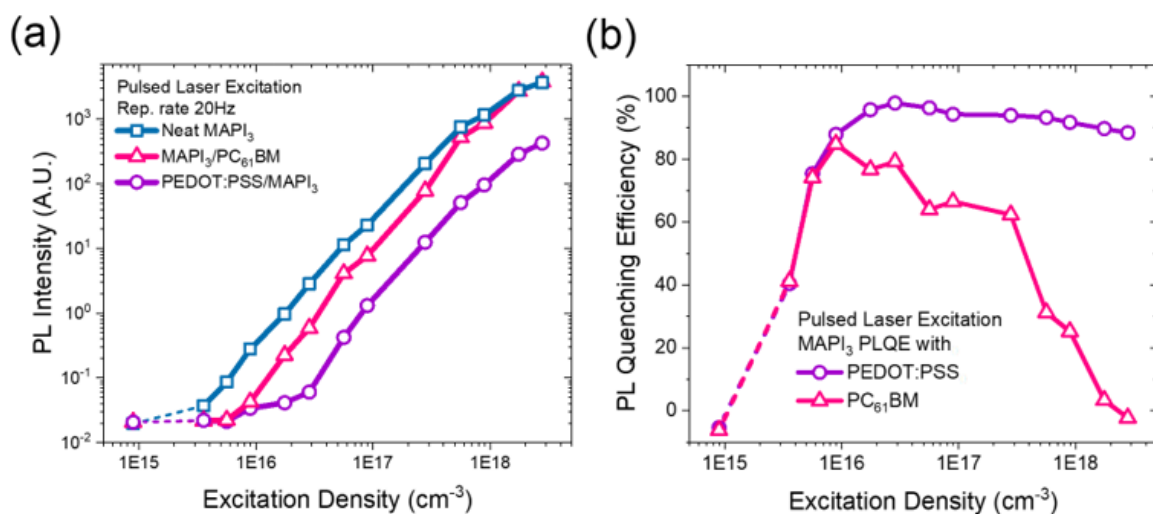
Figure 3.11 a) Integrated PL amplitudes of neat MAPI₃ (blue-green squares), MAPI₃/PC₆₁BM (pink triangles), and PEDOT:PSS/MAPI₃ (purple circles) films determined using low repetition-rate pulsed laser excitation, plotted on double-logarithmic scales for excitation densities ranging from 9 × 10¹⁴ to 3 × 10¹⁸ cm⁻³; b) MAPI₃ film PLQE with PC₆₁BM (pink triangles) and PEDOT:PSS (purple circles) determined from data as a function of excitation density.

Low repetition rate pulsed PL measurements, employing a pulsed Nd:YAG OPO laser (5 ± 2 ns pulse width, 20 Hz) and Si-photodiode detector with a 200 ns response function are considered first. The peak PL intensity of the three samples were recorded for different

excitation densities, and therefore approximate carrier densities, ranging from 9×10^{14} to 3×10^{18} cm^{-3}, as plotted in Figure 3.11a. Based on these data, the PLQE of the samples were calculated and plotted in Figure 3.11b. Both bilayers show a rise PLQE up to 10^{16} cm^{-3} excitation density, followed by a drop in PLQE for higher excitation densities. The dependence on excitation density is much more pronounced for MAPI$_3$/PC$_{61}$BM, as also observed in the steady-state PLQE data (Figure 3.5b). These data suggest that at carrier densities $\sim 10^{16}$ cm^{-3}, further charge trapping into non-radiative trap states is inhibited, allowing efficient charge transfer of the excess charge carriers. At higher carrier densities however the PLQE decreases with increasing excitation intensity due to increasing band-to-band bimolecular recombination and possible Auger recombination.[20]

3.4.2.2. Femtosecond transient absorption spectroscopy (Charge transfer VS bimolecular recombination)
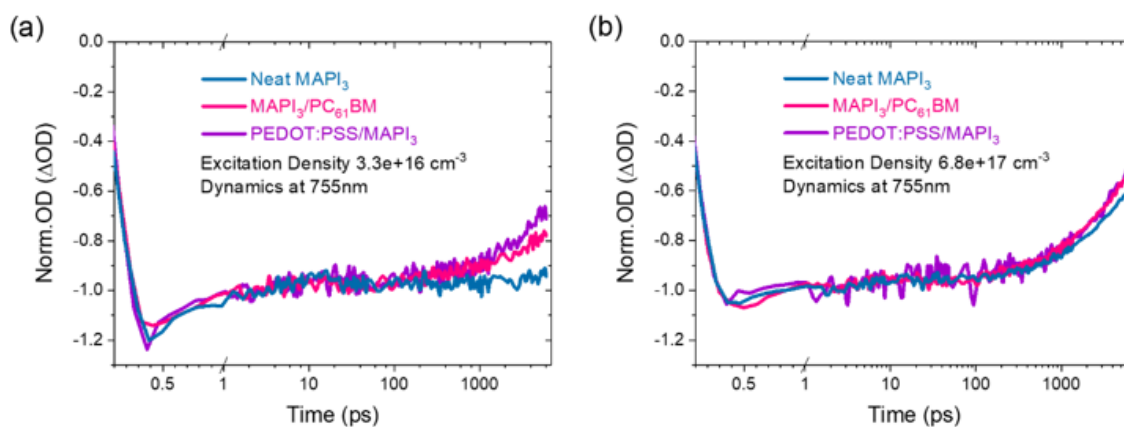
Figure 3.12 Comparison of kinetics of neat MAPI$_3$ (blue-green line) probed at 755 nm for time delays up to 6 ns with MAPI$_3$/PC$_{61}$BM (pink line) and PEDOT:PSS /MAPI$_3$ (purple line) at excitation densities of a) 3.32×10^{16} and b) 6.77×10^{17} cm^{-3}. Time axes are linear up to 1 ps and logarithmic thereafter.

Finally, we turn to fs-TAS studies. TAS is another optical technique widely used for charge transfer studies in perovskite devices.[21] However, due to its lower sensitivity, it is normally

conducted at much higher excitation densities than most PL techniques. The excitation densities were varied between 10^{16} and 10^{18} cm^{-3} and the photogenerated charge dynamics probed by recording the absorption change at the maximum of the negative signal at 755 nm, (Figure 3.13) typically assigned to the MAPI$_3$ ground state bleaching.[1c, 22]
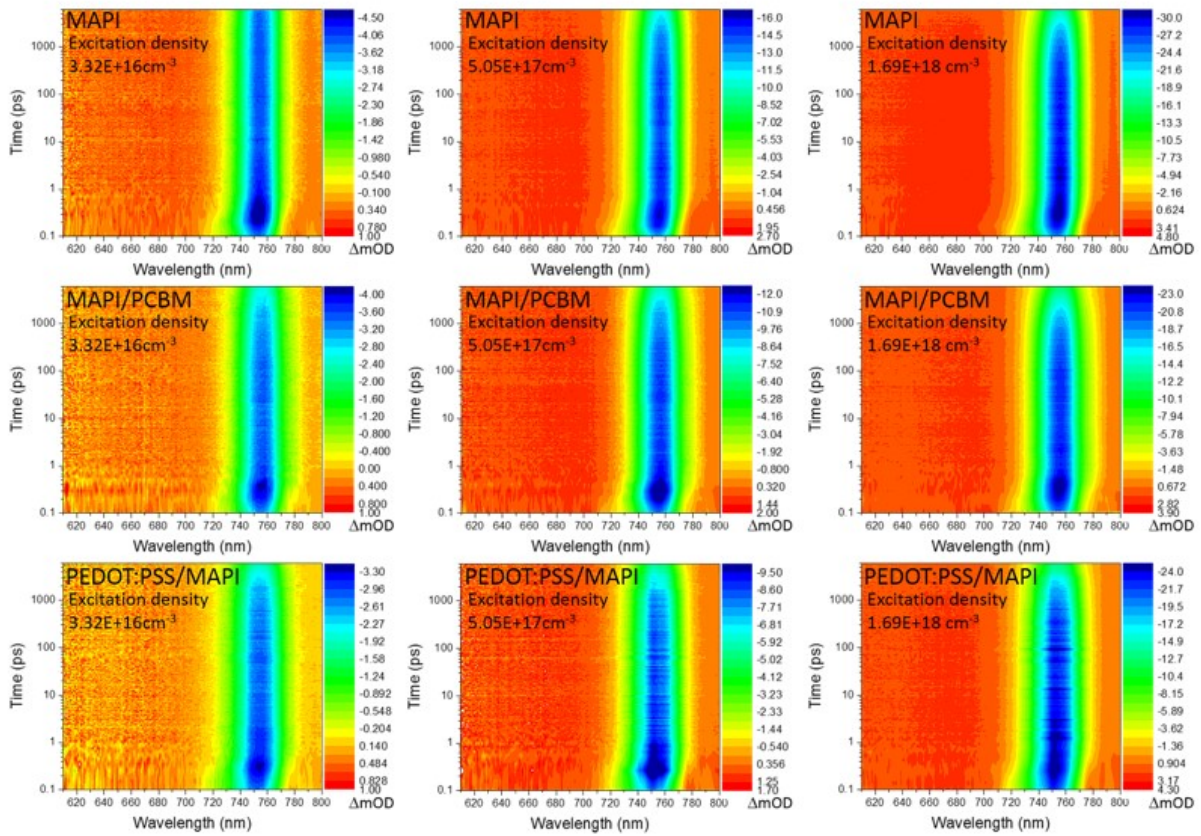

Figure 3.13 2D colour filled plot of ultra-fast transient absorption of neat MAPI$_3$, MAPI$_3$/PC$_{61}$BM and PEDOT:PSS/MAPI$_3$ with various excitation density.
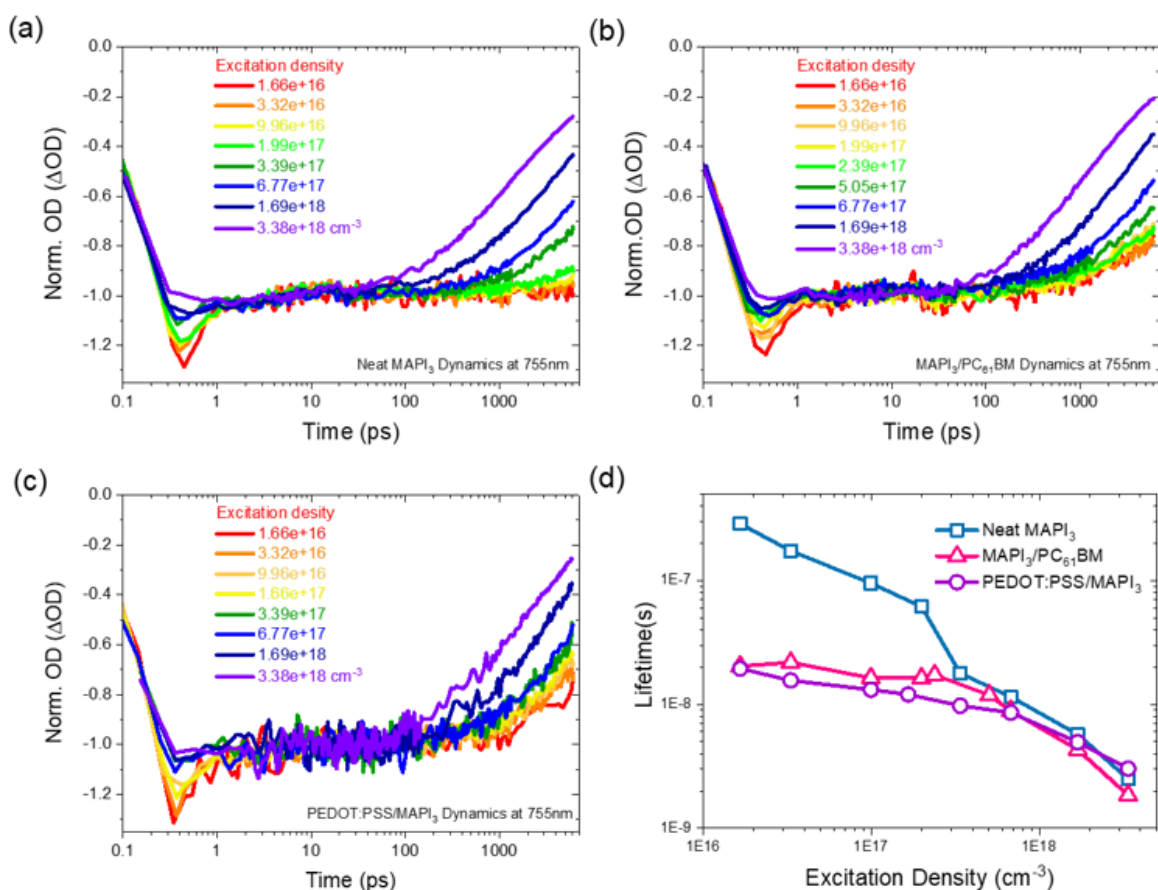
Figure 3.14 Normalised dynamics of ultra-fast transient absorption with various excitation densities used in the study of a) neat MAPI$_3$, b) MAPI$_3$/PC$_{61}$BM, and c) PEDOT:PSS/MAPI$_3$; d) Lifetime of ultra-fast transient absorption dynamics of neat MAPI$_3$ (blue-green squares), MAPI$_3$/PC$_{61}$BM (pink triangles), and PEDOT:PSS/MAPI$_3$ (purple circles) as a function of excitation density.

Figure 3.14 plots the dynamics of the neat MAPI$_3$, MAPI$_3$/PC$_{61}$BM, and PEDOT:PSS/MAPI$_3$ bleach signal for time delays up to 6 ns as a function of excitation density. There are two excitation density dependent decay phases apparent in these data: an initial sub-ps decay which disappears at higher excitation densities and a much slower (nanosecond) decay phase which appears only at higher excitation densities. Such data are similar to those reported previously; the sub-ps decay phase is assigned to ultrafast charge trapping/relaxation that saturates at higher laser intensities, whilst the slower decay is assigned to bimolecular charge recombination.[2c, 3a, 21d, 22a, 23] Figure 3.12a and 3.12b compare the bleach decay kinetics of neat MAPI$_3$ with MAPI$_3$/PC$_{61}$BM and PEDOT:PSS/MAPI$_3$ bilayers at excitation densities of 3.3×10^{16} and 6.8

$\times$ 10^{17} cm^{-3} respectively. The former excitation density corresponds to carrier densities near those in devices under 1 Sun irradiation. At this excitation density, negligible bimolecular recombination is observed for the MAPI$_3$ film alone over the timescale plotted (up to 6 ns). In contrast, both bilayers show significant nanosecond decays, which can be attributed to electron transfer to PC$_{61}$BM and hole transfer to PEDOT:PSS. Note that the given limited time range of the data, transfer times cannot be accurately estimated from these data, although they appear consistent with the 10's of nanosecond timescale determined from the TCSPC data above. For the higher excitation density, 6.8×10^{17} cm^3, the MAPI$_3$ film alone shows a significant nanosecond decay phase (decay time $\sim$ 8 ns), assigned to bimolecular recombination (note under these conditions, excessive charge accumulation on the contact layers may also impede charge transfer). Both bilayers show only marginally faster decay kinetics than the MAPI$_3$ film alone, indicative of the 8 ns estimated bimolecular recombination time being faster than the time constants for electron / hole transfer. (See Figure 3.14d for lifetime fitting) This result is also consistent with the loss of PLQE observed at high excitation densities in Figure 3.7, and is indicative that under these excitation conditions, electron / hole transfer is unable to kinetically compete with rapid bimolecular charge recombination in the MAPI$_3$ film.

3.5. Discussion

PL spectroscopy is a standard technique used for studying the interfacial charge transfer properties of photovoltaic devices, including perovskites. By measuring the PL intensity of the photoactive layer with and without the charge transport layers, one can in principle determine the fraction of charge carriers that are transferred across the interfaces and, if combined with time-resolved data, the rate constants for these charge transfers. The efficiency of these charge transfer processes is a key consideration for photocurrent generation in complete devices.

3.5.1. Charge carrier dynamics on MAPI$_3$ with ETL and HTL

It is apparent from the data presented herein that measurement of the efficiency of electron transfer for MAPI$_3$/PC$_{61}$BM bilayers and hole transfer for PEDOT:PSS/MAPI$_3$ bilayers is strongly dependent upon the excitation conditions employed. In particular, it is apparent that the PLQE measured in a standard PL spectrometer can yield significantly different transfer efficiencies to those measured under 1 Sun equivalent irradiation, due to the relatively low excitation conditions employed in standard spectrometers. Furthermore, transient spectroscopic measurements measured under pulsed laser excitation may also yield very different transfer efficiencies depending upon the excitation conditions employed. As demonstrated, TCSPC measurements can yield relatively low transfer efficiencies due to the excitation densities being much lower than 1 Sun irradiation, and ultrafast transient absorption measurements can yield relatively low transfer efficiencies for the opposite reason of employing higher excitation density conditions than those relevant to 1 Sun irradiation.

The primary cause of this dependence of transfer efficiency upon excitation conditions is the dependence of charge trapping and recombination in MAPI$_3$ upon charge carrier density. It is already well established that the recombination dynamics in MAPI$_3$ films is charge density dependent and can be dominated by Shockley-Read-Hall recombination to sub-bandgap trap states (1st order with respect to charge density) at low charge densities, by free electron-hole bimolecular recombination (2nd order with respect to charge density) at intermediate charge densities, and by Auger recombination (3rd order process) at very high charge densities.[2e, 2f, 17b] Auger recombination only becomes dominant at very high charge densities ($\geq$ 2-5 $\times$ 10^{18} cm^{-3}) as described,[1e, 20, 24] outside the scope of this study. The transition from 1st to 2nd order

recombination has been suggested to occur when the density of photogenerated charge carriers exceeds the trap density, resulting in a saturation of charge trapping.[2a-c]

3.5.2. Charge-carrier dynamics model on perovskite
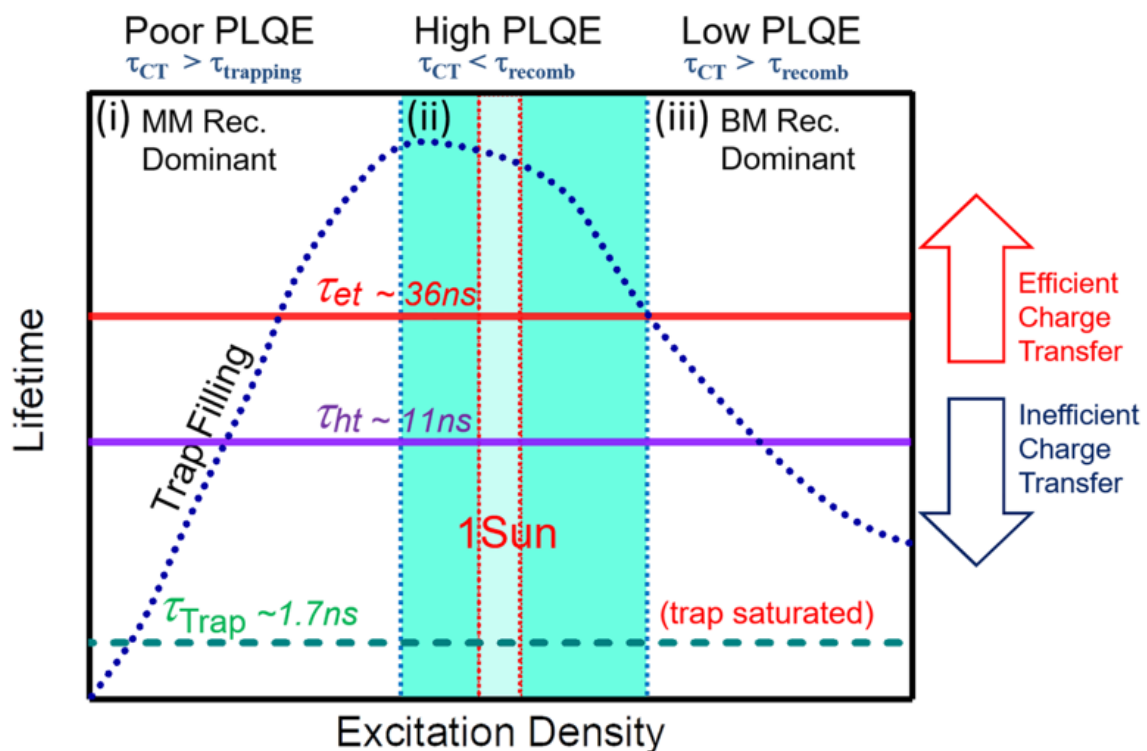
Figure 3.15 Illustration of the excitation density dependence of the competing interfacial charge transfer kinetics and yields vs charge trapping and recombination. Y-axis corresponds to measured charge lifetimes.

The excitation density dependence of PLQE, and therefore charge transfer efficiencies, can be understood in terms of the charge carrier density dependence of charge trapping and recombination, as illustrated in Figure 3.15. At low excitation densities, nanosecond charge trapping processes compete effectively with charge transfer to the $PC_{61}BM$ and PEDOT:PSS layers, resulting in low PLQE's. At intermediate excitation densities, this charge trapping saturates due to trap filling, enabling efficient electron / hole transfer. This transition to efficient

charge transfer occurs for the bilayers studied at steady-state light fluxes of circa 0.01 Sun, or a charge density of $\sim 5 \times 10^{15}$ cm^{-3} from our pulsed laser measurements. As the excitation intensity, and resulting charge density, is increased further, bimolecular recombination accelerates and begins to compete with charge transfer for densities greater than circa. 3×10^{17} cm^{-3}. Under 1 Sun irradiation, hole transfer in PEDOT:PSS/MAPI$_3$ bilayer remains efficient, but the electron transfer efficiency in MAPI$_3$/PC$_{61}$BM bilayers drops to circa 50 %. At higher excitation conditions, both hole and, particularly, electron transfer efficiency drops further as bimolecular recombination accelerates.

From the TCSPC data shown in Figure 3.10, excitation density independent electron / hole transfer lifetimes of circa 36 and 11 ns respectively can be estimated. These measured time constants for electron and hole transfer may be limited by either charge transport to the bilayer interfaces or by electron / hole transfer at these interfaces. In this regard, the faster time constant for the PEDOT:PSS/MAPI$_3$ bilayer is consistent with the higher hole mobility reported for MAPI$_3$ relative to its electron mobility, and with the higher PLQE, observed for this bilayer.[25] Literature data for these charge transfer times to PC$_{61}$BM and PEDOT:PSS are in the range of 0.4 - 15 ns and of 6 – 90 ns for electron and hole transfer, respectively.[3d, 26] It is not clear if these variations reflects variations in sample preparation, measurement technique or excitation density. Some of these measurements employed very low excitation conditions where competition with charge trapping is likely to be critical. It should be noted that most studies measured kinetics on films shortly after fabrication, where the subsequent evolution of film PL, and therefore MAPI$_3$ photophysics, with storage and/or light exposure time may have significant impact. Furthermore, the TCSPC measurements in Figure 3.8a at low excitation densities indicate that charge trapping kinetics are not changed by the presence of PC$_{61}$BM and

PEDOT:PSS contact layers, indicating that neither contact layer generates a significant number of surface defects/recombination centres.

As discussed above, the PLQE data in Figure 3.11b as a function of pulse energy indicate that charge trapping no longer competes effectively with charge transfer for excitation densities of $\sim 10^{16}$ cm^{-3}. Indeed, increasing the excitation density to only 3×10^{15} cm^{-3} already results in an increase in PLQE, and therefore charge transfer efficiency, to 40% (Figure 11b). These data suggest that these relatively low excitation densities are sufficient to result in enough trap filling to enable efficient charge transfer.[27] These data, however, contrast with other assays of trap density in MAPI$_3$ films, based on for example analysis of ss-PL versus light flux, which more typically yield trap densities of $\sim 10^{17}$ cm^{-3}.[1d, 18a] The origin of this apparent discrepancy is not fully determined. However there is likely to be a distribution of trap depths in MAPI$_3$ films, as this study and others have discussed elsewhere,[4h, 19, 28] with charge trapping being relatively irreversible for deeper traps, but more reversible (on the nanosecond timescale relevant to charge transfer) for shallower trap states (sometimes referred to as 'tail states'). It appears reasonable that trapping into a relatively low density of deeper traps competes effectively with charge transfer, whilst the presence of a higher density of shallow tail states, whilst impacting upon PL density, has relatively little impact upon the efficiency of charge transfer.

3.5.3. Steady and static state

The steady-state PLQE versus light flux plot in Figure 3.5b shows a drop in PLQE from ~84% to 55% between 0.1 and 1% of 1 Sun for in MAPI$_3$/PC$_{61}$BM bilayers. An equivalent drop in PLQE is not observed in the low repetition rate pulsed PLQE measurements (Figure 3.11b).

Whilst a quantitative comparison between steady-state and pulsed measurements is challenging, it appears most likely that this drop in PLQE at modest steady-state light fluxes is associated with charge accumulation in the $PC_{61}BM$ layer impeding electron transfer in the steady-state measurements. In the pulsed measurements, where the bilayers recover to their dark charge densities between light pulses, such charge accumulation will have less impact. Such charge accumulation is likely to be particularly important in complete devices under open circuit conditions, and less critical at short circuit where charges are extracted to the external circuit. However, study of such issues requires data on complete devices, beyond the scope of this study.

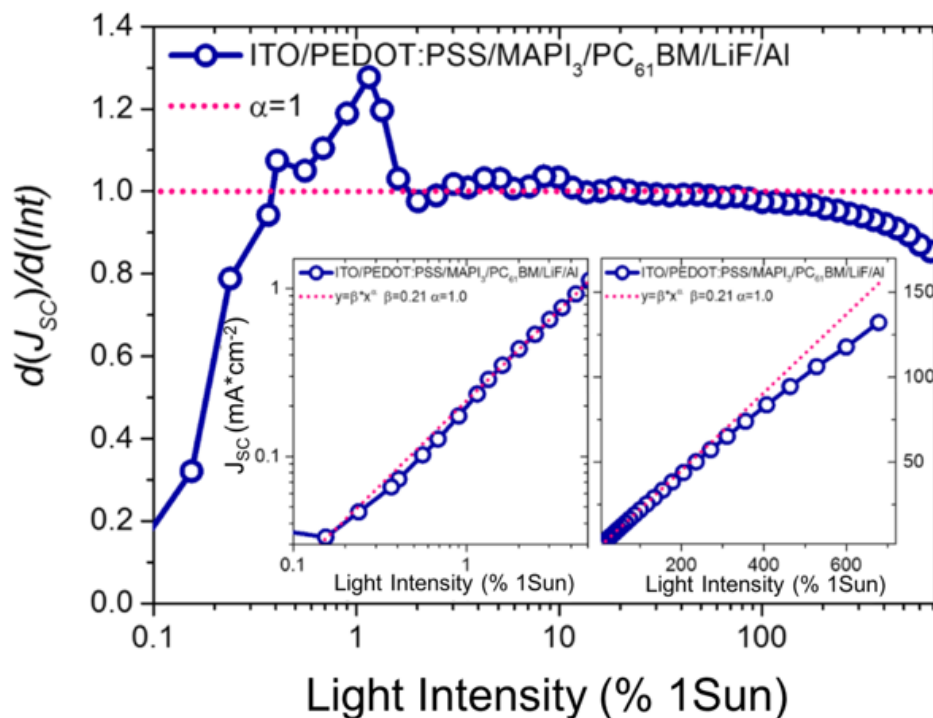### 3.5.4. Device current measurement

Figure 3.2 Linearity of J_{SC} versus excitation light intensity (Int) for an ITO/PEDOT:PSS/MAPI₃/PC₆₁BM/LiF/Al device, shown in the inserts as direct dependencies for low and high excitation densities as a function of light intensity, and as $d(J_{SC})/d(Int)$ versus Int in the main figure.

This section concludes with a brief discussion of the relevance of the data reported herein to the operation of complete devices under steady-state irradiation. The current study is limited to bilayers, and therefore cannot be directly compared to complete devices. However, at least qualitatively, photocurrent generation in analogous complete devices can be expected to show similar trends to those reported herein, with irreversible charge trapping limiting photocurrent generation at very low light fluxes, and bimolecular recombination limiting photocurrent generation at high light fluxes. Details of this behaviour will depend upon contact layer, $MAPI_3$ layer thickness and processing, device operating condition and field distribution, amongst other parameters. As an initial evaluation of this issue, Figure 3.16 presents a plot of $d(J_{SC})/d(Int)$ as a function of 1 light intensity (*Int*), where the J_{SC} is measured of a complete Glass/ITO/PEDOT:PSS/$MAPI_3$/$PC_{61}BM$/LiF/Al device. $d(J_{SC})/d(Int)$ values < 1 are a measure of the presence of non-linear losses limiting photocurrent generation.[29] It is striking that PLQE and $d(J_{SC})/d(Int)$ show rather analogous dependencies on light intensity (compare Figures 3.5b and 3.11b to Figure 3.16), indicating that the effects discussed on bilayers are directly relevant to complete device performance, with the intensity dependence of interfacial charge transfer impacting directly upon the intensity dependence of photocurrent generation. Currently more quantitative analysis of this issue is being undertaken, including direct measurements of transfer efficiencies in complete devices, to determine the detailed impact of these dependencies upon device performance. In particular, it should be noted that the study herein does not address the issue of whether charges transferred to the contact layers are efficiently extracted to the external circuit (not present in the bilayer samples studied herein) or undergo surface recombination losses, a key consideration for many $MAPI_3$ solar cells.

3.6. Conclusion

The results in this chapter indicate that different experimental assays of charge transfer efficiency in MAPI$_3$/PC$_{61}$BM and PEDOT:PSS/MAPI$_3$ films can yield very different results. These differences are linked to the excitation conditions employed in terms of excitation density and pulsed versus steady-state measurements. The results indicate that PLQE measurements in a typical PL spectrometer can yield significantly higher transfer efficiencies to those measured under 1 Sun irradiation. To ensure most relevance to device operation, it can be concluded that such steady-state PLQE measurements should be done using irradiation conditions similar to solar irradiation. It is apparent that typical TCSPC transient emission studies and ultrafast transient absorption studies yield transfer efficiencies very different from those observed under 1 Sun conditions due to the different excitation conditions typically employed in such studies. Electron and hole transfer times to PC$_{61}$BM and PEDOT:PSS are determined to be 36 and 11 ns respectively for the films studied. The slower transfer time for electrons results in a stronger dependence of transfer efficiency upon excitation conditions. From pulsed excitation measurements, it is found that excitation densities of $\sim 5 \times 10^{15}$ cm^{-3} are sufficient to reach the highest charge transfer efficiencies, indicating that the density of traps in MAPI$_3$ which compete directly with charge transfer is of this order of magnitude. At higher excitation conditions, accelerating bimolecular recombination is observed to reduce charge transfer efficiencies. The measured excitation density dependencies of charge transfer efficiency in these bilayers are shown to correlate, at least qualitatively, with the linearity of device photocurrent with light intensity, indicating the relevance of the charge carrier dependent transfer process in operational devices.

3.7. References

[1] a) J. H. Im, C. R. Lee, J. W. Lee, S. W. Park, N. G. Park, *Nanoscale.* **2011**, 3, 4088; b) S. D. Stranks, G. E. Eperon, G. Grancini, C. Menelaou, M. J. Alcocer, T. Leijtens, L. M. Herz, A. Petrozza, H. J. Snaith, *Science.* **2013**, 342, 341; c) G. Xing, N. Mathews, S. Sun, S. S. Lim, Y. M. Lam, M. Gratzel, S. Mhaisalkar, T. C. Sum, *Science.* **2013**, 342, 344; d) G. Xing, N. Mathews, S. S. Lim, N. Yantara, X. Liu, D. Sabba, M. Gratzel, S. Mhaisalkar, T. C. Sum, *Nature Materials.* **2014**, 13, 476; e) M. Cadelano, V. Sarritzu, N. Sestu, D. Marongiu, F. Chen, R. Piras, R. Corpino, C. M. Carbonaro, F. Quochi, M. Saba, A. Mura, G. Bongiovanni, *Advanced Optical Materials.* **2015**, 3, 1557.

[2] a) S. Draguta, S. Thakur, Y. V. Morozov, Y. Wang, J. S. Manser, P. V. Kamat, M. Kuno, *Journal of Physical Chemistry Letters.* **2016**, 7, 715; b) S. D. Stranks, V. M. Burlakov, T. Leijtens, J. M. Ball, A. Goriely, H. J. Snaith, *Physical Review Applied.* **2014**, 2; c) Z. Y. Zhang, H. Y. Wang, Y. X. Zhang, Y. W. Hao, C. Sun, Y. Zhang, B. R. Gao, Q. D. Chen, H. B. Sun, *Sci Rep.* **2016**, 6, 27286; d) J. Q. Grim, S. Christodoulou, F. Di Stasio, R. Krahne, R. Cingolani, L. Manna, I. Moreels, *Nature Nanotechnology.* **2014**, 9, 891; e) C. Wehrenfennig, G. E. Eperon, M. B. Johnston, H. J. Snaith, L. M. Herz, *Advanced Materials.* **2014**, 26, 1584; f) M. B. Johnston, L. M. Herz, *Acc Chem Res.* **2016**, 49, 146; g) R. L. Milot, G. E. Eperon, H. J. Snaith, M. B. Johnston, L. M. Herz, *Advanced Functional Materials.* **2015**, 25, 6218.

[3] a) Q. Shen, Y. Ogomi, J. Chang, S. Tsukamoto, K. Kukihara, T. Oshima, N. Osada, K. Yoshino, K. Katayama, T. Toyoda, S. Hayase, *Physical Chemistry Chemical Physics.* **2014**, 16, 19984; b) S. Makuta, M. Liu, M. Endo, H. Nishimura, A. Wakamiya, Y. Tachibana, *Chemical Communications.* **2016**, 52, 673; c) P. Piatkowski, B. Cohen, F. Javier Ramos, M. Di Nunzio, M. K. Nazeeruddin, M. Gratzel, S. Ahmad, A. Douhal, *Physical Chemistry Chemical Physics.* **2015**, 17, 14674; d) E. M. Hutter, J. J. Hofman, M. L. Petrus, M. Moes, R. D. Abellon, P. Docampo, T. J. Savenije, *Advanced Energy Materials.* **2017**, 7, 1602349.

[4] a) G. J. Hedley, A. J. Ward, A. Alekseev, C. T. Howells, E. R. Martins, L. A. Serrano, G. Cooke, A. Ruseckas, I. D. Samuel, *Nature Communications.* **2013**, 4, 2867; b) A. J. Ward, A. Ruseckas, M. M. Kareem, B. Ebenhoch, L. A. Serrano, M. Al-Eid, B. Fitzpatrick, V. M. Rotello, G. Cooke, I. D. Samuel, *Advanced Materials.* **2015**, 27, 2496; c) K. H. Lee, P. E. Schwenn, A. R. Smith, H. Cavaye, P. E. Shaw, M. James, K. B. Krueger, I. R. Gentle, P. Meredith, P. L. Burn, *Advanced Materials.* **2011**, 23, 766; d) J. Kim, I. Heo, D. Park, S. J. Ahn, S. Y. Jang, S. Yim, *Journal of Materials Chemistry A.* **2014**, 2, 10250; e) Z. Tan, J. Li, C. Zhang, Z. Li, Q. Hu, Z. Xiao, T. Kamiya, H. Hosono, G. Niu, E. Lifshitz, Y. Cheng, J. Tang, *Advanced Functional Materials.* **2018**, 28, 1801131; f) Y. Q. Luo, S. Aharon, M. Stuckelberger, E. Magana, B. Lai, M. I. Bertoni, L. Etgar, D. P. Fenning, *Advanced Functional Materials.* **2018**, 28, 1706995; g) F. Zhang, W. Shi, J. Luo, N. Pellet, C. Yi, X. Li, X. Zhao, T. J. S. Dennis, X. Li, S. Wang, Y. Xiao, S. M. Zakeeruddin, D. Bi, M. Gratzel, *Advanced Materials.* **2017**, 29; h) Y. Lin, L. Shen, J. Dai, Y. Deng, Y. Wu, Y. Bai, X. Zheng, J. Wang, Y. Fang, H. Wei, W. Ma, X. C. Zeng, X. Zhan, J. Huang, *Advanced Materials.* **2017**, 29; i) C. M. Wolff, F. Zu, A. Paulke, L. P. Toro, N. Koch, D. Neher, *Advanced Materials.* **2017**, 29; j) J. R. Zhang, D. L. Bai, Z. W. Jin, H. Bian, K. Wang, J. Sun, Q. Wang, S. Z. Liu, *Advanced Energy Materials.* **2018**, 8, 1703246; k) B. Krogmeier, F. Staub, D. Grabowski, U. Rau, T. Kirchartz, *Sustainable Energy & Fuels.* **2018**, 2, 1027; l) F. Staub, T. Kirchartz, K. Bittkau, U. Rau, *Journal of Physical Chemistry Letters.* **2017**, 8, 5084.

[5] a) D. S. Ginger, N. C. Greenham, *Phys Rev B.* **1999**, 59, 10622; b) K. Cnops, B. P. Rand, D. Cheyns, B. Verreet, M. A. Empl, P. Heremans, *Nat Commun.* **2014**, 5, 3406; c) D. M. Stoltzfus, J. E. Donaghey, A. Armin, P. E. Shaw, P. L. Burn, P. Meredith, *Chemical Reviews.* **2016**, 116, 12920.

[6] P. Docampo, J. M. Ball, M. Darwich, G. E. Eperon, H. J. Snaith, *Nature Communications.* **2013**, 4, 2761.

[7]   K. Tvingstedt, L. Gil-Escrig, C. Momblona, P. Rieder, D. Kiermasch, M. Sessolo, A. Baumann, H. J. Bolink, V. Dyakonov, *ACS Energy Letters.* **2017**, 2, 424.

[8]   a) J. You, L. Meng, T. B. Song, T. F. Guo, Y. M. Yang, W. H. Chang, Z. Hong, H. Chen, H. Zhou, Q. Chen, Y. Liu, N. De Marco, Y. Yang, *Nature Nanotechnology.* **2016**, 11, 75; b) H. T. Peng, W. H. Sun, Y. L. Li, W. B. Yan, P. R. Yu, H. P. Zhou, Z. Q. Bian, C. H. Huang, *Journal of Photonics for Energy.* **2016**, 6, 022002.

[9]   a) X. F. Deng, X. M. Wen, J. H. Zheng, T. Young, C. F. J. Lau, J. Kim, M. Green, S. J. Huang, A. Ho-Baillie, *Nano Energy.* **2018**, 46, 356; b) D. W. deQuilettes, W. Zhang, V. M. Burlakov, D. J. Graham, T. Leijtens, A. Osherov, V. Bulovic, H. J. Snaith, D. S. Ginger, S. D. Stranks, *Nature Communications.* **2016**, 7, 11683; c) X. Feng, H. Su, Y. Wu, H. Wu, J. Xie, X. Liu, J. Fan, J. Dai, Z. He, *J Mater Chem A.* **2017**, 5, 12048; d) D. W. deQuilettes, S. M. Vorpahl, S. D. Stranks, H. Nagaoka, G. E. Eperon, M. E. Ziffer, H. J. Snaith, D. S. Ginger, *Science.* **2015**, 348, 683; e) L. Zuo, H. Guo, D. W. deQuilettes, S. Jariwala, N. De Marco, S. Dong, R. DeBlock, D. S. Ginger, B. Dunn, M. Wang, Y. Yang, *Science Advances.* **2017**, 3, e1700106; f) T. Li, Y. Pan, Z. Wang, Y. Xia, Y. Chen, W. Huang, *J Mater Chem A.* **2017**, 5, 12602; g) A. R. Pascoe, S. Meyer, W. Huang, W. Li, I. Benesperi, N. W. Duffy, L. Spiccia, U. Bach, Y.-B. Cheng, *Advanced Functional Materials.* **2016**, 26, 1278.

[10]   a) H. Choi, C. K. Mai, H. B. Kim, J. Jeong, S. Song, G. C. Bazan, J. Y. Kim, A. J. Heeger, *Nature Communications.* **2015**, 6, 7348; b) K. C. Wang, J. Y. Jeng, P. S. Shen, Y. C. Chang, E. W. Diau, C. H. Tsai, T. Y. Chao, H. C. Hsu, P. Y. Lin, P. Chen, T. F. Guo, T. C. Wen, *Scientific Reports.* **2014**, 4, 4756; c) Y. Wu, X. Yang, W. Chen, Y. Yue, M. Cai, F. Xie, E. Bi, A. Islam, L. Han, *Nature Energy.* **2016**, 1, 16148; d) K. Gao, B. Xu, C. Hong, X. Shi, H. Liu, X. Li, L. Xie, A. K. Y. Jen, *Advanced Energy Materials.* **2018**, 8, 1800809; e) Y.-Q. Zhou, B.-S. Wu, G.-H. Lin, Z. Xing, S.-H. Li, L.-L. Deng, D.-C. Chen, D.-Q. Yun, S.-Y. Xie, *Advanced Energy Materials.* **2018**, 8,1800399; f) W. Chen, Y. Wu, J. Fan, A. B. Djurišić, F. Liu, H. W. Tam, A. Ng, C. Surya, W. K. Chan, D. Wang, Z.-B. He, *Advanced Energy Materials.* **2018**, 8, 1703519.

[11]   a) J. J. Chang, H. Zhu, B. C. Li, F. H. Isikgor, Y. Hao, Q. H. Xu, J. Y. Ouyang, *Journal of Materials Chemistry A.* **2016**, 4, 887; b) C. L. Chuang, C.-Y. Chen, C.-H. Chiang, C.-G. Wu, *Inorganic Chemistry Frontiers.* **2017**, 4, 850; c) A. Matas Adams, J. M. Marin-Beloqui, G. Stoica, E. Palomares, *J Mater Chem A.* **2015**, 3, 22154.

[12]   a) Q. F. Xue, M. Y. Liu, Z. C. Li, L. Yan, Z. C. Hu, J. W. Zhou, W. Q. Li, X. F. Jiang, B. M. Xu, F. Huang, Y. Li, H. L. Yip, Y. Cao, *Advanced Functional Materials.* **2018**, 28, 1707444; b) H. Dong, Z. X. Wu, J. Xi, X. B. Xu, L. J. Zuo, T. Lei, X. G. Zhao, L. J. Zhang, X. Hou, A. K. Y. Jen, *Advanced Functional Materials.* **2018**, 28, 1704836; c) A. N. Cho, N. G. Park, *ChemSusChem.* **2017**, 10, 3687; d) G. Y. Xu, R. M. Xue, W. J. Chen, J. W. Zhang, M. Y. Zhang, H. Y. Chen, C. H. Cui, H. K. Li, Y. W. Li, Y. F. Li, *Advanced Energy Materials.* **2018**, 8, 1703054; e) H. Hao, L. Wang, X. Ma, K. Cao, H. Yu, M. Wang, W. Gu, R. Zhu, M. S. Anwar, S. Chen, W. Huang, *Solar RRL.* **2018**, 2, 1800061.

[13]   a) T. Du, C. H. Burgess, J. Kim, J. Q. Zhang, J. R. Durrant, M. A. McLachlan, *Sustainable Energy & Fuels.* **2017**, 1, 119; b) D. Bryant, N. Aristidou, S. Pont, I. Sanchez-Molina, T. Chotchunangatchaval, S. Wheeler, J. R. Durrant, S. A. Haque, *Energy & Environmental Science.* **2016**, 9, 1655.

[14]   a) N. J. Jeon, J. H. Noh, Y. C. Kim, W. S. Yang, S. Ryu, S. I. Seok, *Nature Materials.* **2014**, 13, 897; b) N. G. Park, M. Gratzel, T. Miyasaka, K. Zhu, K. Emery, *Nature Energy.* **2016**, 1, 16152; c) Y. Z. Wu, A. Islam, X. D. Yang, C. J. Qin, J. Liu, K. Zhang, W. Q. Peng, L. Y. Han, *Energy & Environmental Science.* **2014**, 7, 2934.

[15]   a) O. Malinkiewicz, A. Yella, Y. H. Lee, G. M. Espallargas, M. Graetzel, M. K. Nazeeruddin, H. J. Bolink, *Nature Photonics.* **2013**, 8, 128; b) B. Xia, Z. X. Wu, H. Dong, J. Xi, W. Wu, T. Lei, K. Xi, F. Yuan, B. Jiao, L. X. Xiao, Q. H. Gong, X. Hou, *Journal of Materials Chemistry A.* **2016**, 4, 6295.

[16]   E. M. Talbert, H. F. Zarick, N. J. Orfield, W. Li, W. R. Erwin, Z. R. DeBra, K. R. Reid, C. P. McDonald, J. R. McBride, J. Valentine, S. J. Rosenthal, R. Bardhan, *Rsc Advances.* **2016**, 6, 86947.

[17]   a) F. Vietmeyer, P. A. Frantsuzov, B. Janko, M. Kuno, *Physical Review B.* **2011**, 83; b) M. Saba, M. Cadelano, D. Marongiu, F. Chen, V. Sarritzu, N. Sestu, C. Figus, M. Aresti, R. Piras,

A. G. Lehmann, C. Cannas, A. Musinu, F. Quochi, A. Mura, G. Bongiovanni, *Nat Commun.* **2014**, 5, 5049.

[18]   a) X. Wen, Y. Feng, S. Huang, F. Huang, Y.-B. Cheng, M. Green, A. Ho-Baillie, *Journal of Materials Chemistry C.* **2016**, 4, 793; b) Y. Yamada, T. Yamada, A. Shimazaki, A. Wakamiya, Y. Kanemitsu, *Journal of Physical Chemistry Letters.* **2016**, 7, 1972.

[19]   S. Wheeler, D. Bryant, J. Troughton, T. Kirchartz, T. Watson, J. Nelson, J. R. Durrant, *J Phys Chem C.* **2017**, 121, 13496.

[20]   M. Cadelano, M. Saba, N. Sestu, V. Sarritzu, D. Marongiu, F. Chen, R. Piras, F. Quochi, A. Mura, G. Bongiovanni, *Photoexcitations and Emission Processes in Organometal Trihalide Perovskites*, IntechOpen, **2016**.

[21]   a) V. sharma, S. Aharon, I. Gdor, C. Yang, L. Etgar, S. Ruhman, *J Mater Chem A.* **2016**, 4, 3546; b) J. M. Marin-Beloqui, J. P. Hernandez, E. Palomares, *Chemical Communications.* **2014**, 50, 14566; c) A. Marchioro, J. Teuscher, D. Friedrich, M. Kunst, R. van de Krol, T. Moehl, M. Gratzel, J. E. Moser, *Nature Photonics.* **2014**, 8, 250; d) H. S. Kim, C. R. Lee, J. H. Im, K. B. Lee, T. Moehl, A. Marchioro, S. J. Moon, R. Humphry-Baker, J. H. Yum, J. E. Moser, M. Gratzel, N. G. Park, *Sci Rep.* **2012**, 2, 591.

[22]   a) T. C. Sum, N. Mathews, G. Xing, S. S. Lim, W. K. Chong, D. Giovanni, H. A. Dewi, *Accounts of Chemical Research.* **2016**, 49, 294; b) J. S. Manser, P. V. Kamat, *Nature Photonics.* **2014**, 8, 737.

[23]   R. Godin, X. R. Ma, S. Gonzalez-Carrero, T. Du, X. E. Li, C. T. Lin, M. A. McLachlan, R. E. Galian, J. Perez-Prieto, J. R. Durrant, *Advanced Optical Materials.* **2018**, 6, 1701203.

[24]   T. C. Sum, N. Mathews, *Energy & Environmental Science.* **2014**, 7, 2518.

[25]   a) T. Zhao, W. Shi, J. Xi, D. Wang, Z. Shuai, *Scientific Reports.* **2016**, 7, 19968; b) Q. Dong, Y. Fang, Y. Shao, P. Mulligan, J. Qiu, L. Cao, J. Huang, *Science.* **2015**, 347, 967; c) Y. Chen, J. Peng, D. Su, X. Chen, Z. Liang, *ACS Applied Materials & Interfaces.* **2015**, 7, 4471; d) J. Peng, Y. Chen, K. Zheng, T. Pullerits, Z. Liang, *Chemical Society Reviews.* **2017**, 46, 5714.

[26]   a) T. Jiang, W. Fu, *Rsc Adv.* **2018**, 8, 5897; b) E. Bi, H. Chen, F. Xie, Y. Wu, W. Chen, Y. Su, A. Islam, M. Gratzel, X. Yang, L. Han, *Nature Communications.* **2017**, 8, 15330; c) J. C. Yu, J. A. Hong, E. D. Jung, D. B. Kim, S. M. Baek, S. Lee, S. Cho, S. S. Park, K. J. Choi, M. H. Song, *Scientific Reports.* **2018**, 8, 1070; d) C. Li, F. Wang, J. Xu, J. Yao, B. Zhang, C. Zhang, M. Xiao, S. Dai, Y. Li, Z. Tan, *Nanoscale.* **2015**, 7, 9771; e) W. Zhang, Y. Ding, Y. Jiang, M. Zheng, S. Wu, X. Lu, M. Zeng, X. Gao, Q. Wang, G. Zhou, J.-m. Liu, K. Kempa, J. Gao, *Rsc Adv.* **2017**, 7, 39523; f) F. H. Isikgor, B. Li, H. Zhu, Q. Xu, J. Ouyang, *J Mater Chem A.* **2016**, 4, 12543; g) C. Li, Y. Zhong, C. A. Luna, T. Unger, K. Deichsel, A. Graser, J. Kohler, A. Kohler, R. Hildner, S. Huettner, *Molecules.* **2016**, 21; h) Y. Li, L. Meng, Y. M. Yang, G. Xu, Z. Hong, Q. Chen, J. You, G. Li, Y. Yang, Y. Li, *Nature Communications.* **2016**, 7, 10214.

[27]   a) G. J. Nan, X. Zhang, M. Abdi-Jalebi, Z. Andaji-Garmaroudi, S. D. Stranks, G. Lu, D. Beljonne, *Advanced Energy Materials.* **2018**, 8, 1702754; b) F. Staub, H. Hempel, J. C. Hebig, J. Mock, U. W. Paetzold, U. Rau, T. Unold, T. Kirchartz, *Physical Review Applied.* **2016**, 6.

[28]   a) Y. Wang, X. Sun, Z. Chen, Y. Y. Sun, S. Zhang, T. M. Lu, E. Wertz, J. Shi, *Advanced Materials.* **2017**, 29; b) T. Du, J. Kim, J. Ngiam, S. Xu, P. R. Barnes, J. R. Durrant, M. McLachlan, *Advanced Functional Materials.* **2018**, 28, 1801808.

[29]   a) L. J. A. Koster, V. D. Mihailetchi, H. Xie, P. W. M. Blom, *Appl Phys Lett.* **2005**, 87, 203502; b) D. Fernandez, A. Viterisi, J. W. Ryan, F. Gispert-Guirado, S. Vidal, S. Filippone, N. Martin, E. Palomares, *Nanoscale.* **2014**, 6, 5871; c) J. Jimenez-Lopez, W. Cambarau, L. Cabau, E. Palomares, *Scientific Reports.* **2017**, 7, 6101; d) K. Wang, C. Yi, C. Liu, X. Hu, S. Chuang, X. Gong, *Scientific Reports.* **2015**, 5, 9265.
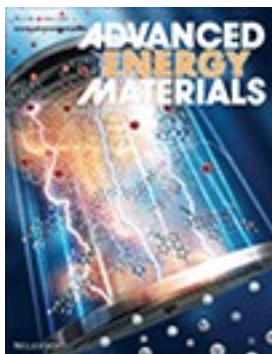
Thank you for your order!

Dear Mr. Jinhyun Kim,

Thank you for placing your order through Copyright Clearance Center's RightsLink®service.

Order Summary

Licensee:	Mr. Jinhyun Kim
Order Date:	Nov 26, 2018
Order Number:	4476310845861
Publication:	Advanced Energy Materials
Title:	Excitation Density Dependent Photoluminescence Quenching and Charge Transfer Efficiencies in Hybrid Perovskite/Organic Semiconductor Bilayers
Type of Use:	Dissertation/Thesis
Order Total:	0.00 GBP

View or print complete details of your order and the publisher's terms and conditions.

Sincerely,

Copyright Clearance Center

Chapter 4. Analyses of evolution of MAPI$_3$ photophysics following film storage

Contents

4.1. Abstract

In this chapter, the origin of the change of the PL of $MAPI_3$ perovskite films stored in nitrogen in the dark is explored. The PL of $MAPI_3$ films was monitored for a month, together with other optical measurements, including UV-vis spectroscopy, TAS and TCSPC. Crystallinity and morphology changes were investigated by XRD and AFM, respectively. Our results indicate that changes in PL intensity are caused by recrystallization processes correlated with reductions in trap state density. Consistent with the higher crystallinity and fewer defects in a $MAPI_3$ film aged for three weeks, the $MAPI_3$ device performance was found to be enhanced by 13% over the storage period, leading to a PCE of 19.6%.

4.2. Introduction

In chapter 3, the excitation density dependence of optical measurements, including PL, PLQE and charge transfer efficiency, which relate to device performance, were successfully explained, employing 'stabilised' MAPI$_3$ films aged for three weeks in nitrogen prior to optical analyses. As explained in chapter 1, the MAPI$_3$ perovskite structure has an extremely low formation energy from NH_3^+ I^- and PbI_4^{2-} via a solid-state reaction, proceeding without solvent at room temperature.[1] This property is a double-edged sword: although it allows formation of highly crystalline films via low-temperature solution-processing,[2] these films can be unstable, readily decomposing into PbI$_2$ and MAI.[3] Simple modifications of the crystal structure and morphology of such perovskite films can significantly change their electronic and optical properties,[4] and therefore the power conversion efficiency of the resultant photovoltaic devices.[5-8]

In 2014, Stranks et al. reported on optical instability issues related to perovskite films, especially concerning the PL.[9] According to a so-called 'curing' effect of perovskite films, the PL intensity has been reported to increase upon illumination for MAPIC (MAPbI$_{3-X}$Cl$_X$) perovskite films. Stranks proposed that photogenerated electrons and chemical reactions driven by light soaking change the ionic motion, stabilising the charge carrier trap states.[9a] It has been suggested that the evolution of PL intensity can be used as an indicator of trap densities, and bulk and surface recombination properties, including interplay between radiative and non-radiative recombination.[10] Measuring the evolution of PL intensity with various parameters is widely used to determine the properties of other photovoltaic materials.[11]

The effect of oxygen and/or light irradiation on the evolution of perovskite PL intensity has been intensively studied to determine the origin of its instability. Feng et al. (2016) proposed that trap sites associated with non-radiative charge recombination can be deactivated by oxygen or H_2O physisorption on the surface.[12] Therefore, the PL enhancement could be reversed by adjusting the excitation light (on or off) or switching the atmosphere between oxygen and nitrogen.[12-13] DeQuilettes et al. (2016) also reported the irradiation intensity dependence of PL enhancement with respect to oxygen and light.[14] Moreover, Tian et al. (2015) proposed a model in which a non-radiative trap state could be deactivated by oxygen in a photochemical reaction.[9b] In their study, for an excitation power density of $0.01-1$ W cm^{-2} in air, the PL intensity could be increased by three orders of magnitude. Time-resolved luminescence microscopy was employed to study light-induced PL enhancement produced by surface-deposited $MAPI_3$ perovskites, which increased the PL lifetime from several to several hundred nanoseconds.[9b] PL enhancement at depths exceeding 100 μm in single crystals has been interpreted as confirming the long-term stability of passivated oxygen species in the absence of light irradiation.[9b] However, according to a recent report by Feng et al. (2017), Tian's model of oxygen diffusion into crystal lattices may not be the main factor in PL enhancement, since the bond dissociation energy for O_2 can reach 5.15 eV without catalysts.[15] As the energy barrier for the reaction can be as low as 0.45 eV, O_2 tends to react with photoinduced free charge carriers in the crystal lattice.[15a, 16] A schematic of Feng's mechanism of PL enhancement in $MAPbI_3$ single crystals by light-soaking effects with and without oxygen is shown in Figure 4.1.[15a]
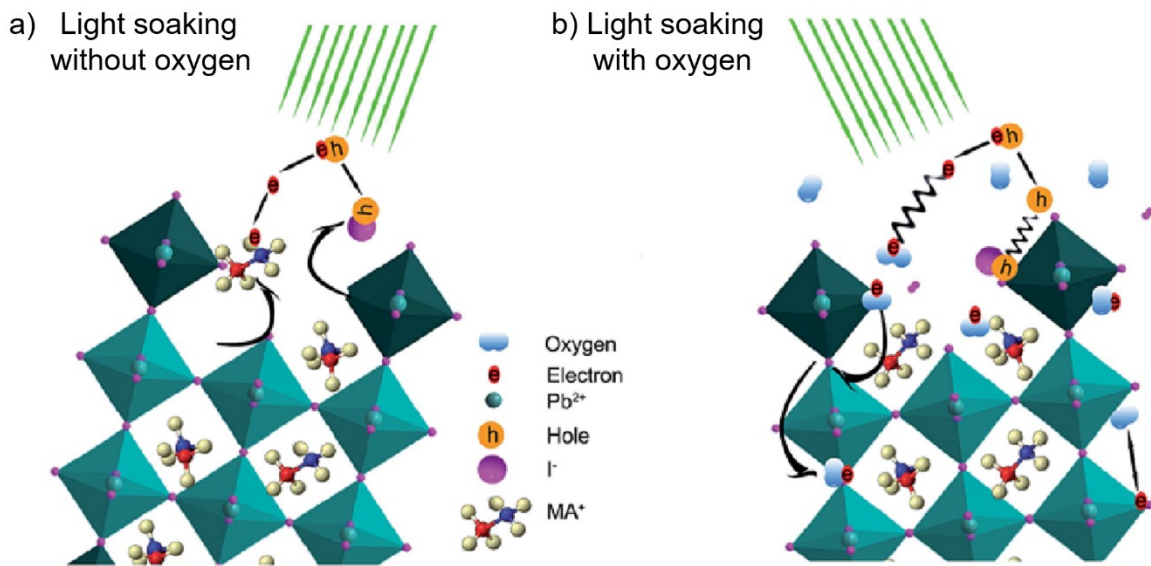
Figure 4.1 Schematic of the degradation mechanisms of MAPI₃ perovskite proposed in a) vacuum and b) in oxygen. (Figure source: J. Mater. Chem. A, 2017, 5, 12048–12053) [15a]

Under vacuum, as shown in Figure 4.1a, it is generally accepted that activation energies (E_A) ,associated with the rate of ion migration , for MAPI₃ single crystals can be as low as 0.1–0.9 eV,[17] thus a significant migration of ions and, the associated formation of defects, can be expected.[15a] Under steady-state conditions, accumulated photon-generated charge carriers can cause ion migration to form methylammonium ions (MA$^+$) and iodine vacancies (V_I^+), which may quench free carriers via 'ion activation'.[18] However, in an oxygen atmosphere, as shown in Figure 4.1b, photon-generated electrons could react with the oxygen to yield high energy O^{2-} superoxides that can be transformed into single oxygen atoms within the lattice.
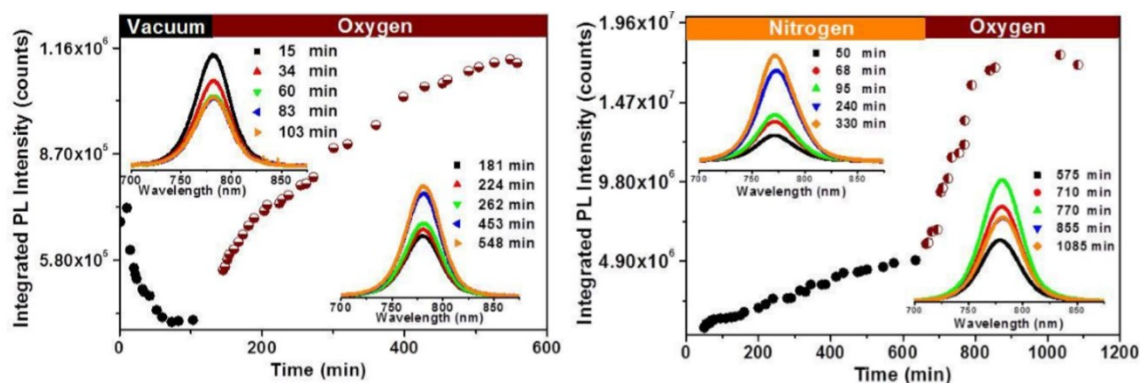
Figure 4.2 Transitions of integrated PL intensity as a function of light-soaking time from vacuum to oxygen and nitrogen to oxygen conditions. (Figure source: J. Mater. Chem. A, 2017, 5, 12048–12053, Supporting Information Figure S1c and d) [15a]

Furthermore, Feng et al. show that the PL of a MAPI$_3$ single crystal could be enhanced by nitrogen as well as oxygen environments[15a] (see Figure 4.2); however, the oxygen effect is much greater than that of nitrogen. They proposed that the PL enhancement in a nitrogen environment may be due to physical absorption (rather than reaction) on corresponding defects in the MAPbI$_3$ single crystals, causing a trap passivation effect, since the high reaction energy barrier for N$_2$ can reach 9.8–11.5 eV. Even in the absence of oxygen, light illumination has been shown to influence PL intensity.[15a] 'Self-curing' has also reported to occur in the dark after illumination. It has been suggested that the energy gained during illumination slowly decays in the dark, generating heat; using this released heat, perovskites can heal their defects, increasing the PL intensity.[19]

The complex and unstable properties of perovskite materials alter optical measurements, which may vary significantly depending on the materials used for the precursor solution and its processing as a film (including solvent, fabrication process, storage conditions and device structure). The sensitivity of PL to changes in the perovskite structure indicates that PL is a suitable probe for investigating changes in the perovskite film. However, to do this, further knowledge of the PL properties of MAPI$_3$ in an inert atmosphere is required, and how this may

evolve with time even in the absence of light. Thus, in this chapter of my thesis, I present a study on the origin of the PL intensity changes induced by storage in an inert atmosphere in the dark, probing the underlying structural and optical changes in perovskite films via UV-vis, tr-PL and TAS; crystallinity and surface morphology were also investigated by XRD and AFM.

4.3. Experimental methods

4.3.1. Sample preparation

4.3.1.1. MAPI$_3$ Perovskite layer

For this chapter, MAPI$_3$ films fabricated by the toluene and diethyl ether dripping methods, explained in chapter 3 and chapter 5 respectively, were used. Diethyl ether dripped MAPI$_3$ films were fabricated by Du Tian (Imperial College London).

4.3.2. Film characterization

XRD, UV-Vis spectroscopy, fs-TAS, TCSPC, ss-PL Spectroscopy were measured following the conditions described in chapter 2. For the spectroscopy, toluene dripped MAPI$_3$ was used. XRD was measured by Du Tian (Imperial College London).

4.3.2.1 AFM measurement

A commercial AFM (Multimode 8, Bruker) was employed with an n-doped silicon tip (radius <7 nm) (Nanosensors) in close contact (tapping) mode. AFM was measured by Dr Ching-Hong Tan (Imperial College London).

4.3.2.2. Device fabrication and performance measurement

ITO/PTAA/MAPI$_3$/PC$_{61}$BM/LiF/Ag device fabrication and measurement was carried out following the conditions described in chapter 5. Note that diethyl ether dripped MAPI$_3$ is used for device characterization. The devices were fabricated and JV characterisation was carried out by Du Tian (Imperial College London).

4.4. Results

4.4.1. PL and UV-vis evolution in nitrogen and in the dark

The samples were encapsulated directly after fabrication (as detailed below), then stored in a nitrogen-filled glove box (GB) in the dark at room temperature, with PL measurements being taken periodically for up to a month after fabrication. It is noteworthy that encapsulation is an important step in this study, as the PL of perovskite is extremely sensitive to sample preparation and measurement conditions, including oxygen, temperature and solvent. Thus, the samples was encapsulated using Surlyn film under the experimental conditions described in chapter 2, which are solvent free and low-temperature, as encapsulation at 80°C can avoid thermal and solvent-induced changes in unstable perovskite films.[2, 20] Secondly, we further sealed the edges with epoxy to minimise potential oxygen diffusion while measuring and storing samples. Additionally, steady state PL spectra were recorded rapidly employing low excitation fluence

(about 1.5 mW cm^{-2}) within about 30 seconds to minimise the exposure of the MAPI$_3$ film to light to avoid light-soaking and self-curing effects.
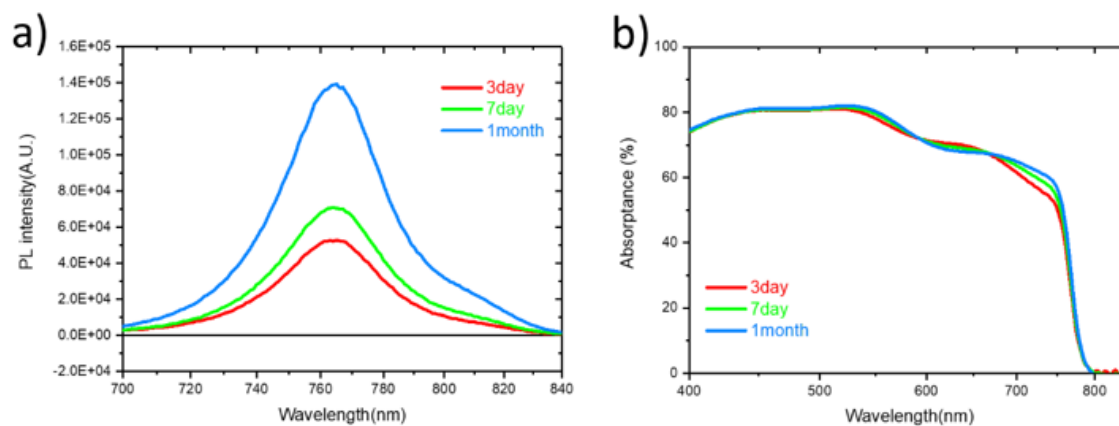

Figure 4.3 (a) PL and (b) absorptance spectra of MAPI$_3$ films measured 3, 7, and 30 days after fabrication. The films were sealed and stored in a glove box in the dark.

MAPI$_3$ samples may be expected to be stable in the absence of oxygen, water and light; however, the PL spectra displayed in Figure 4.3a indicate that the MAPI$_3$ films studied herein showed significant changes in PL intensity during storage in the dark. The MAPI$_3$ PL intensity increased spontaneously, even though the MAPI$_3$ samples were encapsulated and kept in an oxygen-free GB in the dark. Figure 4.3b presents the absorptance spectra of the same MAPI$_3$ film, which shows the usual strong absorptance in the visible range with an onset at 800 nm; however, the absorptance also changes with time, increasing around 750 and 520 nm, although much less significantly than the PL. It should be noted that while this trend of optical property changes was found to be qualitatively reproducible over many measurements, quantitatively the magnitude of the changes varied between films. Possible reasons for these quantitative variations between films are explored further below.
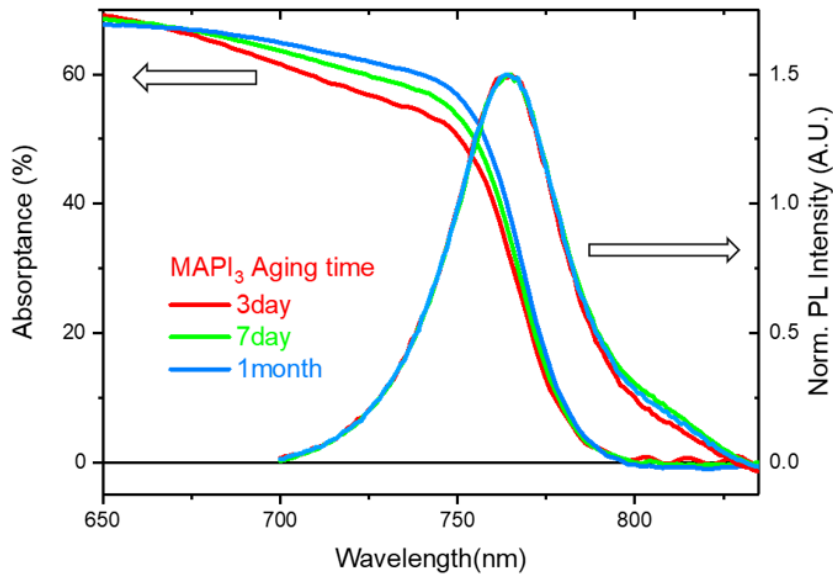
Figure 4.4 Normalised PL and absorptance spectra of MAPI₃ films recorded for different aging times in a glove box in the dark

Typically, for perovskite films, the peak of the PL spectrum is centred at the absorption onset because of its direct band gap structure, as discussed in chapter 1.[21] In Figure 4.4, the normalised PL and absorptance spectra are plotted together to analyse the shift in the peak position of the sample with storage time. The normalised PL values show the same peak position at 764 nm; however, the midpoint of the absorptance is at 768, 766 and 764 nm for the 3 day, 7 day and 1 month samples, respectively. The only differences in the shapes of the PL spectra are around 780 to 820 nm, where a weak PL shoulder increases in amplitude with storage time.
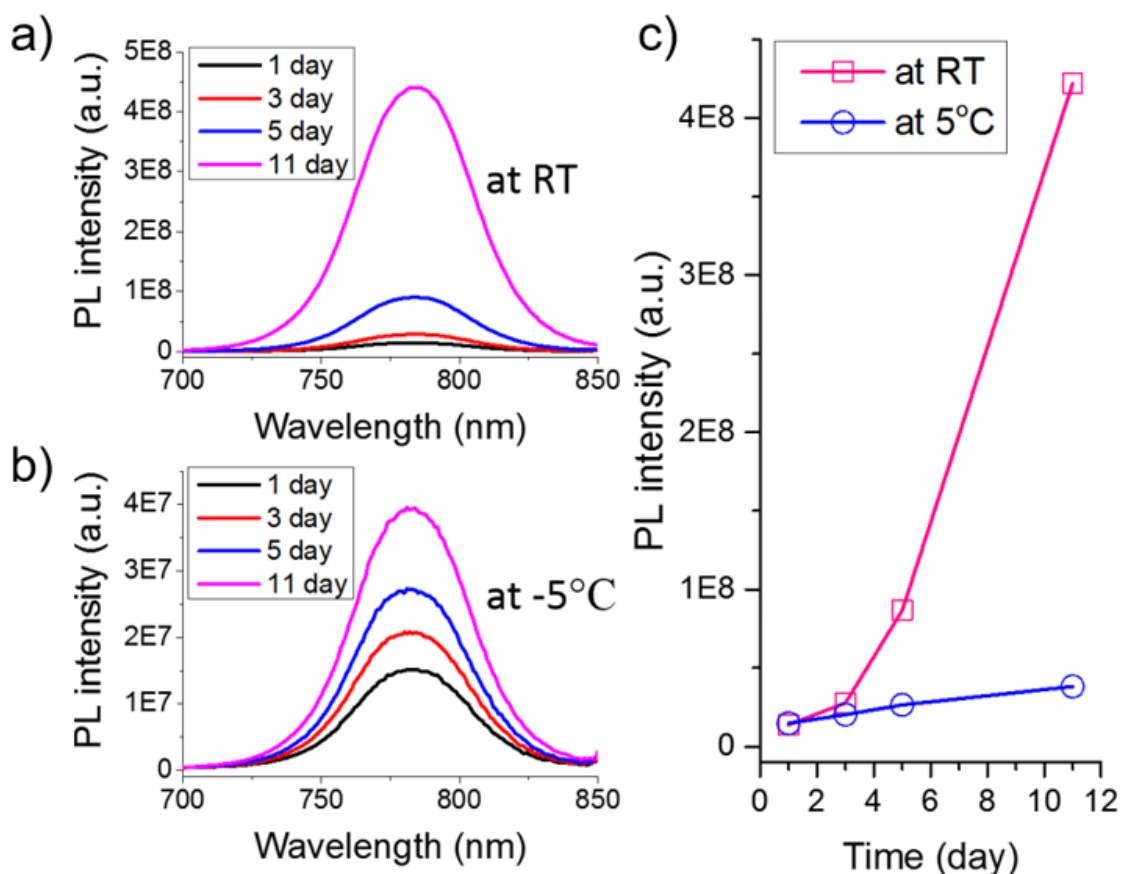
Figure 4.5 PL spectra of MAPI₃ films measured for various storage times at room temperature (a) and at −5 ℃ (b). (c) the PL peak intensity plotted as a function of ageing.

Figure 4.5 shows the change in PL intensity of encapsulated MAPI₃ films stored in the dark at room temperature and at −5°C. Figure 4.5b shows an increase in PL intensity at −5°C; however, the relative increase is much less than for the sample kept at room temperature. The PL peak intensity plots in Figure 4.5c shows a 24-fold increase in PL intensity over 10 days for the MAPI₃ film stored at room temperature, while that stored at −5°C shows only a two-fold increase in the intensity over the same period.
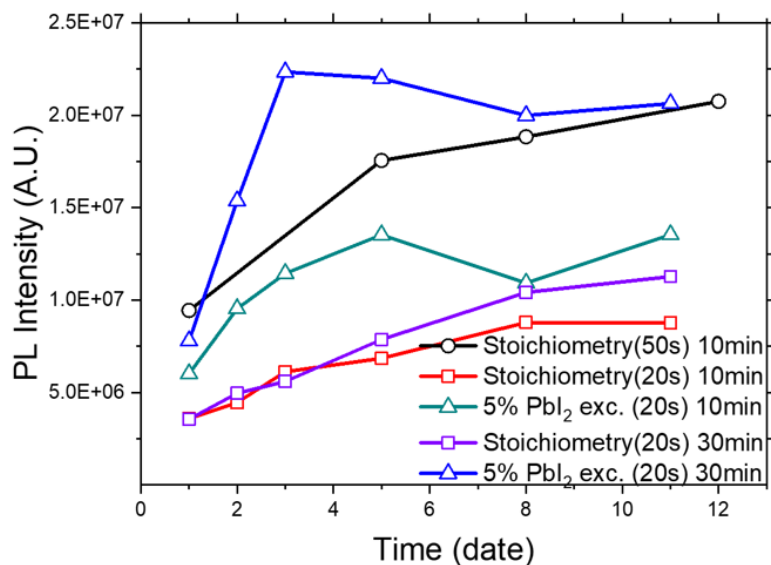
Figure 4.6 PL peak intensity as a function of ageing for MAPI$_3$ films produced by various fabrication conditions controlling the stoichiometry of the precursor solutions and their spin-coating time.

The PL evolution in Figure 4.5 shows different rates and saturation points depending on the fabrication conditions and chemical composition of the films. Figure 4.6 shows the PL intensity of toluene dripped MAPI$_3$ measured over 11 days. The black line shows MAPI$_3$ fabricated under the standard conditions detailed in chapter 3, with 1:1 stoichiometry and 50 s more spinning after toluene dripping, followed by 10 mins annealing at 100°C. When the additional spin time was changed from 50 s to 20 s, the initial and saturation intensities decreased but the rate barely changed. Interestingly, increasing the annealing time to 30 min resulted in a similar initial PL intensity; however, the saturation point at around the 11th day showed a higher intensity. MAPI$_3$ film with excess PbI$_2$ shows a rapid PL enhancement over 5 days, reaching a saturation point.

4.4.2. XRD crystallography of samples stored in nitrogen and in dark

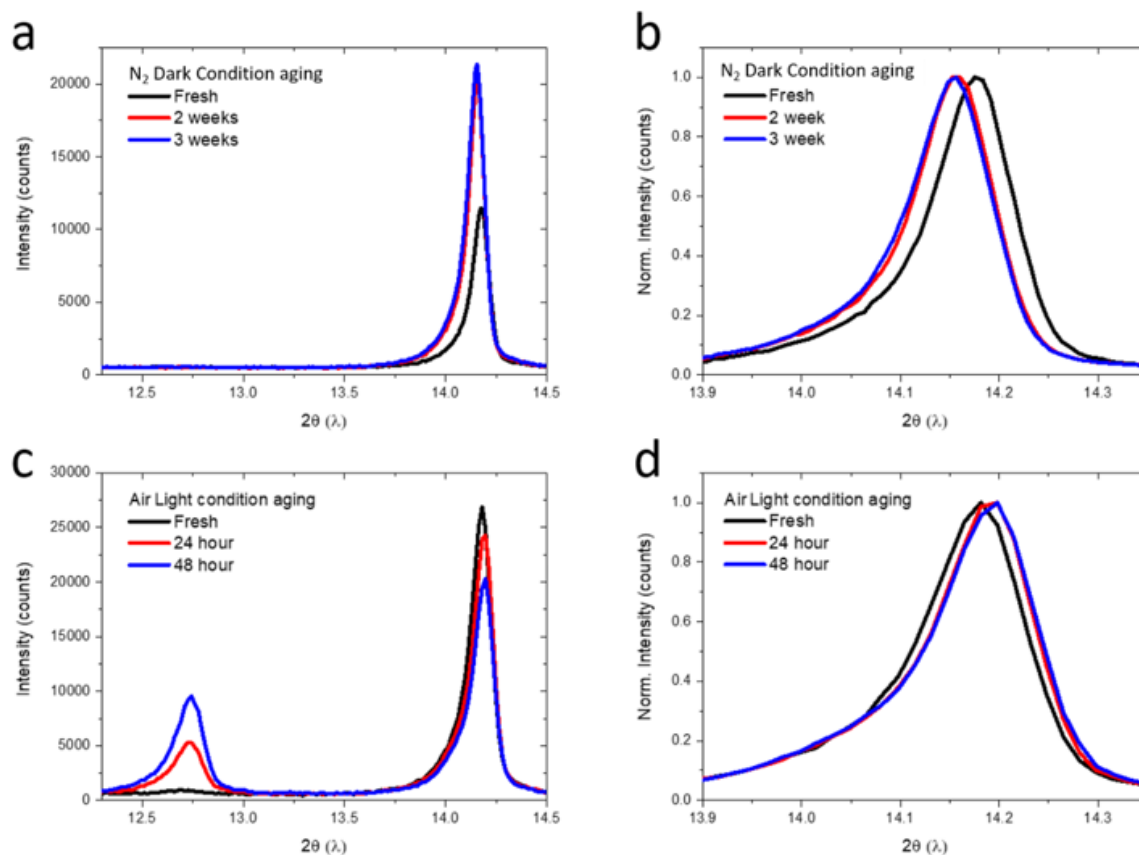*Figure 4.7 (a) XRD spectra of MAPI₃/PC₆₁BM films measured for various ageing times in a nitrogen-filled GB and (b) the normalised data. (c) XRD spectra of MAPI₃/PC₆₁BM films measured after various ageing times in air with light and (d) the normalised data.*

XRD measurements were performed to further investigate these changes in PL properties. Figure 4.7a shows XRD patterns of a fresh MAPI₃ film (black) and after storage in a dark GB for two (red) and three weeks (blue). The XRD peak at 14.1°, assigned to the (110) plane of MAPI₃,[11e, 22] shows a two-fold increase in the peak intensity and a peak position shift of approximately 0.03° to lower angles, suggesting continuous crystallisation of the film, even though samples were kept in an inert environment (see Figure 4.7a and 4.7b, normalised XRD). However, unlike the dark and oxygen effects, as shown in Figure 4.7c, the MAPI₃ film light-soaked in air exhibits an additional peak at 12.7°, which is assigned to the PbI₂ (001) secondary phase.[22b, 23] The intensity of the PbI₂ peak increases with soaking time accompanied by a

decrease in the MAPI$_3$ (110) peak. This trend is consistent with other studies.[23c] Note that the light-soaking time during which considerable PbI$_2$ forms is remarkably shorter than the ageing time in the GB. Also, as shown in Figure 4.7d, the normalised XRD pattern, contrary to GB ageing, shows the peak position shifting towards higher angles.
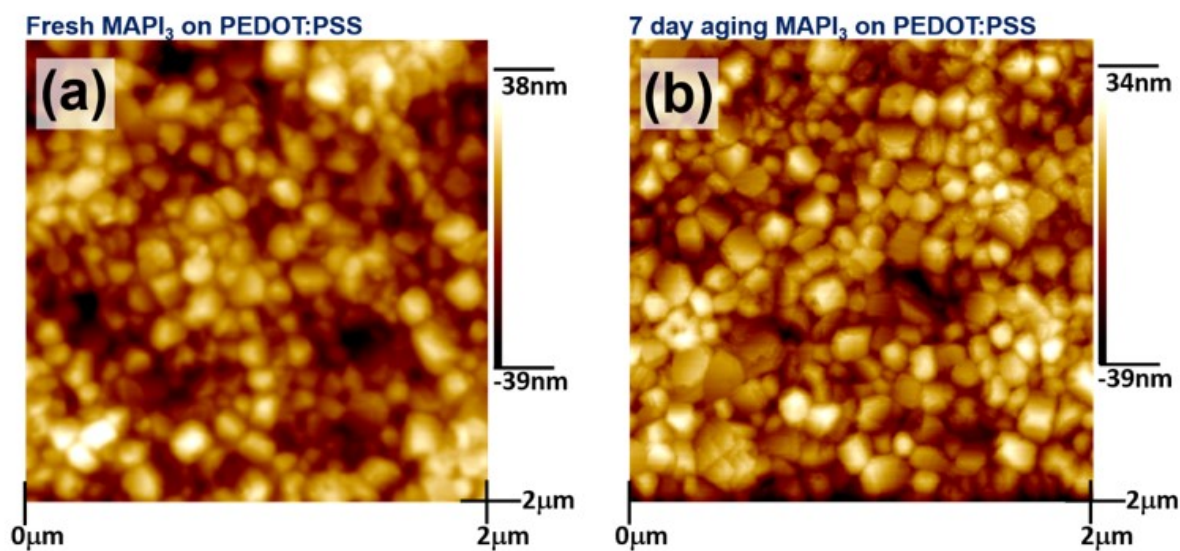

Figure 4.8 AFM images of fresh MAPI$_3$ on PEDOT:PSS/Glass substrate (a) and after 7 days ageing in the dark in a glove box (b)

The surface morphology of the MAPI$_3$ film was explored using AFM to correlate the PL and crystallinity changes. The images shown in Figure 4.8 show the same MAPI$_3$ film on a glass/PEDOT:PSS substrate stored in a GB for 1 day (Figure 4.8a) and 7 days (Figure 4.8b) after fabrication. For MAPI$_3$ on PEDOT:PSS stored for 1 day, the image shows a relatively flat perovskite surface.[24] For the same sample stored for 7 days in the GB, there is no visible difference compared with the image recorded after 1 day, indicating that the change in PL is related to microscopic crystallinity but not surface morphology.

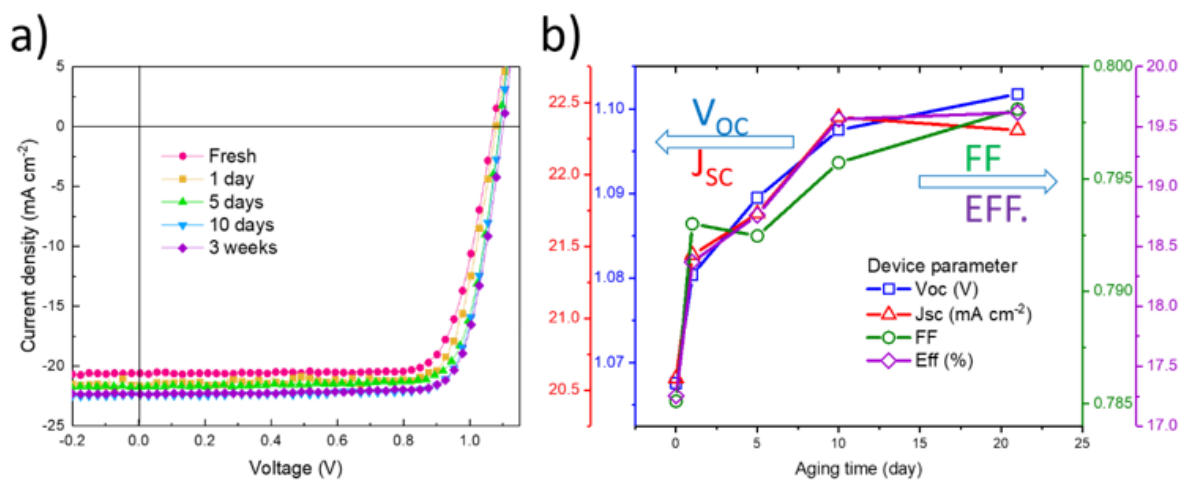### 4.4.3. Device performance enhancement by ageing

Figure 4.9 (a) IV curves of MAPI₃ perovskite solar cells produced with different ageing times and (b) the corresponding device performance parameters

Figure 4.9 shows the performance evolution of devices fabricated with MAPI$_3$ films aged in the dark in a glove box. ITO/PTAA/MAPI$_3$/PC$_{61}$BM/LiF/Ag structured devices show an efficiency of ~17.2% when fabricated from freshly deposited perovskite films, as shown in Figure 4.9a. The device performance is within the range of published figures for MAPI$_3$ devices with this structure. To evaluate the effect of film aging, ITO/PTAA/MAPI$_3$ films were kept in a GB in the dark with no PC$_{61}$BM top coat. The top-layer deposition of ETL and the electrode (PC$_{61}$BM/LiF/Au) were completed between 0 and 21 days later, after which the device performance was measured. Unexpectedly, there was an increase in efficiency with time to ~19.6% together with increases in the J$_{SC}$ and V$_{OC}$ and a slight increase in FF (see 4.9b), indicating a reduction in recombination losses in the device. Interestingly, changes in the parameters coincided with PL intensity changes.

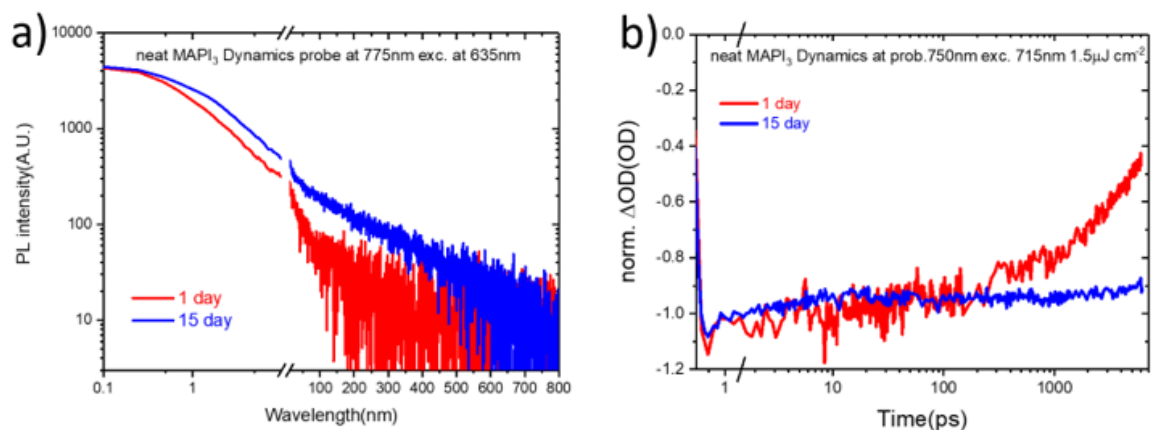### 4.4.4. Bulk charge carrier dynamics evolution of MAPI$_3$ perovskite

Figure 4.10 (a) tr-PL and (b) fs-TAS dynamics of MAPI₃ films measured after 1 and 15 day storage times.

To achieve a more detailed understanding of this enhancement in device performance with film aging, tr-PL and fs-TAS were measured with the same samples used for the reported in this chapter optical study. Figure 4.10a shows the tr-PL of MAPI$_3$ samples aged in a GB for different times in log-log and semi-log break plots for 0.1–10 and 11–800 ns, respectively. During ageing in a GB, the lifetime of the initial fast component continuously increases up to 15 days, which is likely due to trap passivation processes discussed in the introduction of this chapter. The slow component of the life time also increase by time which is consistent with ss-PL measurement in figure 4.3a. This phenomenon can also be observed in the fs-TAS decay probed at750 nm, which is a MAPI$_3$ perovskite photobleaching signal assigned to free charge carriers, as shown in Figure 4.10b. The charge carrier lifetime is only 7±0.1 ns when the sample is fresh (fitted assuming a single exponential decay), but this increases over time and finally saturates at > 100 ns at 15 days, consistent with the PL behaviour. Figure 4.11 shows the normalised fs-TAS spectra at 1 ps after charge carrier cooling in the visible range, with the peak shifting from 765 to 750 nm during the ageing time. This shift most probably results from

an evolution of the MAPI₃ density of states, and specifically to a decrease of density of tail
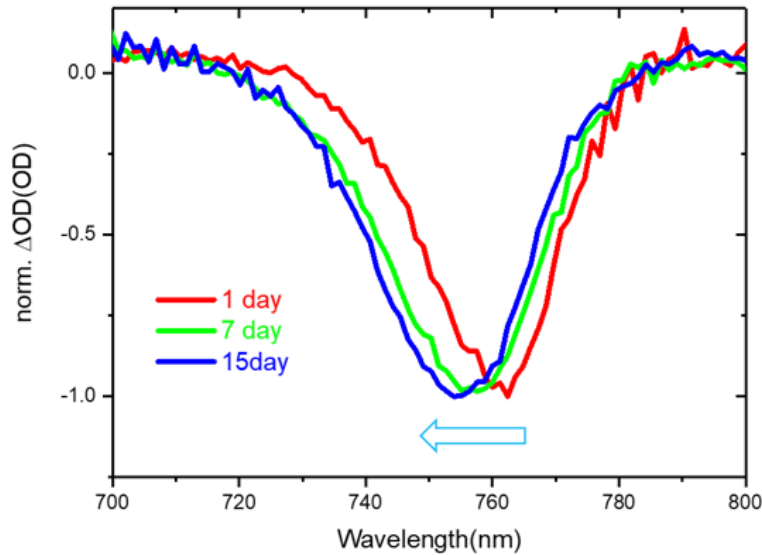
defect states during aging.[25]

Figure 4.11 fs-TAS spectra at 1 ps of MAPI₃ films measured after various storage times.

4.5. Discussion

Knowledge of the ageing process of MAPI₃ in the absence of air and light in relation to PL

evolution is essential for understanding the fundamental properties of perovskite materials, not

only because this effect leads to device performance changes but also because this process

affects most optical measurements. The spectroscopy tools described in chapter 3 are key to

determining the working mechanism of a photovoltaic device. However, most studies on PL

evolution involve light soaking with oxygen,[9b, 12-14, 19] which is far from the commercial

device encapsulated from the air. This study has focused on ageing in the dark in an inert

atmosphere, which is much less studied than oxygen ageing in the light. The study also aims

to clarify the need for specifying sample handling conditions to avoid reaching incorrect

conclusions. (For example, for how long should samples be stored after fabrication, and where?

At what temperature? When samples are measured, are they encapsulated? Are the samples exposed to air?)

The PL intensity measurements for MAPI$_3$ stored in dark and in GB reported in this chapter show similar PL evolution behaviour to that reported previously for the oxygen with or without light soaking effect reported previously, although with different rates.[9b, 12-14, 19] However, due to the absence of oxygen and water the aging process reported herein is different from the processes induced by light, water and oxygen. The oxygen light-soaking enhancement effect may be explained according to an oxygen and light degradation process which is suggested by Sun et al.[26] In their study, films with a higher defect density were degraded faster under oxygen and light. Counteracting this is surface state passivation by oxygen leading to an initial rise in PL as observed in our study but in the absence of oxygen. [26] Another possible reason for a rise in PL is the passivation of defects by PbI$_2$ formation. [27-28] In the current study, similar increase in PL was observed, but for samples stored in the dark and without oxygen, therefore, ruling out oxygen induced mechanisms. The XRD analysis shown in Figure 4.7 shows clearly there are significant differences between light soaking with oxygen and nitrogen in the dark. Our results obtained for samples aged in the dark in an inert atmosphere paint a different picture of the structural and optical evolution of MAPI$_3$ films. The increase in the peak intensity of the XRD patterns shown in Figure 4.7a indicates that the crystallinity of the MAPI$_3$ films is considerably enhanced by storing them in a dark inert atmosphere. The (110) peak position also shifts towards lower angles, suggesting an increased distance between lattice planes. Both observations indicate removal of amorphous parts of the polycrystalline perovskite film by ageing, which could be correlated with the filling of vacant sites in the lattice. This may result from incomplete conversion of precursors during the initial thermal annealing of as-deposited films. Figure 4.7c suggests that light soaking in the air shows a different trend

regarding the MAPI$_3$ (110) plain. In contrast with the dark GB ageing, Figure 4.7c highlights that exposure to air and light considerably degrades the perovskite film and leads to the appearance of the PbI$_2$ peak otherwise absent in the samples stored in dark and under nitrogen.[22d] These data highlight that, over time, the proportion of MAPI$_3$ crystalline phase spontaneously increases at room temperature. As mentioned earlier, the formation energy of MAPI$_3$ is low enough to allow rearrangement of the perovskite framework without additional energy. This process is affected by ambient conditions, including light, atmosphere and temperature. During ageing in a GB, solid-state reactions may occur in the perovskite crystals, including ion-exchange, topochemical reduction and dehydration, which can change the XRD patterns as well as the PL intensity.[29] It has been suggested these reactions change the crystal structure and/or remove defect sites in the perovskite film; thereby, the PL yield can be changed.[29a]

The results shown in Figure 4.5 as a function of temperature and storage time show that the PL intensity change decelerates at a lower temperature. This may indicate that the change in PL involves a chemical reaction in which non-radiative defect sites are reduced or passivated. MAPI$_3$ perovskite film fabricated by spin-coating have been suggested to form non-radiative trap states with a density of around 5×10^{16} cm^{-3} due to incomplete crystallisation.[29c] As discussed in chapter 3, the presence of such trap states can significantly reduce PL intensity. The ageing time in a GB without light may allow MAPI$_3$ crystals to form slowly via a solid-state reaction with thermal energy at room temperature, as indicated by the XRD data in figure 4.7,[29b] and then the non-radiative recombination rate associated with this trapping would decrease, increasing the PL intensity.

Unlike the observed PL changes, the absorptance of the perovskite films remain relatively constant with aging time. However, the shape of the spectra clearly change with time. As described in chapter 1, the mismatch between the PL peak wavelength and the midpoint of the onset of the absorption spectra of fresh samples might indicate the existence of a sub-band energy structure[30] (double conduction or valence band, or indirect band structure caused by methyl ammonium rotation). This gap in the $MAPI_3$ film probably reduces with time, resulting in sharpening of the band edge absorption, which is also consistent with the XRD results.

To investigate PL evolution during ageing in nitrogen in the dark, transient PL and absorptance measurements were performed. The TCSPC dynamics at low excitation fluence are limited by monomolecular recombination associated with trap states, so that the PL provides information about trap state properties.[9a, 31] The observed fast decay component corresponds to trapping of free charge carriers, while the long lifetime component corresponds to delayed emission from de-trapped charges. In Figure 4.10a, the samples kept in an inert atmosphere in the dark show an increased PL lifetime, indicating reduction of the trap state density in the film, consistent with the increased PL intensity and XRD results. However, further ageing reduces the charge carrier lifetimes. This effect is expected to similarly manifest in the fs-TAS, as we observe herein. The fs-TAS also shows bleach position shifts between samples measured at different ageing times, which are consistent with such a model of shallow trap state passivation due to crystallisation in the encapsulated films in the absence of oxygen, and the enhanced device performance.

4.6. Conclusion

This study demonstrates the PL evolution of $MAPI_3$ stored without oxygen in the dark. Our data shows that other optical properties, including UV-vis absorptance, TCSPC and fs-TAS,

change over time together with the PL. The XRD study highlights the differences between ageing in an inert atmosphere in the dark and oxygen and light-soaking effects, which both improve the PL intensity. The origin of PL enhancement is determined. The data suggests that aging in the dark under inert conditions reduces the number of non-radiative defect sites increasing the PL intensity. With this knowledge, the PL intensity could be correlated with the MAPI$_3$ perovskite device performance. Reducing the trap state density and improving the crystallinity of the MAPI$_3$ film causes the device performance factors, V_{OC}, J_{SC} and FF, to increase concurrently, and this growth trend matched the PL intensity changes. Thus, monitoring PL changes over a prolonged period provides information on both the optical properties and the device performance. Additionally, as with the preparation conditions, the sample storage conditions are critical with respect to the optical measurements and device performance.

4.7. References

[1]   a) A. M. Ganose, C. N. Savory, D. O. Scanlon, *Chemical Communications.* **2016**, 53, 20; b) Y.-Y. Zhang, S. Chen, P. Xu, H. Xiang, X.-G. Gong, A. Walsh, S.-H. Wei, *Chinese Physics Letters.* **2018**, 35.

[2]   a) J. You, Z. Hong, Y. M. Yang, Q. Chen, M. Cai, T. B. Song, C. C. Chen, S. Lu, Y. Liu, H. Zhou, Y. Yang, *ACS Nano.* **2014**, 8, 1674; b) G. Abdelmageed, C. Mackeen, K. Hellier, L. Jewell, L. Seymour, M. Tingwald, F. Bridges, J. Z. Zhang, S. Carter, *Solar Energy Materials and Solar Cells.* **2018**, 174, 566; c) C. Barone, F. Lang, C. Mauro, G. Landi, J. Rappich, N. H. Nickel, B. Rech, S. Pagano, H. C. Neitzert, *Scientific Reports.* **2016**, 6, 34675.

[3]   A. M. Ganose, C. N. Savory, D. O. Scanlon, *Journal of Physical Chemistry Letters.* **2015**, 6, 4594.

[4]   a) J. Burschka, N. Pellet, S. J. Moon, R. Humphry-Baker, P. Gao, M. K. Nazeeruddin, M. Gratzel, *Nature.* **2013**, 499, 316; b) J. H. Heo, S. H. Im, J. H. Noh, T. N. Mandal, C.-S. Lim, J. A. Chang, Y. H. Lee, H.-j. Kim, A. Sarkar, M. K. Nazeeruddin, M. Grätzel, S. I. Seok, *Nature Photonics.* **2013**, 7, 486.

[5]   a) A. D. McNaught, A. D. McNaught, *Compendium of chemical terminology*, Blackwell Science Oxford, **1997**; b) G. Hayes, B. Deveaud, *PHYSICA STATUS SOLIDI A APPLIED RESEARCH.* **2002**, 190, 637; c) A. Furube, T. Shiozawa, A. Ishikawa, A. Wada, K. Domen, C. Hirose, *The Journal of Physical Chemistry B.* **2002**, 106, 3065.

[6]   a) Y. Xu, T. Gong, J. N. Munday, *Scientific Reports.* **2015**, 5, 13536; b) G. Segev, Y. Rosenwaks, A. Kribus, *Solar Energy Materials and Solar Cells.* **2015**, 140, 464; c) S. M. Menke, N. A. Ran, G. C. Bazan, R. H. Friend, *Joule.* **2018**, 2, 25.

[7]   a) M. Y. Han, B. Ozyilmaz, Y. Zhang, P. Kim, *Physical Review Letters.* **2007**, 98, 206805; b) A. Luque, A. Martí, *Physical Review Letters.* **1997**, 78, 5014.

[8]   a) T. Trupke, M. A. Green, P. Würfel, *J Appl Phys.* **2002**, 92, 4117.

[9]   a) S. D. Stranks, V. M. Burlakov, T. Leijtens, J. M. Ball, A. Goriely, H. J. Snaith, *Phys Rev Appl.* **2014**, 2; b) Y. Tian, M. Peter, E. Unger, M. Abdellah, K. Zheng, T. Pullerits, A. Yartsev, V. Sundstrom, I. G. Scheblykin, *Physical Chemistry Chemical Physics.* **2015**, 17, 24978.

[10]   a) E. Gaubas, V. Borschak, I. Brytavskyi, T. Heponis, D. Dobrovolskas, S. Juršėnas, J. Kusakovskij, V. Smyntyna, G. Tamulaitis, A. Tekorius, *Advances in Condensed Matter Physics.* **2013**, 2013; b) L. Höglund, D. Z. Ting, A. Khoshakhlagh, A. Soibel, C. J. Hill, A. Fisher, S. Keo, S. D. Gunapala, *Appl Phys Lett.* **2013**, 103; c) H. Zhang, X. Ren, X. Chen, J. Mao, J. Cheng, Y. Zhao, Y. Liu, J. Milic, W.-J. Yin, M. Grätzelc, W. C. H. Choy, *Energy & Environmental Science.* **2018**, 11, 2253.

[11]   a) J. Kim, I. Heo, D. Park, S. J. Ahn, S.-Y. Jang, S. Yim, *J Mater Chem A.* **2014**, 2, 10250; b) F. Jin, Z. Su, B. Chu, P. Cheng, J. Wang, H. Zhao, Y. Gao, X. Yan, W. Li, *Scientific Reports.* **2016**, 6, 26262; c) W.-J. Ho, S.-K. Feng, J.-J. Liu, Y.-C. Yang, C.-H. Ho, *Applied Surface Science.* **2018**, 439, 868; d) V. Svrcek, T. Yamanari, D. Mariotti, S. Mitra, T. Velusamy, K. Matsubara, *Nanoscale.* **2015**, 7, 11566; e) T. Du, J. Kim, J. Ngiam, S. Xu, P. R. F. Barnes, J. R. Durrant, M. A. McLachlan, *Advanced Functional Materials.* **2018**, 28.

[12]   H. H. Fang, S. Adjokatse, H. Wei, J. Yang, G. R. Blake, J. Huang, J. Even, M. A. Loi, *Science Advances.* **2016**, 2, e1600534.

[13]   J. F. Galisteo-Lopez, M. Anaya, M. E. Calvo, H. Miguez, *Journal of Physical Chemistry Letters.* **2015**, 6, 2200.

[14]   D. W. deQuilettes, W. Zhang, V. M. Burlakov, D. J. Graham, T. Leijtens, A. Osherov, V. Bulovic, H. J. Snaith, D. S. Ginger, S. D. Stranks, *Nature Communications.* **2016**, 7, 11683.

[15]   a) X. Feng, H. Su, Y. Wu, H. Wu, J. Xie, X. Liu, J. Fan, J. Dai, Z. He, *J Mater Chem A.* **2017**, 5, 12048; b) I. Pelant, J. Valenta, *Luminescence Spectroscopy of Semiconductors*, Oxford University Press, Oxford, **2012**.

[16]   K. M. Ervin, I. Anusiewicz, P. Skurski, J. Simons, W. C. Lineberger, *The Journal of Physical Chemistry A.* **2003**, 107, 8521.

[17]   a) Y. Yuan, J. Huang, *Accounts of Chemical Research.* **2016**, 49, 286; b) Y.-F. Chen, Y.-T. Tsai, D. M. Bassani, L. Hirsch, *Appl Phys Lett.* **2016**, 109.

[18]   a) S. Chen, X. Wen, S. Huang, F. Huang, Y.-B. Cheng, M. Green, A. Ho-Baillie, *Solar RRL.* **2017**, 1; b) D. Yang, W. Ming, H. Shi, L. Zhang, M.-H. Du, *Chem Mater.* **2016**, 28, 4349.

[19]   W. Nie, J. C. Blancon, A. J. Neukirch, K. Appavoo, H. Tsai, M. Chhowalla, M. A. Alam, M. Y. Sfeir, C. Katan, J. Even, S. Tretiak, J. J. Crochet, G. Gupta, A. D. Mohite, *Nature Communications.* **2016**, 7, 11574.

[20]   J. C. Hamill, J. Schwartz, Y.-L. Loo, *ACS Energy Letters.* **2017**, 3, 92.

[21]   a) J. L. Knutson, J. D. Martin, D. B. Mitzi, *Inorganic Chemistry.* **2005**, 44, 4699; b) C. Wehrenfennig, M. Liu, H. J. Snaith, M. B. Johnston, L. M. Herz, *Journal of Physical Chemistry Letters.* **2014**, 5, 1300.

[22]   a) M. Bouchard, J. Hilhorst, S. Pouget, F. Alam, M. Mendez, D. Djurado, D. Aldakov, T. Schülli, P. Reiss, *The Journal of Physical Chemistry C.* **2017**, 121, 7596; b) A. M. A. Leguy, Y. Hu, M. Campoy-Quiles, M. I. Alonso, O. J. Weber, P. Azarhoosh, M. van Schilfgaarde, M. T. Weller, T. Bein, J. Nelson, P. Docampo, P. R. F. Barnes, *Chem Mater.* **2015**, 27, 3397; c) C. M. M. Soe, W. Nie, C. C. Stoumpos, H. Tsai, J.-C. Blancon, F. Liu, J. Even, T. J. Marks, A. D. Mohite, M. G. Kanatzidis, *Advanced Energy Materials.* **2018**, 8; d) T. Du, C. H. Burgess, J. Kim, J. Zhang, J. R. Durrant, M. A. McLachlan, *Sustain Energ Fuels.* **2017**, 1, 119.

[23]   a) Q.-D. Dao, A. Fujii, R. Tsuji, Y. Takeoka, M. Ozaki, *Organic Electronics.* **2017**, 43, 156; b) S. N. Habisreutinger, T. Leijtens, G. E. Eperon, S. D. Stranks, R. J. Nicholas, H. J. Snaith, *Nano Letters.* **2014**, 14, 5561; c) C. Qin, T. Matsushima, T. Fujihara, W. J. Potscavage, Jr., C. Adachi, *Advanced Materials.* **2016**, 28, 466.

[24]   a) J. H. Im, I. H. Jang, N. Pellet, M. Gratzel, N. G. Park, *Nature Nanotechnology.* **2014**, 9, 927; b) S. Paek, N. Cho, H. Choi, H. Jeong, J. S. Lim, J.-Y. Hwang, J. K. Lee, J. Ko, *The Journal of Physical Chemistry C.* **2014**, 118, 25899; c) N. J. Jeon, J. H. Noh, Y. C. Kim, W. S. Yang, S. Ryu, S. I. Seok, *Nature Materials.* **2014**, 13, 897.

[25]   a) C. L. Davies, M. R. Filip, J. B. Patel, T. W. Crothers, C. Verdi, A. D. Wright, R. L. Milot, F. Giustino, M. B. Johnston, L. M. Herz, *Nature Communications.* **2018**, 9, 293; b) S. Brittman, G. W. P. Adhyaksa, E. C. Garnett, *MRS Communications.* **2015**, 5, 7; c) J. A. Carr, S. Chaudhary, *Energy & Environmental Science.* **2013**, 6, 3414; d) X. Lin, G. E. Purdum, Y. Zhang, S. Barlow, S. R. Marder, Y.-L. Loo, A. Kahn, *Chem Mater.* **2016**, 28, 2677; e) Y. Yang, D. P. Ostrowski, R. M. France, K. Zhu, J. van de Lagemaat, J. M. Luther, M. C. Beard, *Nature Photonics.* **2015**, 10, 53; f) M. Malinauskas, P. Danilevicius, S. Juodkazis, *Optics Express.* **2011**, 19, 5602.

[26]   Q. Sun, P. Fassl, D. Becker-Koch, A. Bausch, B. Rivkin, S. Bai, P. E. Hopkinson, H. J. Snaith, Y. Vaynzof, *Advanced Energy Materials.* **2017**, 7.

[27]   Q. Chen, H. Zhou, T. B. Song, S. Luo, Z. Hong, H. S. Duan, L. Dou, Y. Liu, Y. Yang, *Nano Letters.* **2014**, 14, 4158.

[28]   T. S. Sherkar, C. Momblona, L. Gil-Escrig, J. Avila, M. Sessolo, H. J. Bolink, L. J. A. Koster, *ACS Energy Letters.* **2017**, 2, 1214.

[29]   a) R. E. Schaak, T. E. Mallouk, *Chem Mater.* **2002**, 14, 1455; b) A. Ummadisingu, M. Gratzel, *Science Advances.* **2018**, 4, e1701402; c) X. Wen, Y. Feng, S. Huang, F. Huang, Y.-B. Cheng, M. Green, A. Ho-Baillie, *Journal of Materials Chemistry C.* **2016**, 4, 793.

[30]   a) C. Motta, F. El-Mellouhi, S. Kais, N. Tabet, F. Alharbi, S. Sanvito, *Nature Communications.* **2015**, 6, 7026; b) J. S. Manser, P. V. Kamat, *Nature Photonics.* **2014**, 8, 737; c) K. G. Stamplecoskie, J. S. Manser, P. V. Kamat, *Energy & Environmental Science.* **2015**, 8, 208.

[31]   Y. Yamada, T. Nakamura, M. Endo, A. Wakamiya, Y. Kanemitsu, *Journal of the American Chemical Society.* **2014**, 136, 11610.

Chapter 5. Excited state dynamics of perovskite / organic bulk hetero-junction integrated devices.

Contents

5.1. Abstract

In this chapter, the carrier dynamics in integrated perovskite / organic bulk-heterojunction photovoltaic device are characterised using TAS. In this study fs-TAS is analysed with bi- and multi-layer samples, as well as full devices in short circuit (SC) conditions. Our results demonstrate that the measurement of full devices at SC conditions show a different charge-carrier transfer behaviour to films alone. The work presented here was conducted in collaboration with Dr. Hongkyu Kang of Gwangju Institute of Science and Technology, South Korea. (GIST)

5.2. Introduction

Photovoltaic cells integrating organic and inorganic perovskite semiconducting materials are a promising photovoltaic technology under active research and development.[1] With a bandgap of 1.6eV, MAPI$_3$-based devices can produce remarkable performance, which has come close to theoretical efficiency limits. The PV industry and relevant researchers are now expanding their efforts into perovskite tandem devices to extend light harvesting to >850nm.[2] Tin-halide-based perovskites have been developed to extend light harvesting up to 1000 nm, but this has been done via bandgap reduction and increased defects, causing an undesirably small V_{OC}.[1a, 3] Further drawbacks include very low stability, even compared to MAPI$_3$ devices, and PCE which are not competitive.[3b, 4] An alternative strategy is integrated perovskite/organic bulk heterojunction (BHJ) solar cells, which have shown a potential to approach higher device performance, without a V_{OC} loss, whilst increasing J_{SC}.[5] Such devices employ an organic BHJ effectively to sensitise the perovskite layer, enhance near IR photoactivity, and thus differ from conventional series connected tandem solar cells which employ a recombination layer between two separate light absorbing and voltage generating devices. To-date, MAPI$_X$Cl$_{3-X}$ perovskite films have been combined with PDTP-DFBT:PC$_{61}$BM 1:2 weight percent organic photovoltaic (OPV) blend in an inverted structure capable of 15.8% PCE, which was improved from 14.2% for the perovskite device alone. The improvement was mainly due to the increase of J_{SC}. The external quantum efficiency (EQE) indicates that additional light absorption of the OPV layer over 800 nm contributes to this improvement. Dong at el. provided data suggesting that quasi-Fermi level pinning is the physical source of the V_{OC} in integrated devices.[6] In this model, the V_{OC} is determined by quasi-Fermi level splitting of the double absorber system, which is dominated (or fixed) by the perovskite cell, rather than the OPV cell. However, the detailed function of these integrated perovskite/BHJ solar cells, which provide a higher V_{OC} from the

perovskite layer whilst photocurrent generation from both the perovskite and organic devices, remains poorly understood. The possibility to create such integrated devices without losing either V_{OC} or J_{SC} raises questions about the nature of electron and hole dynamics between perovskite and OPV structures. Here, it will be presented a study of the excited state and carrier recombination dynamics of perovskites/OPV integrated cells focused mostly on using fs-TAS.

5.3. Experimental detail

5.3.1. Sample preparation

For this chapter 5, MAI was purchased from Greatcell solar, and PbI_2 was purchased from Alfa Aesar. All solvent was purchased from Sigma-Aldrich. Poly(triaryl amine) (PTAA), Poly [(9,9-bis(3'-(N,N-dimethylamino)propyl)-2,7-fluorene)-alt-2,7-(9,9–dioctylfluorene)] (PFN), $PC_{61}BM$ and low band gap polymer DT-PDPP2T-TT (TT) were purchased from One materials.

5.3.1.1. Film and device fabrication

ITO were cleaned with a detergent, DI water, acetone and IPA in this sequence. PTAA (2mg/ml in toluene) was spin-coated on ITO at 3000 rpm for 30 seconds. To resolve the wetting issue of perovskite solution on PTAA, PFN (0.05 wt% in methanol) was spin-coated on PTAA to modify surface wettability. The perovskite solution was prepared by dissolving 1.5M MAI and PbI_2 in DMF/DMSO (9:1.1) mix and then deposited onto substrates and spin-coated at 4000 rpm for 30 seconds. At the 7th second of this spin-coating step, 400 µL diethyl ether was dripped to form a transparent intermediate phase. The substrate was then annealed at 100°C for 10 min. The organic polymer solution (TT:$PC_{61}BM$:N2200 = 4 mg:12 mg:1mg mL^{-1} in chloroform)

was spin coated onto the perovskite substrates at 1500 rpm for 30 second. At last, 100 nm Ag was evaporated on top of the stack as an electrode. For the devices analysed with TAS, a 20 nm thick Ag layer was deposited as an electrode to provide enough transparency for the accurate measurement of absorption.

5.3.2. Characterization

5.3.2.1. Device characterization

The J-V characteristic of devices (active area=4.64 mm^2) were scanned between 1.2V to –0.5V in both reverse and forward directions in N$_2$ filled glove box under AM 1.5G solar simulator calibrated with certified silicon solar cell from the National Renewable Energy Laboratory. The EQE spectra were obtained by an IPCE system (PV Measurements, Inc.). The measurement scans were from 300 nm to 1000 nm range with the chopping frequency of 100 Hz. In this study, the film and devices were fabricated with J-V and EQE characterization by Chieh Ting Lin (Imperial College London), Dr. Hongkyu Kang (GIST), and Dr. Jinho Lee (GIST)

5.3.2.2. Spectroscopy

All Uv-Vis spectroscopy and fs-TAS measurements were carried out as described in chapter 2.
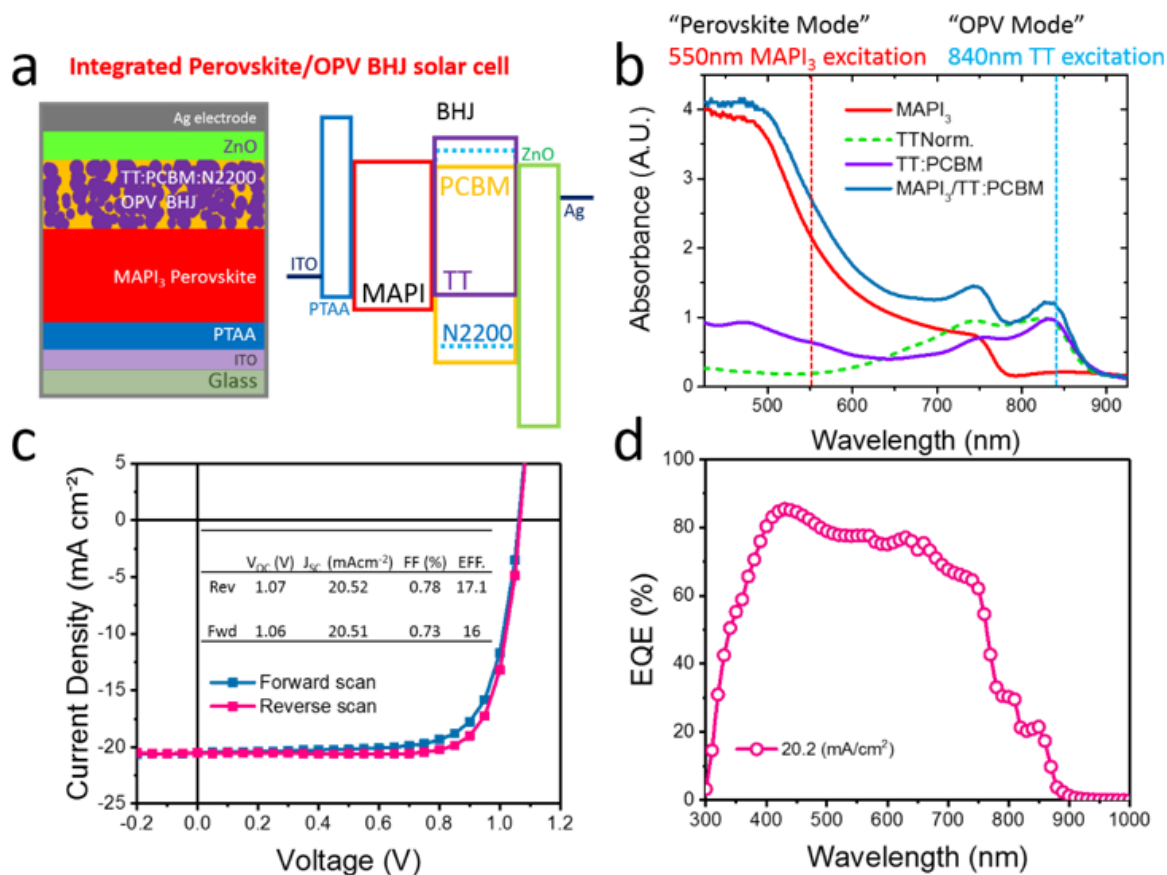
5.4. Results

Figure 5.1 (a) Schematic of the perovskite-organic integrated solar cell structure and energy level diagram used in this study; (b) absorption spectra of MAPI₃ (red line), TT (blue dot line), TT:PC₆₁BM (purple line), and MAPI₃/TT:PC₆₁BM (dark cyan line) films; (c)J-V of the perovskite integrated solar cell and (d) external quantum efficiency (EQE).

Figure 5.1a shows the integrated device structure using $MAPI_3$ and TT light-absorbers and a conduction and valence band energy level diagram based on literature data.[5b, 6b, 7] The structure is similar to the p-i-n inverted perovskite device structure, adding a $TT:PC_{61}BM:N2200$ blended layer instead of a phenyl-C_{61}-butyric acid methyl ester ($PC_{61}BM$) electron transport layer. PTAA is the hole transport layer, which has previously been shown to exhibit a high efficiency with $MAPI_3$ devices.[8] Zinc oxide (ZnO) is the electron-transfer and hole-blocking layer. In the integrated cells, $MAPI_3$ interfaces with the BHJ film, resulting in both $MAPI_3/PC_{61}BM$ and $MAPI_3/TT$ interfaces. It should be noted that the "/" and ":" labels denote a bilayer heterojunction and bulk heterojunction, respectively. In addition, N2200 is an additive (~6% weight) to the BHJ film used to improve electron mobility in the OPV BHJ layer,

with the aim of balancing the rapid electron mobility of perovskites. Figure 5.1c indicates that the integrated devices fabricated for this study have high as ~17 % PCE measured under a reverse scan. Figure 5.1d displays the EQE spectrum of the integrated device, which clearly has a TT contribution at the 780-900 nm range reaching ~20% and indicating TT absorption contributes to the photocurrent. These device and film preparation conditions are therefore used in the current laser spectroscopy study to resolve the exciton and charge dynamics in the integrated devices.

In Figure 5.1b, $MAPI_3$ has a typical broad continuous absorption spectrum in the visible range up to 785 nm, while the TT polymer's absorption covers the range of $600 - 870$ nm with a peak absorption at 830 nm, making this material suitable for integrated Per/OPV devices with red-shifted absorption. The $MAPI_3$ / TT: $PC_{61}BM$ film exhibits a broader absorption approximately matching the sum of absorption of the composite materials. To study charge dynamics using fs-TAS, the $MAPI_3$ and TT material were independently excited by using laser excitation pulses with 550 nm to excite $MAPI_3$ (called herein a perovskite mode) and 840 nm to excite the BHJ film (called herein an OPV mode). It should be noted that the sample was excited from the glass substrate direction, as would occur in an operational device, and as a result the 550 nm light is absorbed by the thick $MAPI_3$ perovskite film (absorbance of more than 2 (1% transmittance)). Therefore, a negligible signal from the TT:$PC_{61}BM$ blend was generated. The 830 nm pump excites only the TT:$PC_{61}BM$ blend due to the transparency of $MAPI_3$ at this wavelength. The following section, discusses the results from spectroscopy measurements in the perovskite mode and the OPV mode.
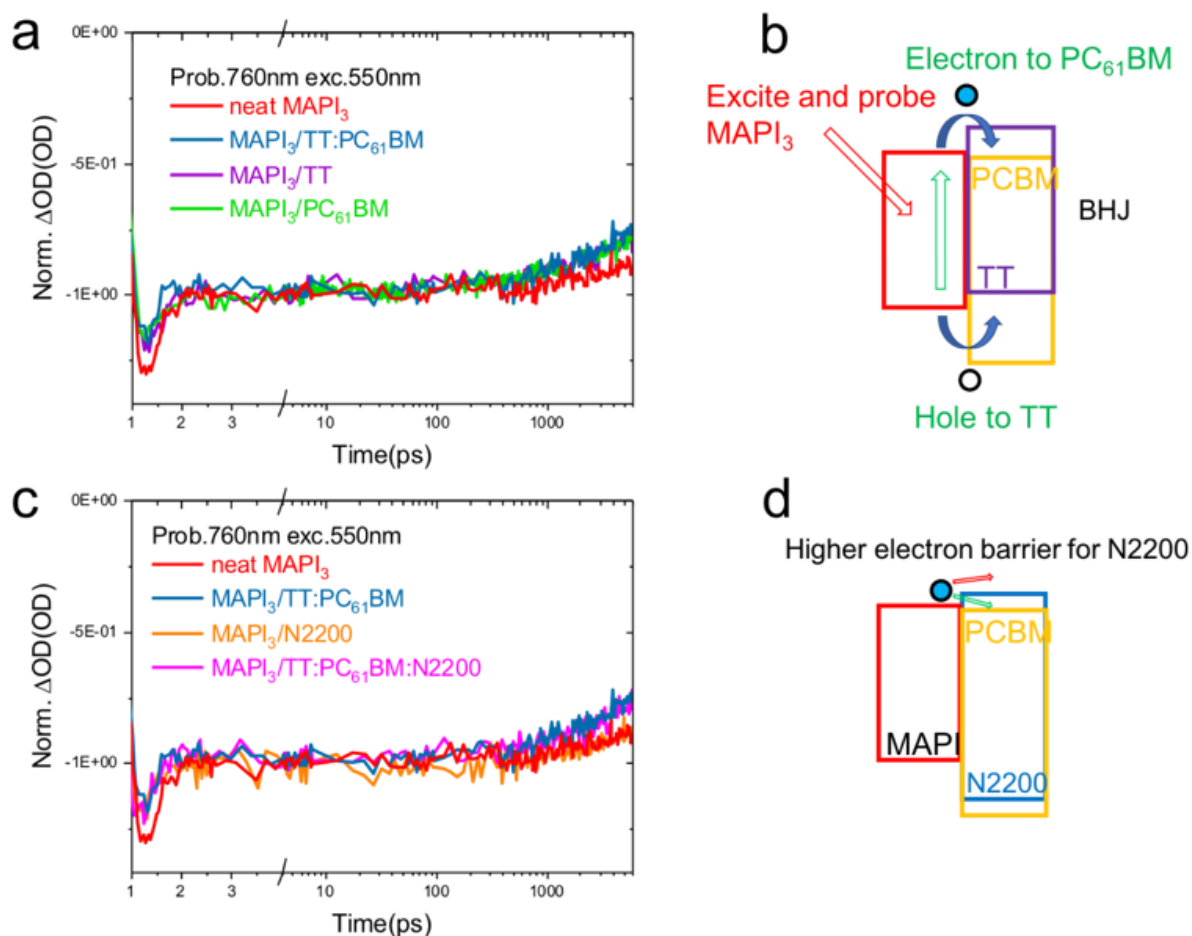
5.4.1. Perovskite mode visible range

Figure 5.2 a) fs-TAS dynamics of neat MAPI₃ (red line), MAPI₃/TT (purple line), MAPI₃/PC₆₁BM (green line), and MAPI₃/TT:PC₆₁BM (dark cyan line) films at 765 nm. Excitation wavelength used was 550 nm; b) schematic figure of possible charge-carrier transfer pathways from MAPI₃ to PC₆₁BM or TT; c) fs-TAS dynamics of neat MAPI₃ (red line), MAPI₃/TT:PC₆₁BM (dark cyan line), MAPI₃/N2200 (orange line), and MAPI₃/TT:PC₆₁BM:N2200 (pink line) were carried out using a probe wavelength of 765 nm with an excitation wavelength of 550nm; d) schematic figure of possible charge-carrier transfer pathways from MAPI₃ to PC₆₁BM with N2200.

Figure 5.2a presents the fs-TAS dynamics of the photo-bleaching signal of MAPI₃ at 765 nm with an excitation energy density of ~1µJ/cm². The photo-bleaching dynamic of pure MAPI₃ (red line) has an ultrafast sub-ps decay corresponding to peak-shifting towards longer wavelengths (due tocarrier cooling down to the bottom of the band) and a slower nanosecond decay (τ= 46 ns, assumed for simplicity to be a single exponential) corresponding to e-h

recombination in $MAPI_3$. The films with organic heterojunctions exhibit nearly identical bleach recovery dynamics ($PC_{61}BM$ and TT, $\tau= 22$ and 24 ns, respectively) which are shorter than the recovery of the neat $MAPI_3$ dynamics. This suggests that charge carriers from $MAPI_3$ are transferred to each of the organic films deposited onto $MAPI_3$. However, the overall bleach recovery does not give insight into the exact timescales of the charge transfer processes which, according to interfacial energetics, are expected to include electron transfer from $MAPI_3$ to $PC_{61}BM$ and hole transfer by TT to $MAPI_3$. The presence of quenching in the $MAPI_3$/ TT film suggests the existence of hole transfer from $MAPI_3$ to TT (Figure 5.2b). The $MAPI_3$ bleach in $MAPI_3/TT:PC_{61}BM$ exhibits a similar decay of $\tau=20$ ns compared with the rest of the films. The impact of the addition of N2200 to the charge dynamics in the films was also investigated and data presented in Figure 5.2c. The presence of N2200 (pink line $\tau=25$ ns) does not significantly affect the bleach dynamics of $MAPI_3$ and $MAPI_3/TT:PC_{61}BM$, suggesting little effect of this additive to early timescale electron-hole recombination dynamics. N2200 is a well-performing non-fullerene accepter material, but in this system, it is only used as an additive (6% weight) to increase the electron charge-carrier mobility.
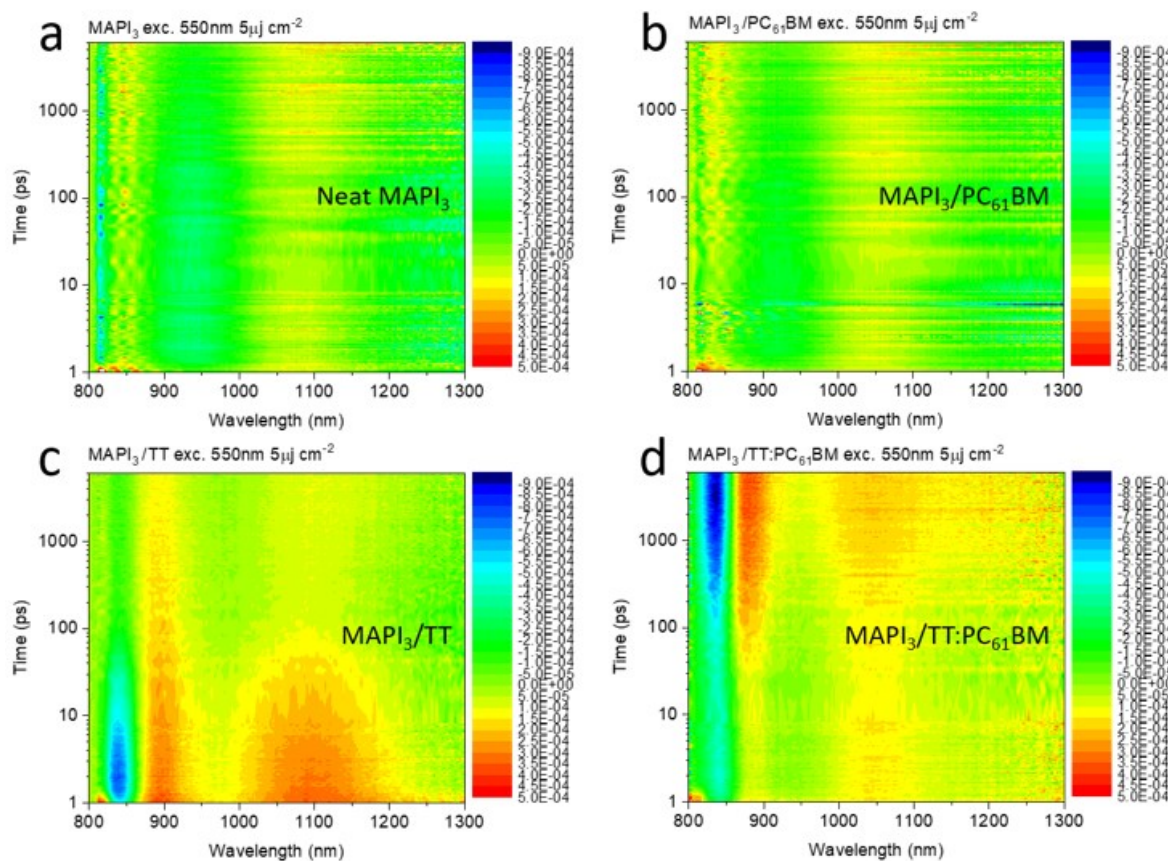
5.4.2. Perovskite mode NIR range

Figure 5.3 fs-TAS, 3D colour-filled plots of ultra-fast transient absorption of a) neat MAPI$_3$, b) MAPI$_3$/PC$_{61}$BM, c) MAPI$_3$/TT, and d) MAPI$_3$/TT:PC$_{61}$BM films were carried out using a probe wavelength range of 800 to 1300 nm, with excitation wavelength of 550nm.

Figure 5.3 displays 3D colour-filled plots of fs-TAS in the NIR range with the excitation of MAPI$_3$ using 550 nm laser. Figures 5.3a and 1b display the spectra of MAPI$_3$ and MAPI$_3$/PC$_{61}$BM, which have only a weak oscillation signal which may be caused by the light reflectance coming from the different interfaces in the films and devices. In this study, this signal is not considered because of its very low amplitude compared to the photoinduced excitonic and polaron signal. As shown in Figure 5.3c, the addition of TT to the OPV blend results in a strong negative signal at 840 nm and positive signal at 900 and 1100 nm. This negative signal at 840 nm is assigned to GSB/SE signals of TT, and the positive signals to TT polaron absorption, consistent with the corresponding data for neat TT and TT:PC$_{61}$BM films. (see figure 5.8a and 5.8b below) Whilst these signals appear with the pump pulse in the

MAPI$_3$/TT film, the same spectral signatures are formed in MAPI$_3$/ TT:PC$_{61}$BM in Figure 5.3d after ~100 ps, indicating population of TT on reduced timescales likely via delayed charge-transfer processes.
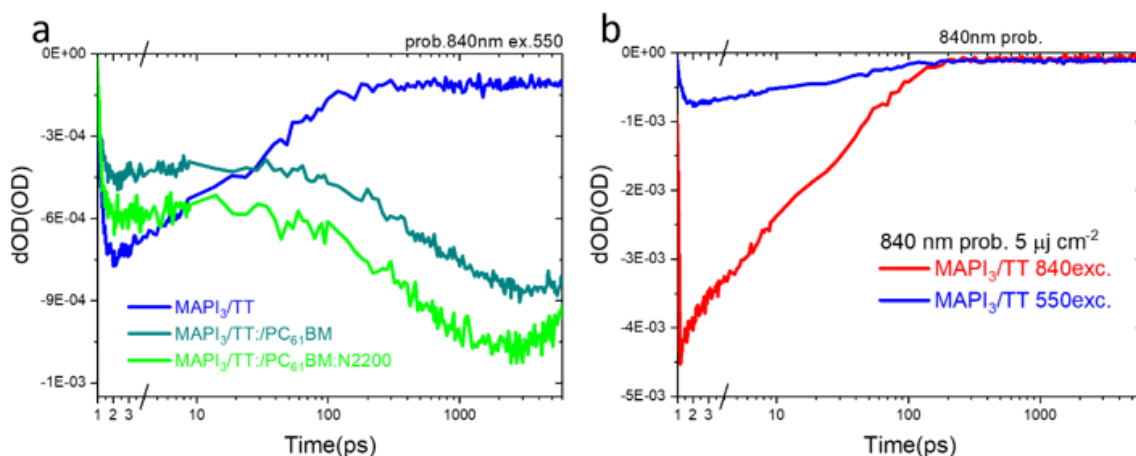

Figure 5.4 a) fs-TAS dynamics of MAPI$_3$/TT (blue line), MAPI$_3$/TT:PC$_{61}$BM (dark cyan line) and MAPI$_3$/TT:PC$_{61}$BM:N2200 (green line) films measured with probe wavelength of 840 nm and excitation wavelength of 550nm; b) MAPI$_3$/TT films probe at 840 nm excited using 550 (blue line) and 840 nm (red line) wavelength with 5μjcm^{-2}.

Figure 5.4a presents fs-TAS dynamics of the negative photobleaching signal at 840 nm (probing TT GSB/SE) using an excitation fluence of ~5μJ/cm^2 following excitation of MAPI$_3$ with 550 nm excitation. Since MAPI$_3$ perovskite does not exhibit any specific signal in the NIR region, there is no signal for neat MAPI$_3$ and MAPI$_3$/PC$_{61}$BM. However, there is a strong negative TT photo-bleaching signal in the MAPI$_3$/TT film, which has a rise-time constant of 0.6 ps. This signal may indicate the transfer of holes from MAPI$_3$ to TT or could be an exciton energy transfer from MAPI$_3$ interface. This signal then decays with a time constant of ~35 ps. An additional long-lived signal at 6 ns, which is ~5% of the total TT signal, is also observed. In addition, the MAPI$_3$/TT film was excited at 880 nm to test signal assignment and dynamics, and the direct excitation transient signal of TT was identified in Figure 5.4b. This signal has rise and decay times of 0.2 and 25 ps, respectively, which are faster than the TT signal observed

upon MAPI$_3$ excitation. The long-lived signal left at 6 ns is just 2%, indicating clear differrences between the measurements. The fast charge-carrier transfer properties between organic donnor and MAPI$_3$ perovskite materials is consistent with the publication by Ke Gao et al., which suggests ultrafast (<2 ps) population of the BHJ layer by the perovskite layer.[6a] Focusing back on Figure 5.4a, the addition of PC$_{61}$BM to the TT organic film completely changes the observed signal dynamics. In addition to the fast rise of the TT signals corresponding to hole-transfer from MAPI$_3$ to TT, there is a ns signal rise which indicates delayed hole transfer kinetics. The hole signal and the rate of delayed population are enhanced with the addition of N2200 to the system, suppressing the sub-2 ps hole-transfer from MAPI$_3$ to TT. These results indicate that charge dynamics in the MAPI$_3$/BHJ integrated device are complex and involve each of the materials separately.
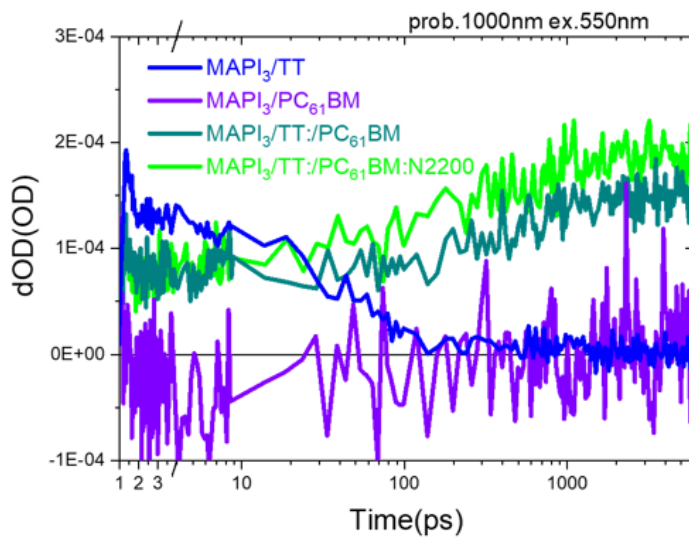

Figure 5.5 the positive fs-TAS dynamics signal observed for the samples with TT using an excitation fluence of ~5μj/ cm^2 of MAPI$_3$/TT (Blue line), MAPI$_3$/PC$_{61}$BM (purple line), MAPI$_3$/TT:PC$_{61}$BM (dark cyan line), and MAPI$_3$/TT:PC$_{61}$BM:N2200 (green line) films at 1000 nm. Excitation wavelength used was 550 nm.

In Figure 5.5, the photo-induced absorption at 1000 nm is assigned to the hole polaron absorption of TT polymer, as it appears only in the presence of TT. This signal does not appear

in the spectra of neat TT films, further confirming signal assignment. Probing the TAS signal from 1000 nm (assigned to polaron absorption, which extends from 900-1300nm) allows cavity effects to be avoided after OPV deposition on the perovskite. In the TT/MAPI$_3$ film, the dynamics show hole injection into the TT on an early time scale and rapid recombination (τ=48 ps), consistent with the bleach dynamics of TT measured at 840 nm. The fast charge-transfer may be related to the high efficiency of hole-mobility of perovskite films. In the films with added PC$_{61}$BM, the dynamics of hole formation are clearly delayed, as expected from the data in Figure 5.6. The hole-transfer from MAPI$_3$ has two time constants (see Figure 5.6 for fit), a fast constant which corresponds to instantaneous MAPI$_3$-TT transfer, and a delayed constant which may indicate heterogeneity in the MAPI$_3$-TT interface or slower charge transport/ transfer processes. This slower transfer will be discussed in Figure 5.15 below in further detail.
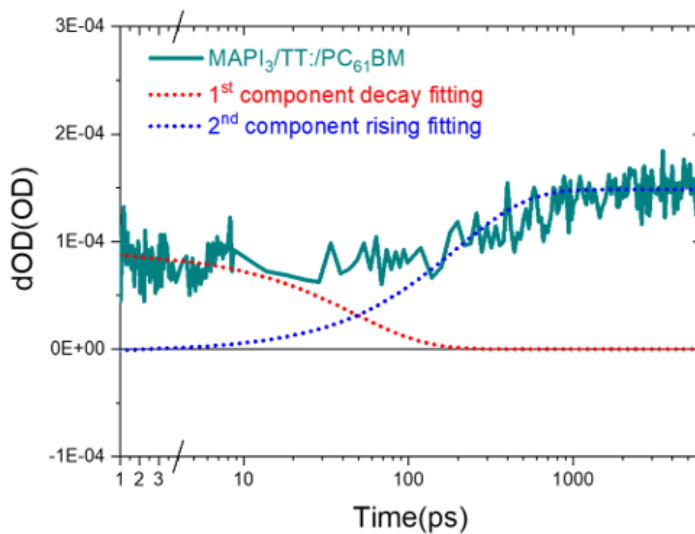

Figure 5.6 fs-TAS dynamics fitting with a bi-exponential function of MAPI$_3$/TT:PC$_{61}$BM (dark cyan line) films probed at 1000 nm excited at 550 nm. 1st decay component and 2nd rising component with red and blue dotted lines, respectively.
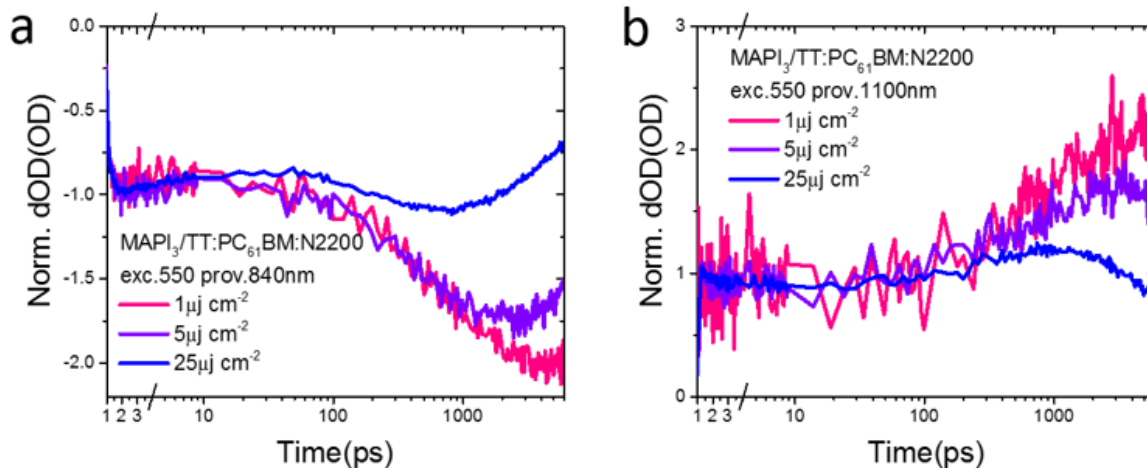
Figure 5.7 fs-TAS dynamics of the excitation density dependence of the 550 nm excited TT photo bleach of MAPI$_3$/TT:PC$_{61}$BM:N2200 (green line) films at a) 840 nm and b) 1100nm.

In Figure 5.7, bleach signal at 840 and the positive polaron absorption at 1100 nm, both show similar decay dynamics. These negative and positive 2nd rising components speed up with increased charge density. The exact nature of this recombination cannot be confirmed, but it is likely to be at the PC$_{61}$BM:TT interface as similar time-constants are observed in TAS of organic BHJ blends.[9]
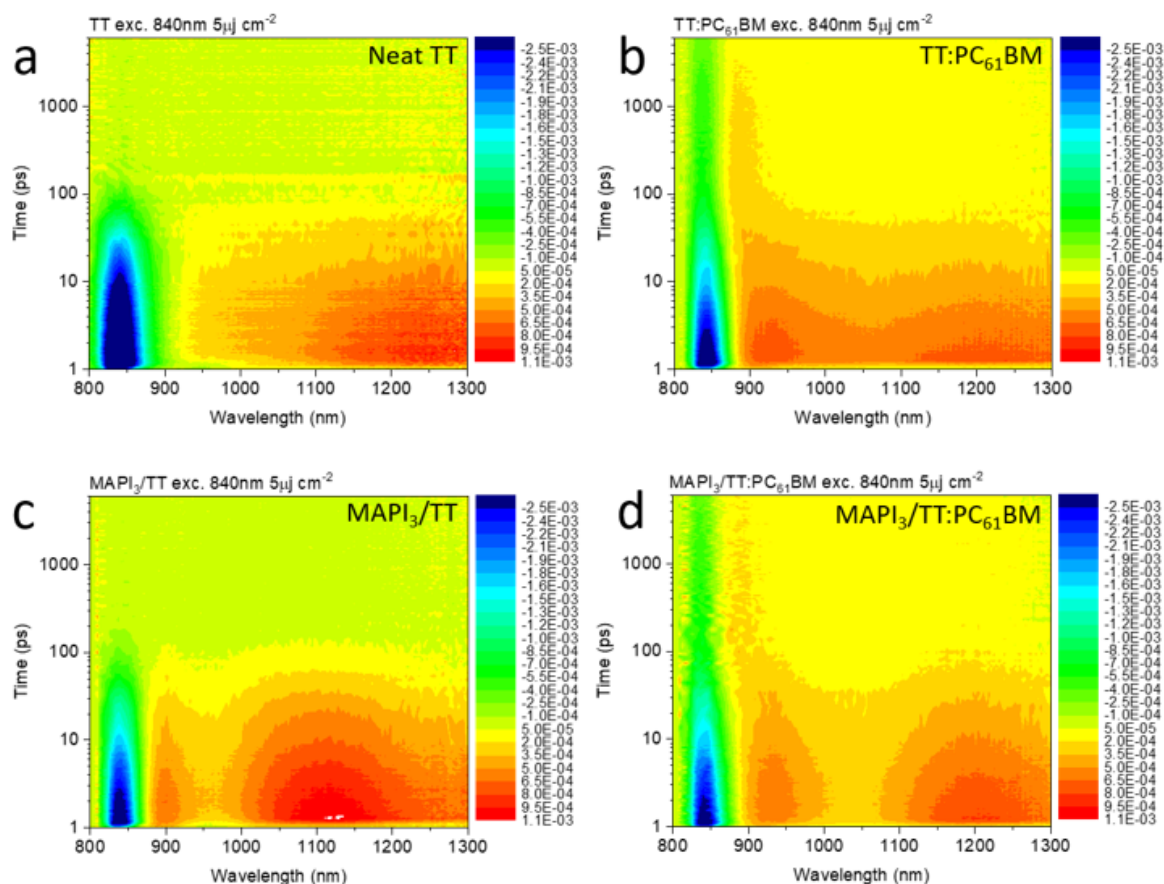
5.4.3. OPV mode NIR range

Figure 5.8 displays 3d colour-filled plots of fs-transient absorption spectra in the NIR range for direct excitation of TT, using an 840 nm laser. a) neat MAPI₃, b) MAPI₃/PC₆₁BM, c) MAPI₃/TT, and d) MAPI₃/TT:PC₆₁BM films. Measurements were carried out using a probe wavelength range of 800 to 1300 nm, with an excitation wavelength of 840 nm.

The kinetics following direct excitation of TT (OPV mode) are now considered in more detail. In Figure 5.8a, TT material displays a bleach signal at 840 nm and positive excited-state absorption with a peak at 1200 nm. When TT is mixed with $PC_{61}BM$ (BHJ), the bleach lifetime is prolonged, and the associated excited-state absorption signals changed in spectral shape and lifetime. The positive excited-state absorption is from TT polarons. The positive signal at 900 nm also appears in the presence of the $MAPI_3$ junction, but the positive signal between from around 920 to 1100 nm reduced, seems it is affected by interference effects due to the oscillations. In $MAPI_3/TT:PC_{61}BM$ (Figure 5.8d), the bleach and TT polaron signals are much like in $TT:PC_{61}BM$ (Figure 5.8b).
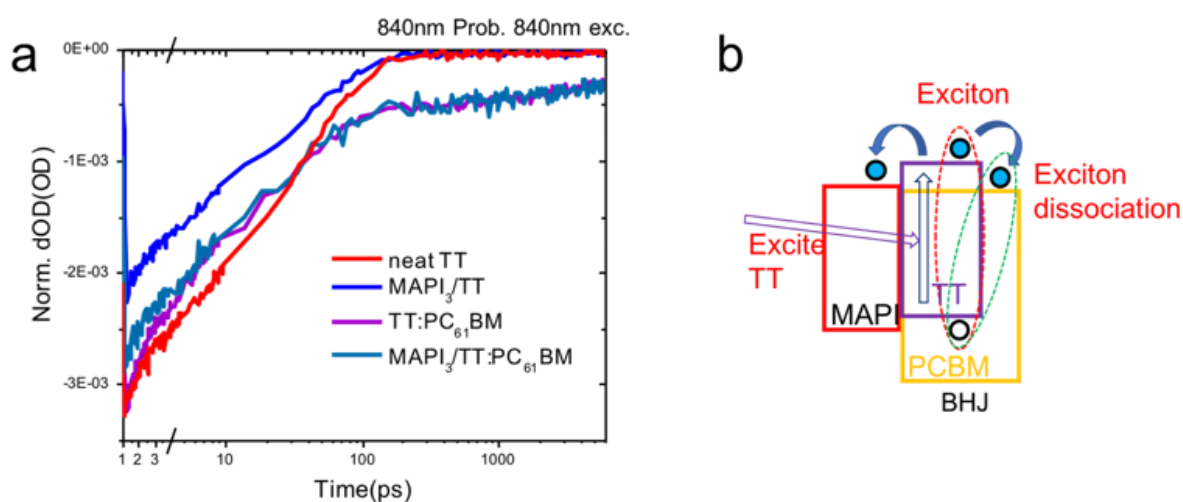
Figure 5.9 a) fs-TAS dynamics of neat TT (red line), MAPI$_3$/TT (blue line), MAPI$_3$/PC$_{61}$BM (purple line), and MAPI$_3$/TT:PC$_{61}$BM (dark cyan line). Measurements were carried out using a probe wavelength of 840 nm, with an excitation wavelength of 840nm; b) schematic drawing of exited hole of TT dynamics

To understand the operating mode of OPV excitation, the TT photo-bleaching at 840 nm after 840 nm excitation was plotted in Figure 5.9. Figure 5.9 illustrates the dynamics of neat TT (red line), MAPI$_3$/TT (blue line), TT:PC$_{61}$BM (purple line), and MAPI$_3$/TT:PC$_{61}$BM (dark cyan line) excited using 840 nm at 5 μj cm^{-2} excitation. The exciton formed in the neat TT film relaxes to the ground state with τ=40 ps. The intensity of the TT photo-bleaching is reduced by the MAPI$_3$ layer junction, suggesting a fast electron-transfer from TT to MAPI$_3$. Whilst the data cannot distinguish between electron- or hole- transfer, the position of the highest occupied molecular orbital (HOMO) and lowest unoccupied molecular orbital (LUMO) levels of the polymer, compared against MAPI$_3$ conduction and valence band, would suggest hole-transfer is enthalpically forbidden. Whilst the yield of long-lived TT bleach is low, contradicting the conclusion for rapid electron transfer from TT to MAPI$_3$, the analysis of the positive hole signal of TT in Figure 5.10 indicates rapid formation of positive hole signal at 920 nm after excitation of TT, which is consistent with assigned electron transfer from TT to MAPI$_3$. The TT:PC$_{61}$BM BHJ film has the typical decay dynamics for OPV material behaviour: excited-state absorption

occurs with light absorption, followed by the formation of long lifetime (τ=10 ns) polaron signals, assigned to electron transfer from TT to $PC_{61}BM$. The signal left after exciton decay at 200 ps is ~20% of the total photo-induced absorption, suggesting that the polaron generation efficiency in this blend is 20%. Once a $MAPI_3$ layer is added, the PB intensity of TT is mostly unchanged with a slightly lower initial TT bleach signal, which is likely to be due to quenching by $MAPI_3$. The ratio of the initial signal and that at 200 ps (expected to arise from photo-generated polarons) is ~10% higher compared with TT:$PC_{61}BM$, which indicates extra electron transfer to $MAPI_3$ contributes to long-lived polaron yields.
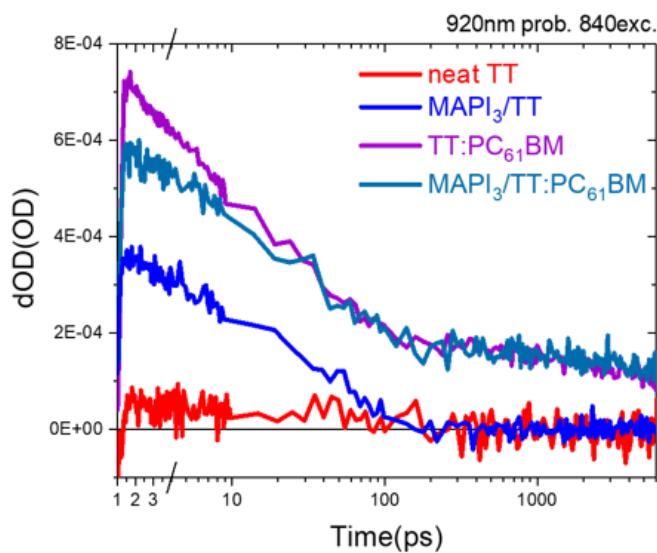

Figure 5.10 fs-TAS dynamics of neat TT (red line), MAPI₃/TT (blue line), MAPI₃/PC₆₁BM (purple line), and MAPI₃/TT:PC₆₁BM (dark cyan line). Measurements were carried out using a probe wavelength of 920 nm with an excitation wavelength of 840nm.
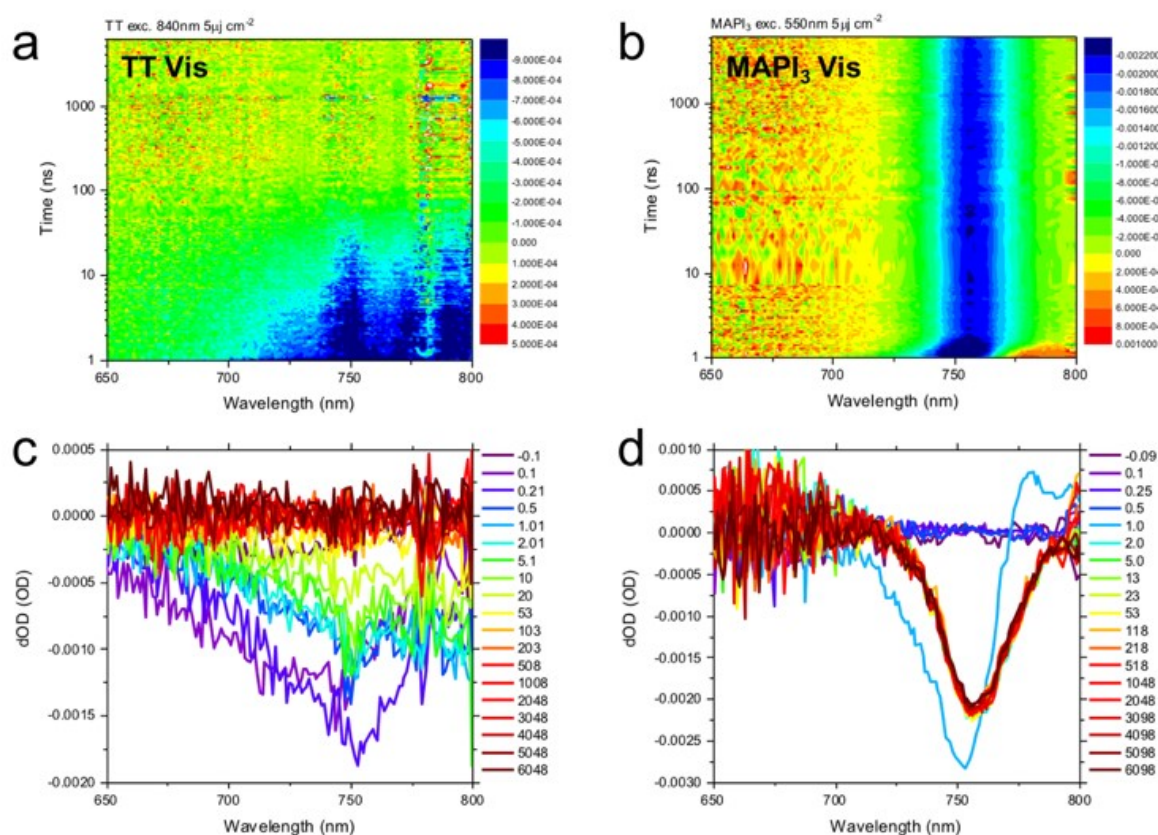
5.4.4. OPV mode visible range

Figure 5.11 fs-TAS 2D spectra and spectra of neat TT excited at 840 nm (a and c), and neat MAPI$_3$ excited at 550 nm (b and d), with the same excitation density of 5μjcm^{-2}.

To study the visible range in TAS for OPV mode, together with MAPI$_3$ perovskite, both TT and MAPI$_3$ photo-bleaching are required to be considered since both materials show a negative signal in this range. Note that the photo-bleaching of TT has a short lifetime, with a peak at ~750 nm and inset at ~700 nm, which is a wide signal with low intensity (Figure 5.11). MAPI$_3$ has a relatively sharper and longer lifetime signal which starts at ~720 nm, and with a peak

intensity at ~760 nm. Thus, the negative signal probe at 760 nm is a photobleaching signal of MAPI$_3$, including a negative TT signal.
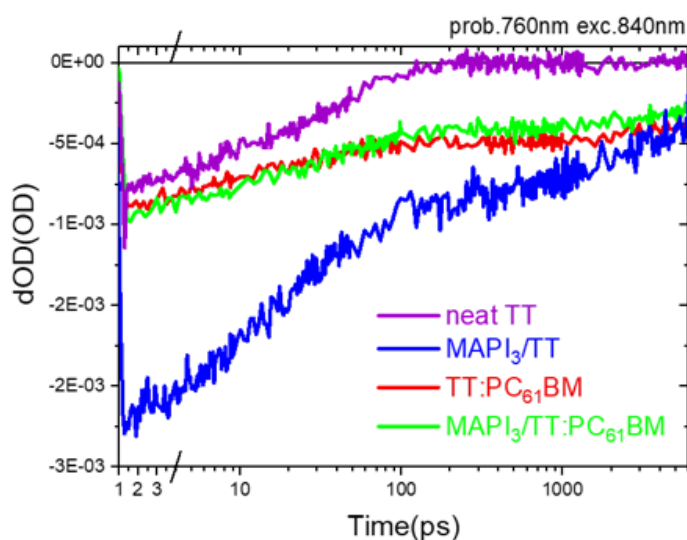

Figure 5.12 fs-TAS dynamics of neat TT (purple line), MAPI$_3$/TT (blue line), MAPI$_3$/PC$_{61}$BM (red line), and MAPI$_3$/TT:PC$_{61}$BM (green line). Measurements were carried out using a probe wavelength of 760 nm, with an excitation wavelength of 840 nm.

Figure 5.12 displays the MAPI$_3$ and TT bleaching dynamics at 760 nm for the films of TT, TT:PC$_{61}$BM, TT:PC$_{61}$BM:MAPI$_3$, and TT:MAPI$_3$. Neat TT exhibits similar dynamics as 840 nm PB signal, and together with PC$_{61}$BM blend, the polaron signal can also be observed after 100 ps. Due to the relatively high proportion of MAPI$_3$ PB signals, the TT/MAPI$_3$ bilayer exhibits significantly different dynamics: from 1-1000 ps, the decay is similar to TT PB signals at 840 nm, and subsequent decay looks like MAPI$_3$ free charge carrier. Therefore, at the early timescale before the few ps, excitons may initially diffuse into the MAPI$_3$ and TT interface in the TT film, and after 100 ns, the binding is dissociated and forms free charges, after which they would recombine in the MAPI$_3$ film and the TT bulk film. However, in MAPI$_3$/TT:PC$_{61}$BM films, since the TT has an interface with MAPI$_3$ and PC$_{61}$BM, excitons formed in the TT have dissociation competition between the PC$_{61}$BM interface and the MAPI$_3$ interface, the intensity of the fast component is reduced.
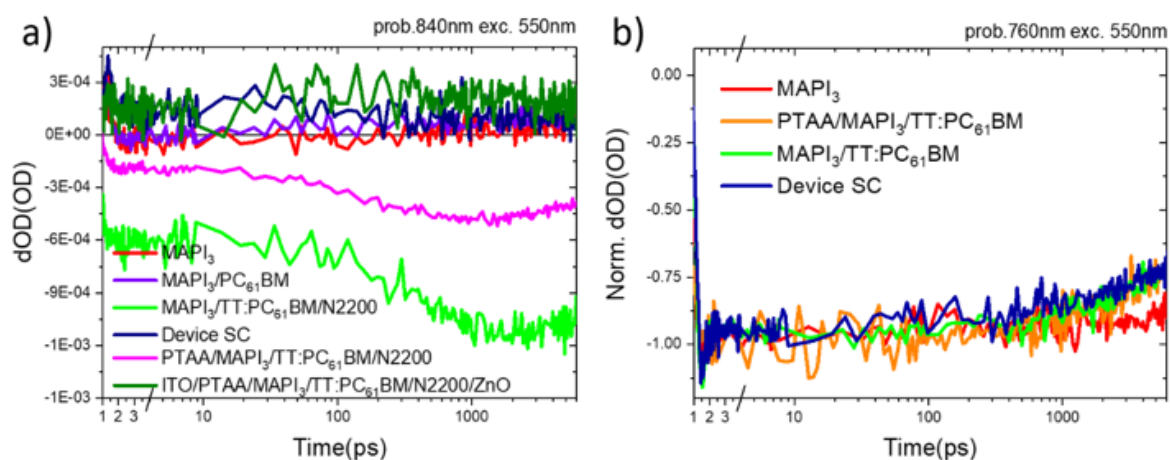
5.4.5. Full device measurement

Figure 5.13 a) fs-TAS dynamics of neat MAPI₃ (red line), MAPI₃/PC₆₁BM (purple line), MAPI₃/TT:PC₆₁BM:N2200 (green line), PTAA/MAPI₃/TT:PC₆₁BM:N2200 (pink line), ITO/ PTAA/MAPI₃/TT:PC₆₁BM:N2200/ZnO (dark green line), and the full device in short circuit condition (blue line). Measurements were carried out using a probe wavelength of 840 nm with an excitation wavelength of 550 nm; b) fs-TAS dynamics of neat MAPI₃ (red line), PTAA/MAPI₃/TT:PC₆₁BM (orange line), MAPI₃/TT:PC₆₁BM (green line), and the full device in short circuit condition (blue line). Measurements were carried out using a probe wavelength of 760 nm with an excitation wavelength of 550 nm.

To investigate the carrier movement in the integrated cell, the TAS of the active layer was measured with the hole and electron transport layers and the complete devices, presented in Figure 5.13a. Our results show a strong negative hole signal from the MAPI₃/TT/PC₆₁BM/N2200 film which is significantly reduced by the PTAA hole transport layer, indicating a change in the charge dynamics in the presence of the hole extracting PTAA. Likewise, the addition of ZnO film at the top of MAPI₃ hinders the hole extraction by the TT material. This result is surprising considering the expectation that internal electric fields at high carrier densities play a small role in photocurrent generation by perovskite devices.[10] Such however clearly arise in the presence of ZnO and PTAA in our integrated perovskite/OPV devices. This result is significant in respect to device performance as hole transfer from MAPI₃ to TT is expected to generate energy losses in the system due to TT's mismatched HOMO level.

Importantly, the full device under a SC condition shows similar lack of signal from hole transfer as in PTAA/MAPI$_3$/TT:PC$_{61}$BM:N2200/ZnO. This is despite of that observed in the NIR OPV mode (figure 5.13b) photo bleach signal of MAPI$_3$ indicating charge-extraction rates equivalent to the simpler MAPI$_3$/TT:PC$_{61}$BM film. These results are discussed below in terms of possible band-bending conditions leading to favourable photocurrent generation and avoiding charge trapping in the TT HOMO in complete devices

5.5. Discussion

According to the fs-TAS results presented, the presence of multiple interfaces in these integrated junctions and solar cells create a complex mix of charge-transfer processes on different timescales and with different efficiencies. The perovskite device is known to have current and voltage hysteresis, and light and electric field induced effects.[11] Thus the analysis of the carrier dynamics on perovskite device in working condition is very difficult because of the dynamics is easily affected by the film structure and the energy levels of contact materials as well as band bending effects and fermi level shifts which will be modulated by irradiation in device operating condition.[11a, 12] In this regard, it is very complicated to study an integrated device which has two different absorber materials which have different properties; one is organic the other is inorganic-organic hybrid. In particular bilayer films are generally used for this type of study quantifying the charge transfer yield between the perovskite and electron or hole transport material. However, as mentioned, under illumination the electric field in the perovskite material is likely to be modulated with charge build-up impacting on band-bending

at the MAPI$_3$ interfaces.[12a] Furthermore charge generation in the organic BHJ could also be dependent on electric fields.

Our spectroscopy results suggest electron transfer from TT to PC$_{61}$BM is ~20% (determined from the ratio of decay constant (τ_0/τ)) both in the TT:PC$_{61}$BM and MAPI$_3$/TT:PC$_{61}$BM structures, which is in good agreement with the observed ~20% EQE at the TT absorption maximum, likely indicating that most of the electron-hole pairs generated from electron transfer from TT excitons contribute to photocurrent generation. This agreement of the TAS and EQE results measured in open and short circuit condition, respectively, may suggest that the OPV mode is significantly limited by exciton separation.
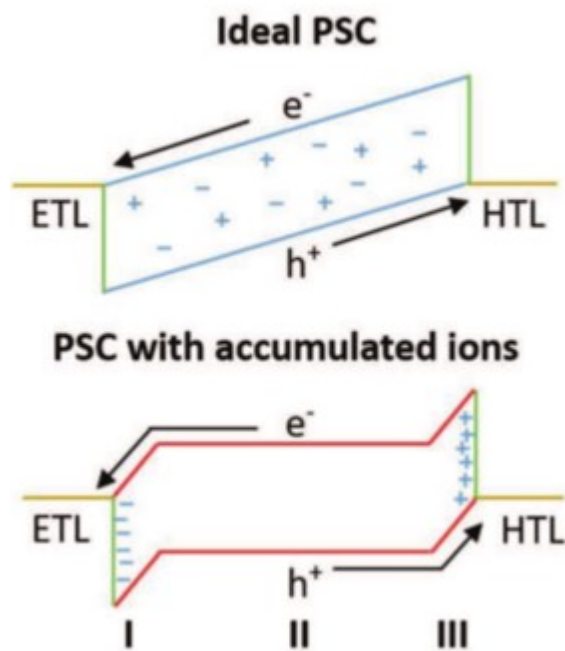

Figure 5.14 Band diagram of an ideal perovskite solar cell (PSC) without ion migration (top) and after ion migration (bottom). (Figure source: Adv. Electron. Mater. 2018, 1800500)[12a]

Figure 5.14 shows diagram depicting band bending in perovskite photovoltaic devices without (top) and with (bottom) ion motion. Ion motion induced for example by irradiation at open circuit can result in screening of the device bulk electric field, confining fields to interface regions.[12a]

Excitation of MAPI$_3$ reveals a completely different picture, where hole transfer from MAPI$_3$ to TT is possible but resulting charges have short lifetimes of tens of picoseconds, with only 5% long-lived charges. This can be expected to cause low photocurrent generation yields in complete devices, however, this does not appear to be the case according to our EQE and JV measurements. Instead, the presence of PC$_{61}$BM facilitates efficient hole-transfer dynamics on the 200 ps timeframe which can be linked to charge accumulation at the MAPI$_3$/TT interface, possibly leading to favourable conditions for hole-transfer band-bending. This is discussed in further detail within Figure 5.15. Clearly, the addition of PC$_{61}$BM to TT plays a significant role in providing a pathway for charge transfer. The addition of N2200 also plays a role in the charge-transfer processes, but whilst increasing hole transfer yields with ~10-20 %, N2200 has little further impact on the charge-transfer dynamics. Therefore, it appears that N2200 plays a role as an additive for optimising either or both the film morphology and energetics and leading

to increased photocurrent. Clearly, further experiments are required to analyse N2200's effect on carrier mobility.
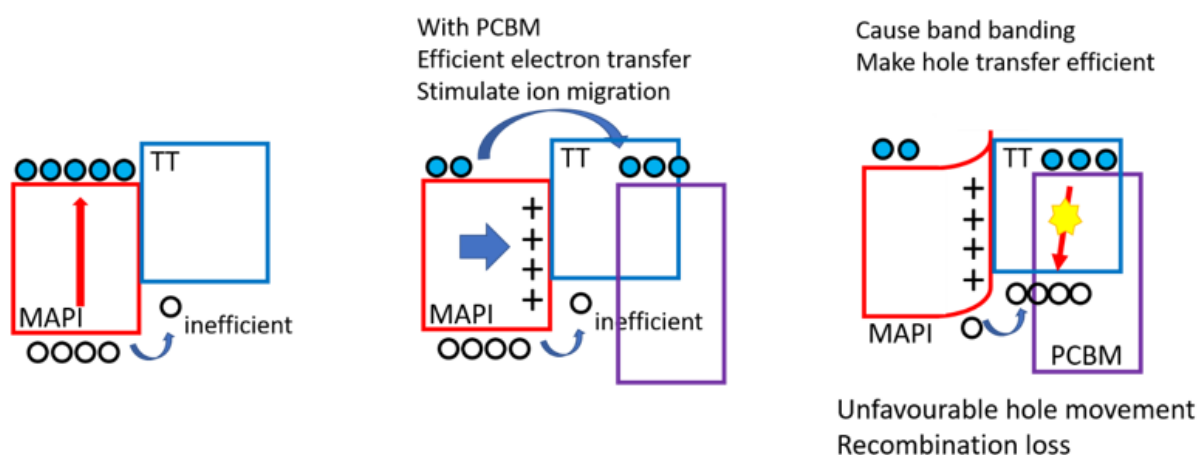
5.5.1. Perovskite mode hole polaron in TT

Figure 5.15 Schematic figure of the charge-carrier dynamics model suggested for MAPI₃ / organic BHJ bilayers. MAPI₃ hole transfer to TT with and without PC₆₁BM. Strong additional hole transfer is induced by transferred electron from MAPI₃ to PC₆₁BM

Figure 5.15 presents model energy-level diagrams, in open circuit condition, depicting charge-transfer processes identified to take place at the interfaces in $MAPI_3$ / organic BHJ bilayers. As already discussed, hole transfer from $MAPI_3$ to TT alone is not efficient, whereas addition of $PC_{61}BM$ leads to significant electron-transfer from $MAPI_3$ to $PC_{61}BM$ leading to a build-up of holes in $MAPI_3$ which are expected to accumulate at the $MAPI_3$/TT: $PC_{61}BM$ interface. This may induce ion migration, which will in turn create band-bending in favour of hole transfer from $MAPI_3$ to TT which is observed in our film measurements at short circuit.[6b, 12c, 13] The band-bending also obstructs the extraction of an electron by $PC_{61}BM$.

5.5.2. fs-TAS of complete devices

It is remarkable that the complete MAPI$_3$/TT:PC$_{61}$BM device successfully works with high V$_{OC}$ and FF, indicating no significant charge recombination losses between the organic and inorganic interfaces. One hypothesis to explain this result is that the samples prepared for fs TAS measurements are bilayer films rather than complete devices, meaning that carrier-transfer yields are only measured at open circuit conditions different from the device operating conditions. To address the issue, measurements under short circuit conditions might help to identify recombination and charge-transfer mechanisms in the complete device. fs-TAS was therefore performed with devices under short circuit. (see figure 5.13a) For this study, the transparent top electrode was deposited with a smaller thickness to provide transparency for TAS experiments.
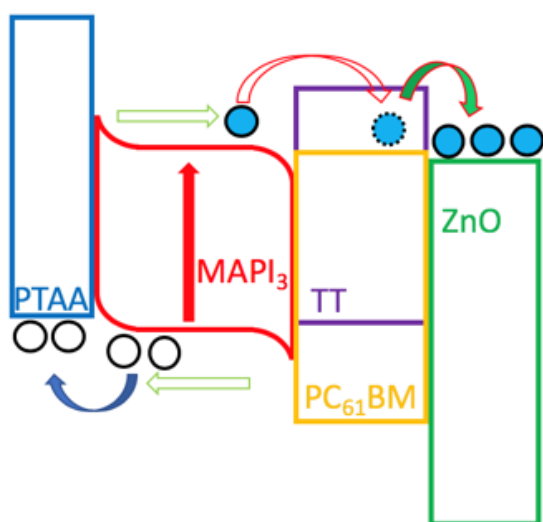

Figure 5.16 Energy diagram of the full device in short circuit condition with excitation of MAPI$_3$.

The strong negative photo-bleaching hole signal of fs-TAS shown in MAPI$_3$/TT:PC$_{61}$BM:N2200 film in flat band condition of the under layer of MAPI$_3$ (that is the

other side of the $MAPI_3$ and TT:$PC_{61}BM$:N2200 interface) is reduced by adding the PTAA. This suggests that in such a structure, the injection of holes to TT is suppressed by changes in the direction of hole movement and the reduction of hole accumulation at the $MAPI_3$/TT: $PC_{61}BM$ interface which is otherwise expected to happen due to significantly faster hole mobility of $MAPI_3$ than the organic film. Similarly, the addition of ZnO film on top of the TT:$PC_{61}BM$:N2200 layer significantly removes charge-carrier accumulation and reduces hole extraction by the TT material. (see Figure 5.16) It appears that the electrons collected by $PC_{61}BM$, and expected to attract + ions from the $MAPI_3$ layer, are extracted by ZnO and further reducing the band bending effects identified in films, equivalent to V_{OC} conditions. In summary, the device measurements under SC lead to a conclusion that the mechanisms of charge-generation and movement are completely different from those at V_{OC} due to band-bending and internal electric field changes.

5.6. Conclusion

In this study, it is demonstrated that charge-carrier dynamics in integrated $MAPI_3$/TT: $PC_{61}BM$ devices are strongly influenced by the conditions at which devices are measured, specifically whether at SC conditions. Our spectroscopy data for films, equivalent to V_{OC} reveal relatively inefficient generation of charges by absorption by TT, but very efficient generation of charges from $MAPI_3$. The latter is facilitated by the presence of $PC_{61}BM$, which opens an electron-transfer pathway from $MAPI_3$ to $PC_{61}BM$. This, in turn induces band-bending at the $MAPI_3$/TT interface and forces efficient hole transfer from $MAPI_3$ to TT which is in an opposite direction of the current flow in the device working condition. The measurement of complete devices at SC conditions indicates very different charge dynamics that have significantly reduced hole transfer from $MAPI_3$ to TT. This reduction is caused by hole extraction (from $MAPI_3$ by PTAA)

and electron extraction (from $PC_{61}BM$ by ZnO), reducing the band-bending noted at V_{OC} and therefore blocking undesirable hole transfer to TT. Our spectroscopy measurements of films also indicate that electron transfer from TT to $MAPI_3$ is possible but not particularly efficient. This study, therefore, demonstrates that the analysis of perovskite-OPV integrated devices requires a careful analysis of each of the constituent layers and interfaces, and also requires consideration of the conditions whether at V_{OC} or J_{SC} to build a more complete picture of the device performance.

5.7. References

[1]   a) J. Liu, M. Ozaki, S. Yakumaru, T. Handa, R. Nishikubo, Y. Kanemitsu, A. Saeki, Y. Murata, R. Murdey, A. Wakamiya, *Angewandte Chemie International Edition.* **2018**, 57, 13221; b) Q. Guo, H. Liu, Z. Shi, F. Wang, E. Zhou, X. Bian, B. Zhang, A. Alsaedi, T. Hayat, Z. Tan, *Nanoscale.* **2018**, 10, 3245; c) Y. Wang, Y. Zhou, T. Zhang, M.-G. Ju, L. Zhang, M. Kan, Y. Li, X. C. Zeng, N. P. Padture, Y. Zhao, *Materials Horizons.* **2018**, 5, 868; d) Z. Liu, Y. Zhong, B. Sun, X. Liu, J. Han, T. Shi, Z. Tang, G. Liao, *ACS Applied Materials & Interfaces.* **2017**, 9, 22361.

[2]   a) S. Albrecht, B. Rech, *Nature Energy.* **2017**, 2, 16196; b) N. N. Lal, Y. Dkhissi, W. Li, Q. Hou, Y.-B. Cheng, U. Bach, *Advanced Energy Materials.* **2017**, 7, 1602761; c) K. A. Bush, A. F. Palmstrom, Z. J. Yu, M. Boccard, R. Cheacharoen, J. P. Mailoa, D. P. McMeekin, R. L. Z. Hoye, C. D. Bailie, T. Leijtens, I. M. Peters, M. C. Minichetti, N. Rolston, R. Prasanna, S. Sofia, D. Harwood, W. Ma, F. Moghadam, H. J. Snaith, T. Buonassisi, Z. C. Holman, S. F. Bent, M. D. McGehee, *Nature Energy.* **2017**, 2, 17009.

[3]   a) S. Shao, J. Liu, G. Portale, H.-H. Fang, G. R. Blake, G. H. ten Brink, L. J. A. Koster, M. A. Loi, *Advanced Energy Materials.* **2018**, 8; b) F. Gao, C. Li, L. Qin, L. Zhu, X. Huang, H. Liu, L. Liang, Y. Hou, Z. Lou, Y. Hu, F. Teng, *Rsc Adv.* **2018**, 8, 14025.

[4]   a) S. J. Lee, S. S. Shin, Y. C. Kim, D. Kim, T. K. Ahn, J. H. Noh, J. Seo, S. I. Seok, *Journal of the American Chemical Society.* **2016**, 138, 3974; b) F. Sani, S. Shafie, H. N. Lim, A. O. Musa, *Materials (Basel).* **2018**, 11.

[5]   a) M. Cheng, C. Chen, K. Aitola, F. Zhang, Y. Hua, G. Boschloo, L. Kloo, L. Sun, *Chem Mater.* **2016**, 28, 8631; b) J. Kim, G. Kim, H. Back, J. Kong, I. W. Hwang, T. K. Kim, S. Kwon, J. H. Lee, J. Lee, K. Yu, C. L. Lee, H. Kang, K. Lee, *Advanced Materials.* **2016**, 28, 3159.

[6]   a) K. Gao, Z. Zhu, B. Xu, S. B. Jo, Y. Kan, X. Peng, A. K. Jen, *Advanced Materials.* **2017**, 29; b) S. Dong, Y. Liu, Z. Hong, E. Yao, P. Sun, L. Meng, Y. Lin, J. Huang, G. Li, Y. Yang, *Nano Letters.* **2017**, 17, 5140.

[7]   C.-T. Lin, S. Pont, J. Kim, T. Du, S. Xu, X. Li, D. Bryant, M. A. McLachlan, J. R. Durrant, *Sustain Energ Fuels.* **2018**, 2, 1686.

[8]   a) S. Hong, J. Lee, H. Kang, G. Kim, S. Kee, J. H. Lee, S. Jung, B. Park, S. Kim, H. Back, K. Yu, K. Lee, *Science Advances.* **2018**, 4, eaat3604; b) J. Lee, J. Kim, C.-L. Lee, G. Kim, T. K. Kim, H. Back, S. Jung, K. Yu, S. Hong, S. Lee, S. Kim, S. Jeong, H. Kang, K. Lee, *Advanced Energy Materials.* **2017**, 7.

[9]   S. D. Dimitrov, Z. Huang, F. Deledalle, C. B. Nielsen, B. C. Schroeder, R. S. Ashraf, S. Shoaee, I. McCulloch, J. R. Durrant, *Energy & Environmental Science.* **2014**, 7.

[10]   J. Shi, D. Li, Y. Luo, H. Wu, Q. Meng, *Review of Scientific Instruments.* **2016**, 87, 123107.

[11]   a) R. Gottesman, P. Lopez-Varo, L. Gouda, J. A. Jimenez-Tejada, J. Hu, S. Tirosh, A. Zaban, J. Bisquert, *Chem.* **2016**, 1, 776; b) R. Gottesman, A. Zaban, *Accounts of Chemical Research.* **2016**, 49, 320.

[12]   a) M. De Bastiani, E. Aydin, T. Allen, D. Walter, A. Fell, J. Peng, N. Gasparini, J. Troughton, D. Baran, K. Weber, T. P. White, S. De Wolf, *Advanced Electronic Materials.* **2018**, DOI: 10.1002/aelm.2018005001800500; b) C. Battaglia, A. Cuevas, S. D. Wolf, *Energy & Enviromental Science.* **2016**, 9, 1552; c) R. A. Belisle, W. H. Nguyen, A. R. Bowring, P. Calado, X. Li, S. J. C. Irvine, M. D. McGehee, P. R. F. Barnes, B. C. O'Regan, *Energy & Environmental Science.* **2017**, 10, 192.

[13]   S. E. J. O'Kane, G. Richardson, A. Pockett, R. G. Niemann, J. M. Cave, N. Sakai, G. E. Eperon, H. J. Snaith, J. M. Foster, P. J. Cameron, A. B. Walker, *Journal of Materials Chemistry C.* **2017**, 5, 452.

Chapter 6. Summary and future study

The focus of this thesis is to understand the charge carrier dynamics in $MAPI_3$ perovskite solar cells using various transient optical tools. Chapter 3 describes the impact of perovskite evolution on several optical and crystallographic measurements in other to measure more accurate and reliable charge carrier dynamics. With this knowledge, the precise transient optical measurements are allowed to be made. Chapter 4 demonstrates the excitation density dependence of perovskite by using key optical measurements, PL, fs-TAS and tr-PL. Based on the measurements, we now understand why the number of PLQE measured using conventional PL could not refer the charge carrier transfer yield in perovskite system. In this study, I introduced new LED PL measurement and showed the correlation between the PLQE and the device performance. Now more complicated system which is perovskite/OPV integrated solar cell can be studied. In chapter 5, the charge carrier dynamics of the perovskite/OPV integrated system using fs-TAS is introduced, and the electronic field caused by BHJ blend layer can be modified to change the charge carrier dynamics.

In further studies, not only the perovskite film has to be carefully prepared, but also the ageing process need to be strictly controlled. This process changes the key information about the trap density of the perovskite film, which has an impact on device performance. The stability issues require to be studied along with degradation mechanisms. The enhancement of optical properties through self-healing processes has been well studied, but the location of the defect sites and the degradation process after the saturation of healing process has not been well defined. Additionally, in order to improve device performance using self-healing processes and stability, we need to know how to speed up the process and stop the process when it is fully healed.

Herein, the importance of the charge carrier density of the perovskite photovoltaic material is emphasized by various measurements. Other parts might need to be considered when studying perovskite device to test full device sample for the measurement. The 1 Sun LED PL measurement requires to improve sensor sensitivity and resolution, and use the AM 1.5 beam spectrum to test the effects of charge carrier accumulation caused by high carrier density and unbalanced charge transfer under the device working condition. In addition, a comparison of open circuit conditions and short circuit conditions is recommended to study, since the internal filed changes the dynamics.

The TAS measurement herein are limited by a narrow time window, several ps to 6 ns. Due to the long lifetime of perovskite, the dynamics is recommended to be checked using nanosecond scale TAS system. Some perovskite films have an extremely long bimolecular recombination lifetime in 1 sun which cannot be measured in this time window. With the bimolecular recombination lifetime, it was difficult to accurately determine the charge transfer yield. Likewise, for the integrated solar cell, much faster time scale needs to be checked, because the process of exciton generation and transfer between polymer BHJ system and perovskite layer is faster than the instrument response.